

## Ionization of atoms and molecules using 200-keV protons and 5.5-MeV/u bare C ions: Energy-dependent collision dynamics

Madhusree Roy Chowdhury,<sup>1,2</sup> A. Mandal,<sup>1</sup> A. Bhogale,<sup>1</sup> H. Bansal,<sup>1</sup> C. Bagdia,<sup>1</sup> S. Bhattacharjee,<sup>1</sup> J. M. Monti <sup>3</sup>,  
R. D. Rivarola,<sup>3</sup> and Lokesh C. Tribedi<sup>1,\*</sup>

<sup>1</sup>Tata Institute of Fundamental Research, Homi Bhabha Road, Colaba, Mumbai 400005, India

<sup>2</sup>M. S. University of Baroda, Vadodara 390001, India

<sup>3</sup>Instituto de Fisica Rosario, CONICET, Universidad Nacional de Rosario, 2000 Rosario, Argentina



(Received 17 March 2020; revised 16 June 2020; accepted 1 July 2020; published 28 July 2020;  
corrected 24 September 2020)

Using electron spectroscopy technique, we measure the absolute double-differential cross sections (DDCSs) of electrons emitted in collisions of 200-keV protons on He, CH<sub>4</sub>, and O<sub>2</sub> and 5.5-MeV/u bare C ions colliding on O<sub>2</sub>. The emitted electrons are measured in the energy range from 1 to 400 eV for He and CH<sub>4</sub> targets and up to 600 eV for O<sub>2</sub> to include the *K*-*LL* Auger line of oxygen. The electrons are detected over different emission angles varying from 20° in the extreme forward direction to 160° in the backward direction. The single-differential cross section (SDCS) and total cross section are deduced from the measured DDCSs spectra for all the targets. The DDCS and SDCS are compared with the state-of-the-art continuum distorted wave–eikonal initial state (CDW-EIS) theoretical model. The CDW-EIS model provides excellent agreement with the oxygen data at MeV energy, whereas the deviation in the case of keV energy is substantial, in spite of having nearly the same perturbation strength. The forward-backward angular asymmetry shows a saturation effect in the case of keV energy protons but no such signature is observed for the high-energy collision. A systematic analysis reveals that the asymmetry at low electron energy is sensitive to the associated atomic or molecular structure and is in close agreement with the theory.

DOI: [10.1103/PhysRevA.102.012819](https://doi.org/10.1103/PhysRevA.102.012819)

### I. INTRODUCTION

The ionization of atomic and molecular targets by the impact of charged particles has been a subject of study over the decades and still draws attention in different fields such as astrophysics, plasma physics (particularly for the modeling of the low-temperature plasmas), and radiation therapy for cancer treatment [1–3]. In this work we focus on the study of single ionization of three different atomic and molecular targets, such as He, CH<sub>4</sub>, and O<sub>2</sub> in collisions with keV energy protons. To understand how the ionization dynamics changes with the variation in the velocity  $v_p$  and charge state  $q_p$  of the projectile, we provide a comparative study for the ionization of the O<sub>2</sub> molecule using keV energy protons and MeV energy C<sup>6+</sup> ions. These two projectiles were chosen such that, although the  $q_p$  and  $v_p$  are quite different, their perturbation strengths  $q_p/v_p$  are nearly the same, i.e., 0.35 for the 200-keV/u protons and 0.40 for the 5.5-MeV/u C<sup>6+</sup> ions.

The collision of protons on He is one of the simplest and a benchmark system for testing the efficacy of the theoretical models on ion-atom collisions. Helium is also one of the most abundant elements found in the universe. The protons and  $\alpha$  particles are present abundantly in the solar wind, which is a highly ionized magnetized plasma. The CH<sub>4</sub> is one of the important molecules which is present in the interstellar medium, in the circumstellar environment, on the surface of

Titan, and also on the surfaces of several icy bodies of the solar system [4,5]. The methane-containing surfaces are exposed to the energetic protons and other ions from the cosmic rays leading to the ionization and fragmentation of the molecules. A better understanding of the ionization cross sections of these molecules is thus essential for modeling the various planetary atmospheres and for other astrophysical applications.

Although the molecular targets, such as CH<sub>4</sub> and O<sub>2</sub>, are more complicated compared to He, they act as benchmark or reference targets for studying the ionization of large biomolecules [6], which have gained immense importance for hadron therapy (for a recent review see [1,2]). The methane also serves as a reference system for studying the large hydrocarbon molecules such as the polycyclic aromatic hydrocarbon molecules in connection with an application in astrochemistry. Therefore, these small molecular targets serve as a bridge between the small atoms and large molecules and provide a stringent test of the theoretical models before they are applied for the larger molecules. Apart from these applications, ionization studies of diatomic molecules such as O<sub>2</sub>, H<sub>2</sub>, and N<sub>2</sub> have also gained renewed interest due to the observation of the Young-type interference effect in the electron-emission spectrum due to spatial coherence, a fundamental quantum-mechanical interest [7–12]. The study of such atoms and molecules is also crucial towards the development of a comprehensive scaling law for ionization (see, for example, the work by Montenegro *et al.* [13]).

Over the past few decades, several studies have been carried out on the double-differential cross sections (DDCSs)

\*lokesh@tifr.res.in; ltribedi@gmail.com

of electrons emitted from a helium atom using the protons and highly charged ions having energies from a few keV to several MeV [14–30]. Different studies on the ionization, fragmentation, and charge-transfer processes [31–34] have also been carried out for CH<sub>4</sub> and O<sub>2</sub> targets. However, not many measurements of the DDCS of electron emission from CH<sub>4</sub> and O<sub>2</sub> exist in the literature [35–41]. Studies on the total ionization cross sections are the most common, although the DDCS measurements provide a much better understanding of the collision dynamics.

In the present experiment, besides the high-energy collision ( $v_p \sim 15$  a.u.), we also measure the electron emission at a lower velocity ( $v_p \sim 2.8$  a.u.), which is closer to the intermediate-velocity regime where along with ionization, electron capture and transfer ionization channels are also effective. In most of the earlier work on DDCS measurements of electron emission from He by protons [15–17], the measured data were compared with the first Born approximation, a one-center model, which is well known to work only for projectiles with high energy and does not deal with postcollisional effects. In contrast, the continuum distorted wave–eikonal initial state (CDW-EIS) model is well known to be effective in the intermediate- to high-energy regime of the projectile. This model assumes the ionized electron to be influenced by the long-range Coulomb field of both the target and the projectile, thus explaining the two-center effect accurately. The present series of experiments using both the He atom and simple molecules along with an elaborate comparison with the CDW-EIS model provides valuable inputs towards the understanding of the collision dynamics in the low- and high-velocity regimes.

We report the energy and angular distributions of the DDCS of the electrons emitted from He, CH<sub>4</sub>, and O<sub>2</sub> in collisions with 200-keV/u protons along with the same for O<sub>2</sub> with 5.5-MeV/u bare C ions. The forward-backward angular asymmetry  $\alpha(k)$ , which reflects well on the two-center effect and also the characteristics of the target, is deduced for all three targets. In our experiments with 200-keV H<sup>+</sup> ions, since the projectile velocity is almost comparable to the velocity of the valence electrons in the target,  $\alpha(k)$  is an even more important quantity to study.

## II. EXPERIMENTAL TECHNIQUES

A brief description of the experimental apparatus is given here. The 200-keV protons (velocity  $v_p = 2.83$  a.u.) were obtained from the electron cyclotron resonance–based ion accelerator facility at TIFR, Mumbai [42,43]. This is a 14.5-GHz machine with a maximum extraction voltage of 30 kV. The electron cyclotron resonance (ECR) plasma ion source along with an electrostatic lens, Faraday cup, and analyzing magnet is mounted on a high-voltage deck which can be raised up to 400 kV. This low-energy accelerator is suitable for providing low-velocity highly charged ions. There are four beamlines and a switching magnet is used to steer the beam in the desired beamline. Each beamline is equipped with electrostatic quadrupole triplet lenses and X-Y deflectors for focusing and steering the ion beam. A pair of four jawed slits is also used to cut the beam and control the beam divergence. A differential pumping arrangement is connected at the end

of the beamline, which is followed by the scattering chamber. An extended aperture, 2 mm in diameter and 30 mm long, is placed at the end of the beamline and another aperture of 4 mm diameter is placed just at the entrance of the scattering chamber for further beam collimation. The beamline pressure is maintained at about  $5 \times 10^{-9}$  mbar and the scattering chamber is maintained at a base pressure of  $10^{-8}$  mbar. It is necessary to maintain a high vacuum in the beamline to reduce the probability of charge neutralization of the projectile ions. In the case of He and CH<sub>4</sub>, the scattering chamber is flooded with the target gases at an absolute pressure of 0.1 and 0.05 mTorr, respectively, which is measured using a capacitance manometer (MKS Baratron). In the case of O<sub>2</sub>, the experiments are performed both under flooded chamber conditions and by using an effusive jet source; in both cases similar results are obtained. In the case of the effusive jet source, the experiment is performed in a crossed-beam arrangement. Two sets of  $\mu$  metal sheets are attached to the inner walls of the scattering chamber to reduce the Earth’s magnetic field to about 10 mG near the interaction region. The ejected electrons are energy analyzed using the hemispherical electrostatic energy analyzer and are further detected by the channel electron multiplier (CEM). A preacceleration voltage  $V_c$  of 6 V is applied at the entrance and exit slits of the spectrometer to increase the collection efficiency of the low-energy electrons. The resolution of the analyzer is 6% of the electron energy. The front of the CEM is biased to +100 V, which ensures a uniform collection efficiency of the detector in the electron energy range measured. The number of projectile ions is obtained by measuring the ion beam current on the Faraday cup. The DDCSs are measured in both the presence and absence of the target gas for all the angles, although the background counts in the absence of the target gas are very low. The ejected electrons from He and CH<sub>4</sub> are measured between 1 and 400 eV and for O<sub>2</sub> from 1 to 600 eV. The measurements for all three targets impacted by 200-keV protons are performed for 11 different angles from 20° to 160°. The total absolute error in the present series of experiments varies from 15% to 19%, which includes contributions from gas pressure fluctuations, counting statistics, efficiency of the detector, resolution of the spectrometer, and the solid-angle path-length integral. The statistical error varies from  $\sim 1\%$  in the case of the forward angles to  $\sim 8\%$  for the higher energies in the extreme backward angles, where the cross section falls by order of magnitude. However, below 10 eV some more systematic error cannot be ruled out, which is difficult to estimate.

A similar kind of setup is used to perform the measurements for the O<sub>2</sub> target using a MeV energy ion beam. The 66-MeV C<sup>5+</sup> ions ( $v_p = 14.9$  a.u.) were obtained from the 14-MV BARC-TIFR Pelletron Accelerator Facility at TIFR, Mumbai. The energy and charge state analyzed C<sup>5+</sup> ions are passed through a poststripper carbon foil arrangement to obtain the bare ions. The C<sup>6+</sup> ions are selected using a switching magnet and directed to the desired beamline. The rest of the experimental techniques and the arrangement comprising the scattering chamber, differential pumping station, and electron analyzer are similar to those in the case of measurements with 200-keV H<sup>+</sup> ions. The experiment is performed under flooded chamber conditions at a static absolute pressure of

0.15 mTorr and the DDCS spectra for electrons emitted from O<sub>2</sub> are measured for 12 different angles, namely, 20°, 30°, 45°, 60°, 75°, 80°, 90°, 105°, 120°, 135°, 150°, and 160°.

### III. THEORETICAL DESCRIPTION

An independent-particle approximation is employed to describe the single-ionization reaction. This means that only one electron from each one of the atomic or molecular orbitals is considered to be ionized, whereas all the other target electrons (the passive electrons) are considered to remain frozen in their initial orbitals. The ionization process is described within the prior form of the CDW-EIS formalism within the straight-line version of the impact parameter approximation used for the calculations [44,45]. The scattering amplitude as a function of the impact parameter in the prior version within the CDW-EIS approximation can be written as [46]

$$A_{if}^-(\rho) = -i \int_{-\infty}^{+\infty} dt \left\langle \chi_f^- \left| \left[ \left( H_{el} - i \frac{\partial}{\partial t} \right) \chi_i^+ \right] \right. \right\rangle, \quad (1)$$

where  $H_{el}$  is the one-active-electron Hamiltonian and  $\chi_f^-$  and  $\chi_i^+$  are the final and initial channel distorted wave functions, respectively, given by

$$\chi_i^+ = \varphi_i(\mathbf{x}) \exp(-i\varepsilon_i t) \exp[-i\nu \ln(v s + \mathbf{v} \cdot \mathbf{s})], \quad (2)$$

$$\begin{aligned} \chi_f^- = & \varphi_f(\mathbf{x}) \exp(-i\varepsilon_f t) N^*(\lambda) {}_1F_1[-i\lambda; 1; -i(kx - \mathbf{k} \cdot \mathbf{x})] \\ & \times N^*(\xi) {}_1F_1[-i\xi; 1; -i(ps - \mathbf{p} \cdot \mathbf{s})], \end{aligned} \quad (3)$$

with  $\mathbf{x}$  ( $\mathbf{s}$ ) the active-electron coordinate in a target-fixed (projectile-fixed) reference frame. In (2)  $\varphi_i$  represents the active-electron initial bound state with  $\varepsilon_i$  its initial binding energy and  $\nu = Z_p/v$  with  $Z_p$  the projectile charge and  $v$  the collision velocity. In (3)  $\varphi_f$  is a free-electron plane wave with momentum  $\mathbf{k}$ ,  $\varepsilon_f = \frac{1}{2}k^2$ ,  $\xi = Z_p/p$ ,  $\mathbf{p} = \mathbf{k} - \mathbf{v}$ , and  $\lambda = \tilde{Z}_T/k$  with  $\tilde{Z}_T$  and the effective target nuclear charge describing the interaction of the active electron with an effective residual-target Coulomb potential. Also  ${}_1F_1$  is the hypergeometric function and  $N(a) = \exp(\pi a/2)\Gamma(1 - ia)$  its normalization factor (with  $\Gamma$  the Euler Gamma function). The initial bound state of the He target was considered within a Roothaan-Hartree-Fock (RHF) representation [47]. In the case of the O<sub>2</sub> target, the molecule was approximated simply by two independent oxygen atoms also described by RHF functions [47]. The CH<sub>4</sub> molecule was represented by a linear combination of atomic orbitals (LCAO) within a complete neglect of differential overlap (CNDO) approximation (see [37,48]).

In all cases the residual-target continuum state effective charge is taken as  $\tilde{Z}_T = n_i \sqrt{-2\varepsilon_i}$ . In the He and O cases,  $n_i$  is the principal quantum number of the atomic orbital and  $\varepsilon_i$  its ionization energy. In the CH<sub>4</sub> case,  $\varepsilon_i$  is now the molecular orbital ionization energy and  $n_i$  the principal quantum number of the corresponding atomic orbital in the LCAO.

This model was applied with very good success, first for mono-electronic atomic targets [49], and since then it has been continuously upgraded (see, for example, the review by Fainstein *et al.* [22]). The model was then extended to multi-electronic atomic targets [44] by including numerical wave functions. The CDW-EIS model has been further improved in order to apply it to small [46,50] and larger biological [51]

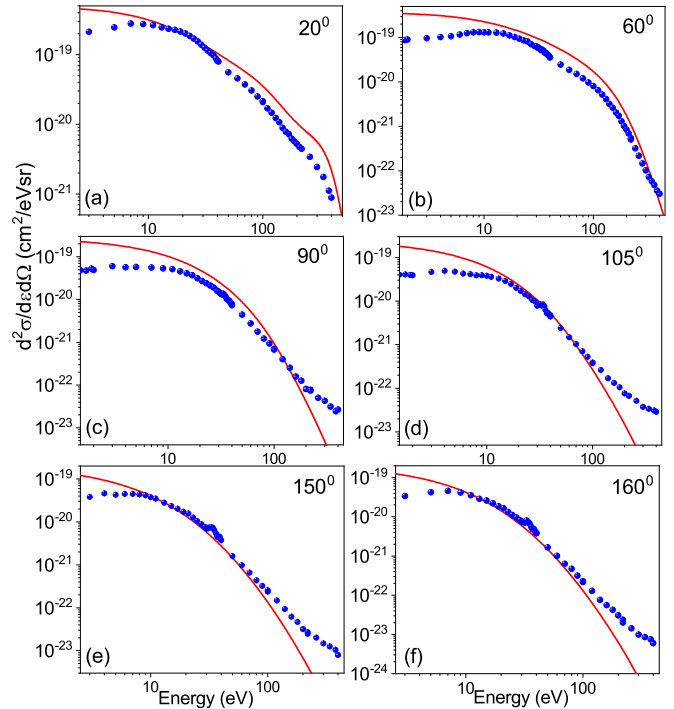


FIG. 1. Absolute electron DDCS for He as a function of emission energies for different forward and backward angles. The solid line in each panel shows the CDW-EIS model calculation.

molecules. Such a developed model has been successfully applied to compare experimental data for methane [38], adenine [3,6], and other large molecules.

## IV. RESULTS AND DISCUSSION

### A. Energy distribution of the electron DDCS

#### 1. 200-keV proton impact

The absolute DDCSs of the electrons emitted from He for six different electron-emission angles are displayed in Fig. 1. The small peak seen in the backward angles at around 35 eV corresponds to the autoionization process following a double excitation. In the case of forward angles, due to the large Coulomb ionization contribution, the autoionization peak is not observed. The CDW-EIS model provides qualitatively overall good agreement with the data for all the forward angles. In the case of the backward angles, the model matches well with data points up to about 70 eV, beyond which it underestimates the data for the rest of the spectra. For the lowest electron energies (i.e., between 1 and 10 eV), the experimental uncertainties are large, as there could be insufficient collection of electrons due to any stray fields causing additional systematic errors. This may explain only a part of the deviation between the theory and experiment at these low energies.

Figure 2 displays the energy distribution curves for CH<sub>4</sub> at different forward and backward emission angles. The DDCS falls by several orders of magnitude with an increase in ejected-electron energy for a fixed emission angle. The sharp peak observed in the backward angles at about 240 eV corresponds to the *K*-*LL* Auger electron emission from carbon

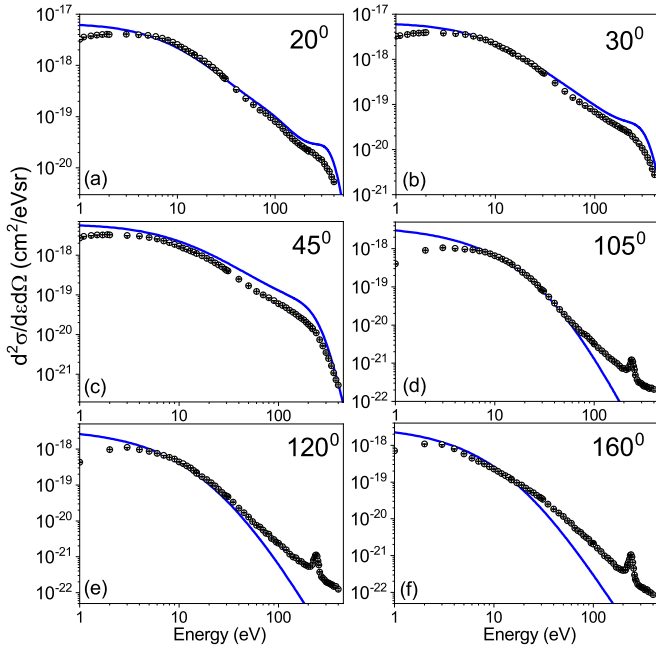


FIG. 2. Same as Fig. 1 but for 200-keV  $H^+$  ions impacting on  $CH_4$ .

which occurs when a vacancy exists in the inner shell. Overall very good agreement is observed between the theoretical model and experimental data for the forward angles, whereas in the backward angles one observes good agreement up to about 50 eV, beyond which the theory shows a discrepancy with the measured data. A small humplike structure can be seen in the forward angles around 250–300 eV at  $30^\circ$  both experimentally and theoretically. This hump is due to the binary nature of the collision or head-on collision between the projectile and the target electron. The position of the binary encounter (BE) peak is given by  $E = 4 \cos^2 \theta m_e (\frac{E_p}{M_p})$ , where  $M_p$  is the mass of the projectile having energy  $E_p$  and  $m_e$  is the mass of the electron emitted with energy  $E$  at an emission angle  $\theta$ . For the present experiment of 200-keV  $H^+$  ions, at  $30^\circ$ , the peak should be observed at 300 eV, whereas for an emission angle of  $45^\circ$ , it should be observed at 200 eV. If the target electron is initially at rest, then one would expect a prominent peak; however, an electron bound to an atom or molecule has an initial momentum distribution which superimposes on the peak. In the present case, the projectile velocity is 2.83 a.u., which is almost comparable to the orbital velocity of the electrons (1 a.u.) in the outermost shell of  $CH_4$  and hence the initial velocity distribution of the target electrons completely smears out the binary peak over the entire range of emission energies.

Similarly, Fig. 3 shows the electron-emission DDCS spectra for  $O_2$  when bombarded with 200-keV  $H^+$  ions; the solid curves correspond to twice the theoretical calculations for atomic oxygen. For the present collision system, a large discrepancy is observed between the measured data and the calculations for all the emission angles, although any obvious reason for the same is not known. The  $K$ - $LL$  Auger electron-emission peak is seen at around 480 eV for all the backward

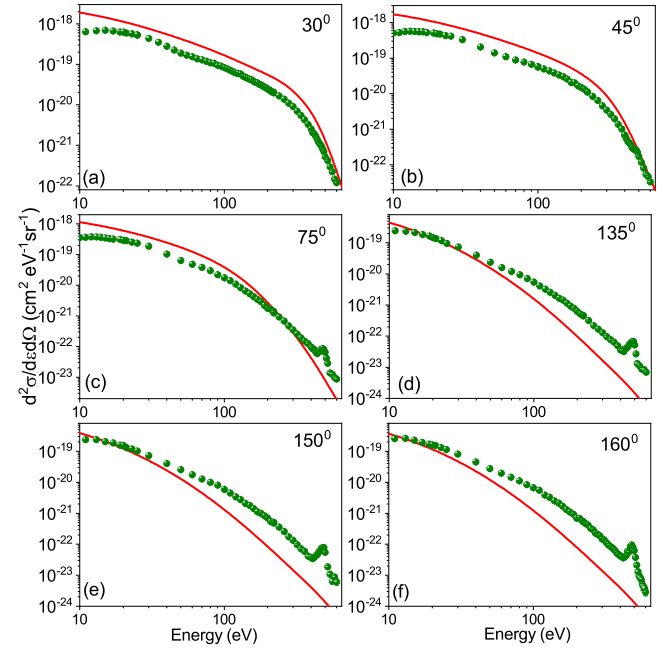


FIG. 3. Absolute electron DDCS for six different emission angles for collision of 200-keV protons on  $O_2$ . Solid lines represent the CDW-EIS calculations for atomic oxygen multiplied by 2.

angles, whereas for forward angles it becomes invisible due to the large continuum cross sections.

## 2. 66-MeV bare C ion impact

The energy distribution of the electrons ejected due to collision of  $C^{6+}$  ions with  $O_2$  is shown in Fig. 4. The low-energy part of the spectrum is dominated by the soft col-

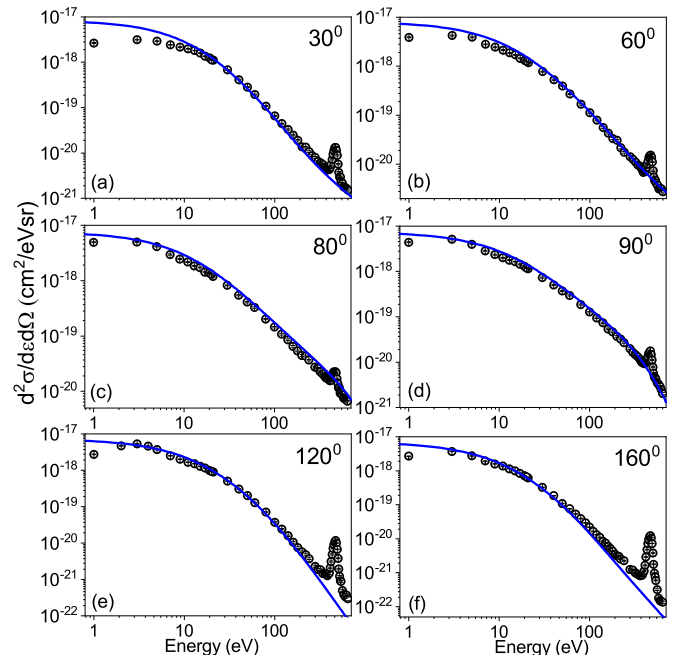


FIG. 4. Same as Fig. 3 but for the collision system of 66-MeV  $C^{6+}$  ions impacting on  $O_2$ .

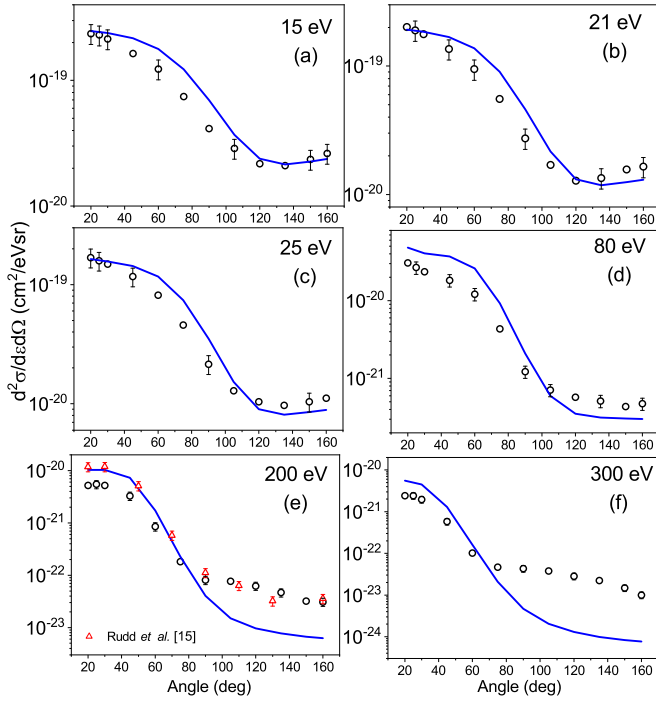


FIG. 5. DDCS of ejected electrons from He as a function of emission angle for different emission energies (black open circles). The solid curves show the CDW-EIS model calculations.

lision or glancing collision mechanism where the electrons are emitted with a large impact parameter. In the case of highly charged ions like  $C^{6+}$ , the two-center effect plays an important role which generates the intermediate part of the spectrum. Moving further ahead in the spectrum, one can see the  $K$ - $LL$  Auger peak at  $\sim 480$  eV for oxygen. For the present projectile, since  $v_p$  is much larger compared to the orbital velocity of the target electrons, the BE peak will be present at a much higher emission energy in the case of the extreme forward angles. The CDW-EIS model for twice the atomic oxygen provides excellent agreement with the experimental data points for all the angles and over the entire energy range under investigation. Only in the case of extreme backward angles, at the higher-energy side of the spectrum, the theory underestimates the data.

### B. Angular distribution of the electron DDCS

Figure 5 shows the angular distribution in the case of the He target for different electron-emission energies. A large angular asymmetry is observed between the extreme forward and extreme backward angles even in the case of low emission energies such as 15 eV. The asymmetry increases even further with an increase in emission energy. This large angular asymmetry between the forward and backward angles may be explained by the two-center collision mechanism, as mentioned in the preceding section. In the case of the atomic target He, excellent agreement is observed between the measured data and the theoretical model for low-emission energies such as 15, 21, and 25 eV. With an increase in emission energy, although qualitative agreement is observed between the theoretical curves and measured quantities, quantitatively it is seen

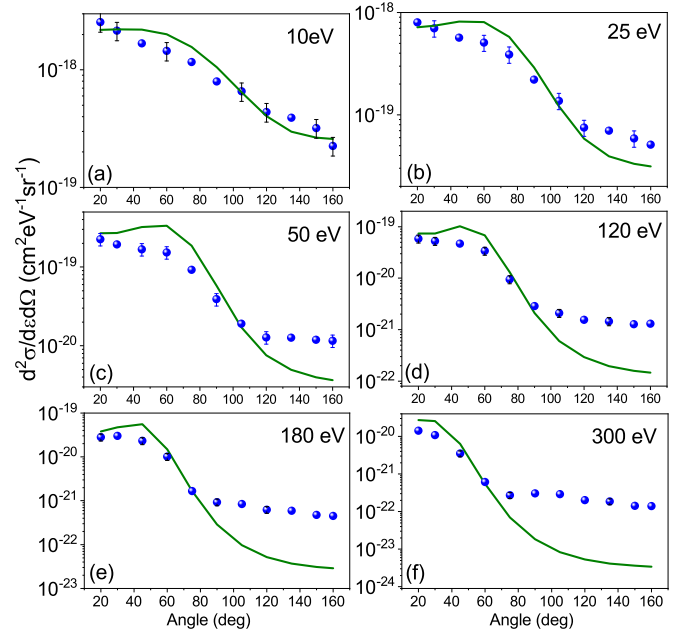


FIG. 6. Angular distribution of the electron DDCS for  $CH_4$  at fixed electron-emission energies along with the theoretical calculations.

that theory slightly overestimates the data for forward angles and underestimates the data points for the backward angles. For higher emission energies, the departure of the theory from the experimental measurements increases even further for the backward angles. The experimental electron DDCS for He reported by Rudd *et al.* [15] is shown in Fig. 5(e) by red triangles. These points match well with the present data for the backward angles but are a factor of 2 times higher for the extreme forward angles. In Figs. 6 and 7, similar results are observed between theoretical curves and experimental data for

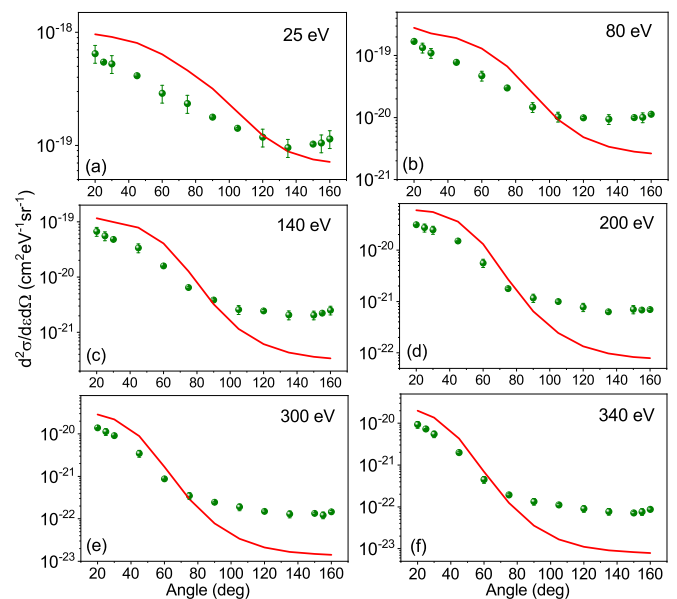


FIG. 7. Angular distribution of  $e^-$  DDCS from  $O_2$  in collisions with 200-keV protons along with CDW-EIS calculations.

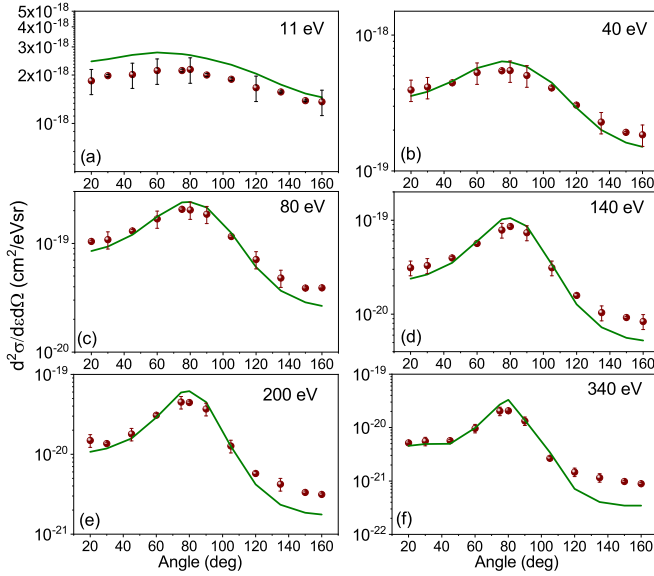


FIG. 8. Same as Fig. 7 but for 66-MeV  $C^{6+}$  ions colliding with  $O_2$ .

both targets,  $CH_4$  and  $O_2$  in collisions with 200-keV  $H^+$  ions. In all the cases, the CDW-EIS model agrees qualitatively with data, but quantitatively shows maximum discrepancies in the backward angles for higher emission energies. In Figs. 5–7, the total absolute error bars are shown for some of the points. From the angular distribution plots, the CDW-EIS model is seen to work well particularly for forward angles.

In Fig. 8 we present the DDCS of electrons as a function of emission angle for the 66-MeV  $C^{6+}$  ion impact on the  $O_2$  target gas. The angular distribution plots shown in the six panels for different electron energies reveal a completely different trend from that observed in Fig. 7. In the case of 11 eV [Fig. 8(a)], we observe an almost flat distribution over the entire angular spread. This is due to the dominance of the soft-collision mechanism, indicating isotropic ionization over all angles. For higher electron energies, a peak is seen around  $80^\circ$  which gets sharper with an increase in electron emission-energy. This peak is due to the binary-collision mechanism. Except for the lowest energies, the forward angles have higher cross sections compared to the backward angles, which is due to the two-center effect. For 80 eV, the DDCS for extreme forward angles is 2.7 times higher than for the extreme backward angles. This factor increases further with higher emission energies and in the case of 340 eV it is about 6 times higher than for backward angles, indicating a drastic fall of cross sections in the case of backward angles. The CDW-EIS model shows overall good agreement with the measured data, except for the higher energies for backward angles, where it underestimates the data.

### C. Forward-backward angular asymmetry

Following the prescription of Fainstein *et al.* [52], we define the forward-backward angular asymmetry parameter  $\alpha(k)$  as

$$\alpha(k, \theta) = \frac{\sigma(k, \theta) - \sigma(k, \pi - \theta)}{\sigma(k, \theta) + \sigma(k, \pi - \theta)}, \quad (4)$$

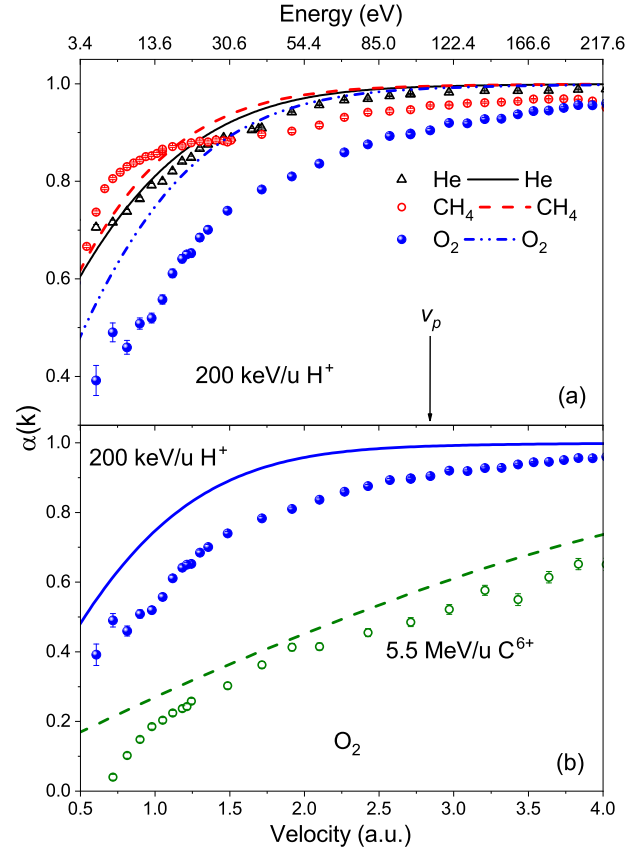


FIG. 9. Asymmetry parameter  $\alpha(k)$  for (a) three different targets bombarded by the same projectile and (b)  $O_2$  impacted by 200-keV protons and 66-MeV  $C^{6+}$  ions. All lines indicate CDW-EIS model predictions.

where the electron energy  $\epsilon_k = \frac{k^2}{2}$  in a.u.,  $\theta$  is a low forward angle, and  $k$  denotes the ejected-electron velocity. Since the angular distribution varies slowly near  $0$  and  $\pi$ , we use the measured DDCS at  $20^\circ$  to calculate the approximate value of the asymmetry parameter, i.e.,  $\alpha(k)$  for all four collision systems under investigation (shown in Fig. 9). For He and  $CH_4$ , a large asymmetry is observed which increases monotonically from 0.7 to  $\sim 1.0$ , showing a tendency to saturate beyond  $k = 2.75$  a.u., as shown in Fig. 9(a). Theory predicts similar behavior, showing overall good agreement for He. However, experimentally  $CH_4$  shows a slightly different shape compared to that for He as well as that predicted by the CDW-EIS calculation. For 200-keV protons colliding on  $O_2$ , the  $\alpha(k)$  increases monotonically from 0.4 to  $\sim 1.0$  and saturates beyond 2.75 a.u. One may note that although the shapes of the angular distributions at the lower-energy (keV) and higher-energy (MeV) collisions are vastly different, the asymmetry parameter reveals similar kind of distributions as a function of  $k$ . This gives us a way to compare the data in a widely different projectile energy range. It is obvious from Fig. 9(b) that the  $\alpha(k)$  values for 200-keV/u protons are much larger than that for the collisions with high energy, i.e., 5.5-MeV/u  $C^{6+}$  ions. This may be explained by the fact that the two-center effect and postcollisional interactions are much stronger for 200-keV protons than for the higher-energy

TABLE I. Total ionization cross section in units of Mb for the four collision systems.

Target	Projectile	$q_p/v_p$	TCS		Ratio
			Expt. ( $\pm 18\%$ )	CDW-EIS	
He	200-keV/u $H^+$ ions	0.35	31.5	50.7	1.6
$CH_4$	200-keV/u $H^+$ ions	0.35	252	346	1.4
$O_2$	200-keV/u $H^+$ ions	0.35	148	337	2.3
$O_2$	5.5-MeV/u $C^{6+}$ ions	0.40	708	809	1.14

projectiles, although the perturbation strengths, i.e.,  $q_p/v_p$ , for both projectiles are almost same. Thus, the asymmetry parameter cannot be characterized uniquely by the perturbation strength; rather it depends independently on the actual value of the  $q_p$  and the  $v_p$ . It can be seen from Fig. 9(a) that for lower electron energies  $\alpha(k)$  is sensitive to the atomic or molecular structure of the target and has the lowest value for the  $O_2$ , followed by the He and  $CH_4$  targets. For these low-energy electrons, the impact parameters are expected to be large and the projectile interacts with the whole atom or molecule. In such cases the momentum transfer is small and thereby the ejected electrons are sensitive to the structure of the atom or the molecule. With an increase in the electron velocity, the  $\alpha(k)$  tend to merge together, since for these electron velocities the impact parameter is quite small and hence the projectile interacts mostly with individual atoms in the molecule. Another feature that is observed for all three targets is the saturation effect. This effect is seen to occur when the electron velocity is close to or above the velocity of the projectile. In the case of 66-MeV bare C ions, with the projectile velocity being much higher than the highest value of  $k$  measured, the  $\alpha(k)$  values keep on increasing with the increase in the electron velocity. Therefore, the angular asymmetry is another or complementary way to look into the information about collision dynamics and its dependence on molecular species.

#### D. Single-differential cross section

The measured DDCS spectra can be used to obtain the single-differential cross section (SDCS) by integrating the DDCS over one of the variables, either the measured emission energies or the emission angles. Figure 10(a) shows the SDCS as a function of emission angles for all three targets He,  $CH_4$ , and  $O_2$  along with the CDW-EIS calculations. The SDCSs obtained experimentally and theoretically for methane have been multiplied by a factor of 4 (shown in the figure). For all three targets, the SDCSs have been obtained by integrating the data from 5 to 400 eV. The CDW-EIS prediction matches well with the experimentally obtained SDCS for the He atom, although it slightly overestimates the data. In the case of  $CH_4$ , the theory shows qualitative agreement with excellent matching around  $100^\circ$ – $120^\circ$ . Contrary to the above two targets, for  $O_2$ , a wide deviation is observed between experimental and theoretical SDCSs over almost the entire angular region. Figure 10(b) displays the SDCS for the MeV energy bare C ions impacting on  $O_2$ . Here also the integration has been performed between 5 and 400 eV. The distribution is

reproduced very well by the theoretical model, with excellent agreement for the backward angles.

Integrating the SDCS further over the emission angles, we get the total ionization cross section (TCS) of the collision system both experimentally and theoretically. The TCS values provided in Table I have been deduced by integrating over the electron energies from 5 to 400 eV and over the emission angles between  $20^\circ$  and  $160^\circ$ . The theoretical to experimental TCS ratios provide the best agreement for MeV energy highly charged ion projectile, whereas deviations (by a factor of 1.4–2.3) exist for 200-keV protons, with the maximum difference occurring in the case of  $O_2$ . From this study it may be inferred that although  $q_p/v_p$  was nearly the same for both energies, the difference between the data and the model is not the same; rather a larger deviation is seen at the lower energy. The experimentally measured DDCS data are provided in the Supplemental Material [53].

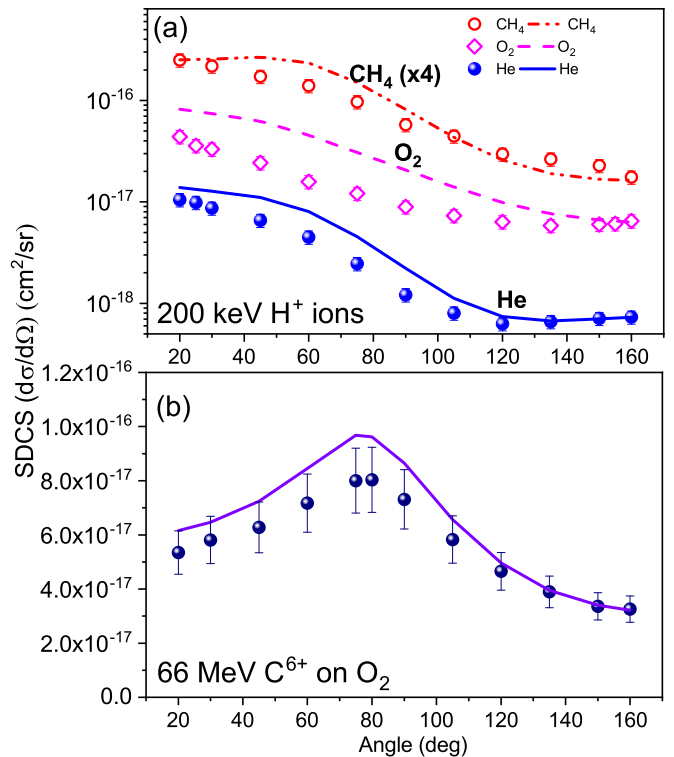


FIG. 10. SDCS as a function of emission angles for (a) all three targets in collisions with 200-keV protons along with CDW-EIS calculations (solid and dashed lines) [the data for  $CH_4$  (and theory) are multiplied by 4] and (b) 66-MeV  $C^{6+}$  ions impacting on  $O_2$ .

## V. CONCLUSION

We have measured the absolute DDCS of the electrons emitted from an atomic target He and two molecular targets CH<sub>4</sub> and O<sub>2</sub> when ionized by 200-keV/u protons. Double-differential cross-section measurements have also been carried out for O<sub>2</sub> in collisions with 5.5-MeV/u bare C ions. These two projectiles were chosen such that the perturbation strengths for both projectiles were nearly the same. In the case of 5.5-MeV/u bare C ions, the CDW-EIS calculations for oxygen show excellent agreement with the measured data for all the angles. For 200-keV protons, the model provides reasonably good agreement for He and CH<sub>4</sub>, but overestimates the DDCS for O<sub>2</sub> in the case of all angles. The angular distribution shows a distinctly different character for the two different projectiles. In the case of lower-energy collisions the forward-backward asymmetry parameter has a much higher value compared to that for high-energy C ions, in spite of almost the same perturbation strength. This implies that the perturbation strength  $q_p/v_p$  alone cannot characterize completely the asymmetry and two-center effect. For 200-keV protons,  $\alpha(k)$  showed a saturation effect (irrespective

of the target species) for electron velocity greater than the velocity of the projectile. The single-differential distributions were also derived. The CDW-EIS model provides the best agreement for the MeV energy collisions, whereas deviations (by a factor of 1.4–2.3) exist for the 200-keV protons with the maximum difference occurring in the case of O<sub>2</sub>, in spite of having the same perturbation strength for all the collisions. Further systematic investigations are required to check the efficacy of perturbation strength in characterizing the collision dynamics.

## ACKNOWLEDGMENTS

We would like to thank N. Mhatre, K. V. Thulasiram, W. A. Fernandes, and D. Pathare for their help during the operation of the ECR ion accelerator. We are also grateful to the staff at the BARC-TIFR Pelletron Accelerator Facility. One of the authors (M.R.C) would like to acknowledge financial assistance from Council of Scientific and Industrial Research (CSIR), India.

- 
- [1] L. C. Tribedi, in *State-of-the-Art Reviews on Energetic Ion-Atom and Ion-Molecule Collisions*, edited by D. Belkić, I. Bray, and A. Kadyrov (World Scientific, Singapore, 2019), Vol. 2, Chap. 3, pp. 59–98.
  - [2] F. Aumayr, K. Ueda, E. Sokell, S. Schippers, H. Sadeghpour, F. Merkt, T. F. Gallagher, F. B. Dunning, P. Scheier, O. Echt *et al.*, *J. Phys. B* **52**, 171003 (2019).
  - [3] Y. Iriki, Y. Kikuchi, M. Imai, and A. Itoh, *Phys. Rev. A* **84**, 052719 (2011).
  - [4] R. V. Yelle, J. Cui, and I. C. F. Müller-Wodarg, *J. Geophys. Res.: Planet.* **113**, E10003 (2008).
  - [5] A. G. G. M. Tielens, The molecular universe, *Rev. Mod. Phys.* **85**, 1021 (2013).
  - [6] S. Bhattacharjee, C. Bagdia, M. R. Chowdhury, A. Mandal, J. M. Monti, R. D. Rivarola, and L. C. Tribedi, *Phys. Rev. A* **100**, 012703 (2019).
  - [7] S. Nandi, A. N. Agnihotri, S. Kasthurirangan, A. Kumar, C. A. Tachino, R. D. Rivarola, F. Martín, and L. C. Tribedi, *Phys. Rev. A* **85**, 062705 (2012).
  - [8] M. Winkworth, P. Fainstein, M. Galassi, J. Baran, B. Dassanayake, S. Das, A. Kayani, and J. Tanis, *Nucl. Instrum. Methods Phys. Res. Sect. B* **267**, 373 (2009).
  - [9] M. Roy Chowdhury and L. C. Tribedi, *J. Phys. B* **50**, 155201 (2017).
  - [10] M. Ilchen, L. Glaser, F. Scholz, P. Walter, S. Deinert, A. Rothkirch, J. Seltmann, J. Viefhaus, P. Declava, B. Langer, A. Knie, A. Ehresmann, O. M. Al-Dossary, M. Braune, G. Hartmann, A. Meissner, L. C. Tribedi, M. AlKhaldi, and U. Becker, *Phys. Rev. Lett.* **112**, 023001 (2014).
  - [11] D. Misra, U. Kadhane, Y. P. Singh, L. C. Tribedi, P. D. Fainstein, and P. Richard, *Phys. Rev. Lett.* **92**, 153201 (2004).
  - [12] D. Misra, A. Kelkar, U. Kadhane, A. Kumar, L. C. Tribedi, and P. D. Fainstein, *Phys. Rev. A* **74**, 060701(R) (2006).
  - [13] E. C. Montenegro, G. M. Sigaud, and R. D. DuBois, *Phys. Rev. A* **87**, 012706 (2013).
  - [14] M. E. Rudd and T. Jorgensen, *Phys. Rev.* **131**, 666 (1963).
  - [15] M. E. Rudd, C. A. Sautter, and C. L. Bailey, *Phys. Rev.* **151**, 20 (1966).
  - [16] M. E. Rudd and D. H. Madison, *Phys. Rev. A* **14**, 128 (1976).
  - [17] D. H. Madison, *Phys. Rev. A* **8**, 2449 (1973).
  - [18] M. E. Rudd, R. D. DuBois, L. H. Toburen, C. A. Ratcliffe, and T. V. Goffe, *Phys. Rev. A* **28**, 3244 (1983).
  - [19] A. Salin, *J. Phys. B* **5**, 979 (1972).
  - [20] A. Salin, *J. Phys. B* **22**, 3901 (1989).
  - [21] D. K. Gibson and I. D. Reid, *J. Phys. B* **19**, 3265 (1986).
  - [22] P. D. Fainstein, V. H. Ponce, and R. D. Rivarola, *J. Phys. B* **24**, 3091 (1991).
  - [23] J. Berakdar, J. Briggs, and H. Klar, *Z. Phys. D* **24**, 351364 (1992).
  - [24] S. T. Manson, L. H. Toburen, D. H. Madison, and N. Stolterfoht, *Phys. Rev. A* **12**, 60 (1975).
  - [25] N. Stolterfoht, H. Platten, G. Schiwietz, D. Schneider, L. Gulyás, P. D. Fainstein, and A. Salin, *Phys. Rev. A* **52**, 3796 (1995).
  - [26] J. H. Miller, L. H. Toburen, and S. T. Manson, *Phys. Rev. A* **27**, 1337 (1983).
  - [27] J. O. P. Pedersen, P. Hvelplund, A. G. Petersen, and P. D. Fainstein, *J. Phys. B* **24**, 4001 (1991).
  - [28] R. D. DuBois, L. H. Toburen, and M. E. Rudd, *Phys. Rev. A* **29**, 70 (1984).
  - [29] J. M. Monti, O. A. Fojón, J. Hanssen, and R. D. Rivarola, *J. Phys. B* **42**, 195201 (2009).
  - [30] L. C. Tribedi, P. Richard, L. Gulyás, and M. E. Rudd, *Phys. Rev. A* **63**, 062724 (2001).
  - [31] I. Ben-Itzhak, K. D. Carnes, D. T. Johnson, P. J. Norris, and O. L. Weaver, *Phys. Rev. A* **49**, 881 (1994).
  - [32] A. Salehzadeh and T. Kirchner, *Eur. Phys. J. D* **71**, 66 (2017).

- [33] M. U. Bug, E. Gargioni, H. Nettelbeck, W. Y. Baek, G. Hilgers, A. B. Rosenfeld, and H. Rabus, *Phys. Rev. E* **88**, 043308 (2013).
- [34] E. J. Angelin and R. Hippler, *J. Phys. B* **47**, 225208 (2014).
- [35] W. E. Wilson and L. H. Toburen, *Phys. Rev. A* **11**, 1303 (1975).
- [36] D. J. Lynch, L. H. Toburen, and W. E. Wilson, *J. Chem. Phys.* **64**, 2616 (1976).
- [37] C. A. Tachino, J. M. Monti, O. A. Fojón, C. Champion, and R. D. Rivarola, *J. Phys.: Conf. Ser.* **583**, 012020 (2015).
- [38] L. Gulyás, I. Tóth, and L. Nagy, *J. Phys. B* **46**, 075201 (2013).
- [39] W.-Q. Cheng, M. E. Rudd, and Y.-Y. Hsu, *Phys. Rev. A* **40**, 3599 (1989).
- [40] J. B. Crooks and M. E. Rudd, *Phys. Rev. A* **3**, 1628 (1971).
- [41] B. Hamre, J. P. Hansen, and L. Kocbach, *J. Phys. B* **32**, L127 (1999).
- [42] A. N. Agnihotri, A. H. Kelkar, S. Kasthurirangan, K. V. Thulasiram, C. A. Desai, W. A. Fernandez, and L. C. Tribedi, *Phys. Scr.* **T144**, 014038 (2011).
- [43] A. Mandal and L. Tribedi, *Nucl. Instrum. Methods Phys. Res. Sect. B* **440**, 19 (2019).
- [44] P. D. Fainstein, V. H. Ponce, and R. D. Rivarola, *J. Phys. B* **21**, 287 (1988).
- [45] S. E. Corchs, R. D. Rivarola, and J. H. McGuire, *Phys. Rev. A* **47**, 3937 (1993).
- [46] J. M. Monti, O. A. Fojón, J. Hanssen, and R. D. Rivarola, *J. Phys. B* **43**, 205203 (2010).
- [47] E. Clementi and C. Roetti, *At. Data Nucl. Data Tables* **14**, 177 (1974).
- [48] M. A. Quinto, P. R. Montenegro, J. M. Monti, O. A. Fojón, and R. D. Rivarola, *J. Phys. B* **51**, 165201 (2018).
- [49] D. S. F. Crothers and J. F. McCann, *J. Phys. B* **16**, 3229 (1983).
- [50] C. A. Tachino, J. M. Monti, O. A. Fojón, C. Champion, and R. D. Rivarola, *J. Phys. B* **47**, 035203 (2014).
- [51] M. E. Galassi, C. Champion, P. F. Weck, R. D. Rivarola, O. Fojón, and J. Hanssen, *Phys. Med. Biol.* **57**, 2081 (2012).
- [52] P. D. Fainstein, L. Gulyás, F. Martín, and A. Salin, *Phys. Rev. A* **53**, 3243 (1996).
- [53] See Supplemental Material at <http://link.aps.org/supplemental/10.1103/PhysRevA.102.012819> for numeric data on the double differential cross section.

*Correction:* Processing errors during the review of the manuscript resulted in the omission of the Supplemental Material. It has now been added, along with the corresponding reference and citation.

# Double differential distributions of e-emission in ionization of N<sub>2</sub> by 3, 4 and 5 keV electron impact

Madhusree Roy Chowdhury<sup>1,2</sup>, Dhaval Chauhan<sup>2</sup>,  
Chetan G Limbachiya<sup>2</sup> , Karoly Tókesi<sup>3</sup> , Christophe Champion<sup>4</sup>,  
Philippe F Weck<sup>5</sup> and Lokesh C Tribedi<sup>1,\*</sup> 

<sup>1</sup> Tata Institute of Fundamental Research, Colaba, Mumbai 400005, India

<sup>2</sup> M S University of Baroda, Vadodara 390001, India

<sup>3</sup> Institute for Nuclear Research, ATOMKI, Debrecen, Hungary

<sup>4</sup> Centre Lasers Intenses et Applications (CELIA), Bordeaux University, Talence, France

<sup>5</sup> Sandia National Laboratories, Albuquerque, NM 87185, United States of America

E-mail: [lokesh@tifr.res.in](mailto:lokesh@tifr.res.in) and [ltribedi@gmail.com](mailto:ltribedi@gmail.com)

Received 3 July 2020, revised 31 August 2020

Accepted for publication 5 October 2020

Published 6 November 2020



## Abstract

We report the measurement of the absolute double differential cross sections (DDCS) of secondary electrons emitted due to the ionization of N<sub>2</sub> molecule in collisions with fast electrons having energies between 3 and 5 keV. The emitted electrons with energies from 1–500 eV have been measured for different forward and backward emission angles. The measured DDCS have been compared with the state-of-the-art first Born approximation with correct boundary condition (CB1) model calculations as well as with the classical trajectory Monte Carlo (CTMC) method. From the measured DDCS, the single differential cross sections (SDCS) as a function of the emission energies have been computed and eventually the total ionization cross sections (TCS) have been derived. The TCS values are also compared with a semi-empirical calculation, namely, the CSP-ic (complex scattering potential-ionization contribution) model.

Keywords: ionization, electron impact, di-atomic molecule, DDCS, CB1, CTMC

 Supplementary material for this article is available [online](#)

(Some figures may appear in colour only in the online journal)

## 1. Introduction

The interaction of a charged particle with an atom or molecule provides information about the fundamentals of dynamics involved in the few-body system being investigated. Depending on the energy and charge state of the projectile, different processes can occur between the two collision partners. The impact of electron on an atom or molecule, leading to single ionization of the target has been a subject of study over decades. Different mechanisms like ionization,

excitation, elastic scattering, e–2e process etc [1] have been investigated over several years and many aspects of these processes are yet to be fully understood. The electron impact ionization of target atoms or molecules is not only important for understanding the collision dynamics but is also useful for other fields of research such as, mass spectrometry, plasma physics, astrophysics, stellar atmospheres and radiation chemistry etc [2–4]. Energetic electrons varying from few keV to hundreds of keV are present in the interplanetary medium. In the solar corona, different impulsive solar electron events are observed at energies between 2 and 15 keV. In the solar wind, the electrons have energy in the range from 20–200 keV [5]. In

\* Author to whom any correspondence should be addressed.

addition, the nitrogen molecule deserves a special care since it is one of the residual gas in the fusion reactors. In such devices although the aim is to produce clean plasma to achieve high fusion performance, the impurities, such as, nitrogen or other noble gases are required to protect the plasma facing components from extreme heat loads coming from the hot plasma. The typical energy of electrons in the fusion chamber vary around a few hundreds eV but the complete energy distribution of electrons is very broad ranging up to a few tens of keV. Thus an accurate knowledge of the ionization cross sections by a few keV electron impact is not only important for basic understanding of the collision mechanisms, but also for the wide scale applications in astrophysics and fusion research. In recent times, fast ion and electron impact ionization studies on biomolecules have gained immense importance due to its applicability in cancer treatment using hadron therapy technique [6]. These studies demand a better understanding of the interaction mechanisms involving relatively smaller but multi-electron molecules, such as  $N_2$  or  $O_2$  etc.

Among the different aspects of electron impact ionization study, the determination of total ionization cross sections of atoms and small molecules have been investigated extensively both in the experimental and theoretical framework. The double differential cross section (DDCS) measurements of the electrons emitted from a target atom/molecule provide a detailed understanding of the collision dynamics. Such experimental investigations serve as a powerful tool for testing the accuracy of different theoretical models. Most of the work on electron impact ionization focuses on impact energies varying from threshold to several hundreds of eV, with limited data existing in the higher energy regime [7]. Particularly, the high energy (a few keV) electrons are ideally suited to explore the applicability of the fundamental atomic collision models which are based on the perturbative approach. Some of the earlier work deal with the resonances in e-scattering from the  $N_2$  at much lower energy, i.e., a few eV [8–14]. There are several theoretical and experimental studies on the e-impact ionization cross section [15–29]. However, the studies on the DDCS measurements for electron impact ionization [30–32] are very scarce. Besides providing information about the contribution of the valence shell electrons in the ionization process, the DDCS measurements also provide insight about the ionization from the inner shells of the target molecule. Such diatomic molecules are also well known candidates for studying the quantum mechanical aspects like Young type electron interference effect [33–35].

In this work, we have measured the e-DDCS for ionization of the  $N_2$  molecule in collisions with fast electrons having energies between 3 and 5 keV. The experimentally obtained electron-DDCS have been compared with the two different theoretical models, namely, the CB1 (first Born approximation with correct boundary conditions) and the CTMC calculations. The interpretation of the cross sections for a multielectronic target system is a challenging task for theoretical models. The CB1 approximation has been successfully employed to calculate the ionization cross sections for varieties of large molecules, such as, biomolecules and PAH molecules under the collisions of fast electrons or fast

heavy-ions [36–42]. Furthermore, in order to assess the possible impact of different descriptions of the molecular wave functions on the ionization cross sections, here we have also carried out the *ab initio* calculations by using two different descriptions of the  $N_2$  molecule: the RHF/6-311G and CCSD/cc-pVTZ levels of theory. The main difficulty is caused by the many-body feature of the collision, involving the projectile, target nucleus and target electron(s). The CTMC method has been quite successful in dealing with the ionization process in ion-atom or ion-molecule collisions [43]. One of the advantages of the CTMC method is that the many-body interactions are exactly taken into account during the collisions on a classical level.

The structure of this paper is as following: in section 2 we have provided a brief outline of the experimental arrangement followed by a short note on the theoretical models in section 3. In section 4 we have dealt extensively with the experimental results and their comparison with the model calculations. Finally, the conclusion is added in section 5.

## 2. Experimental details

An electron gun capable of producing fast electrons with energies from 1–10 keV was mounted in a high vacuum chamber which was a 4-way-cross and maintained at a base vacuum of  $\sim 1 \times 10^{-8}$  mbar. A differential pumping assembly was installed after the electron gun chamber. This was followed by the main scattering chamber which was maintained at a base pressure of  $\sim 5 \times 10^{-8}$  mbar. The projectile electrons of energies 3, 4 and 5 keV were used in the present experiment. Two different sets of electrostatic lenses, deflectors and apertures were used to focus and collimate the electron beam. The projectile electrons collided with  $N_2$  gas in the scattering chamber. The scattering chamber was flooded with the target gas at an absolute pressure of 0.1 mTorr which was measured using a capacitance manometer. The differential pumping arrangement was used to maintain the pressure difference between the interaction chamber and the e-gun chamber. The secondary electrons emitted from the target gas were energy analyzed using a hemispherical electrostatic energy analyzer with an extended collimator at the entrance of the analyzer. The energy selected electrons were detected by a channel electron multiplier (CEM) mounted at the exit end of the spectrometer. Extreme cleanliness was maintained inside the scattering chamber in order to avoid any stray electric and magnetic field near the interaction region which would otherwise deflect the low energy electrons. The collection of the lowest energy electrons accurately is difficult since any fringe field could reduce the transmission of these electrons and hence the experimental uncertainties are large in this region. The Earth's magnetic field was reduced to about 10 mG near the interaction region by using suitable  $\mu$  metal shielding inside the scattering chamber. Two layers of thin  $\mu$  metal sheets were used for this purpose. In addition, a pre-acceleration voltage of 6 V was applied at the entrance and exit slits of the analyzer to enhance the collection efficiency of the low energy electrons. The resolution of the spectrometer was about 6%. The front of the CEM was raised to +100 V, since the detection efficiency of CEM remains

constant ( $0.87 \pm 10\%$ ) for electrons with energies between 100 and 600 eV (as known from the user manual of the CEM used [44]). The number of projectiles colliding with the target gas was obtained by measuring the beam current on a long Faraday cup which was electrically isolated from the main scattering chamber. The long Faraday cup was used to stop the flying away of the backscattered electrons from re-entering into the scattering chamber. A LabVIEW based data acquisition system was used for the entire data collection. The secondary electrons having energies from 1–500 eV were detected at 10 different angles between  $30^\circ$  and  $145^\circ$ . For every spectrum, the corresponding background spectrum was also collected in the absence of the gas which was subtracted from the electron spectrum obtained with the target gas. The statistical fluctuations varied from  $\sim 2\%$  for the lowest energy electrons in the forward angles to about  $11\%$  for the highest energy electrons in the backward angles. In addition, the errors are contributed from gas pressure fluctuations ( $\sim 5\%$ ), solid angle path length integral ( $\sim 10\%$ ), resolution of the spectrometer ( $\sim 10\%$ ) and detector efficiency ( $\sim 10\%$ ). The total uncertainties in each DDCCS data was estimated to be about  $18\%$ – $22\%$ . Details about the analysis of the measured spectra is given in [45]. The experimental DDCCS values are provided in a supplementary file (<https://stacks.iop.org/JPB/53/235201/mmedia>).

### 3. Theoretical models

#### 3.1. CB1 model

The present ionization cross sections are calculated within the 1st Born approximation framework by using the partial-wave expansion formalism recently employed for describing the electron-induced ionization of isolated biomolecules [36–39]. In this approach, the incident/scattered electron is described by a plane wave whereas the ejected electron is modelled by a Coulomb wave associated to an effective target charge  $Z_T^* = \sqrt{-2n^2\epsilon}$  where  $n$  refers to the principal quantum number of each atomic orbital component used in the molecular target description (see hereafter) and the active electron orbital energy  $\epsilon$  is related to the ionization energies  $B$  of each occupied molecular orbital by  $\epsilon = -B$ . Besides, it will be assumed that the passive (not ionized) electrons remain as frozen in their molecular orbitals during the collision, which permits us to reduce the electron target interaction potential to a one-active electron potential (see hereafter).

Under these conditions, the triply differential cross sections—hereafter denoted  $\sigma^{(3)}(\Omega_S, \Omega_e, E_e)$ —differential in the direction of the scattered electron  $\Omega_S$ , differential in the direction of the ejected electron  $\Omega_e$  and differential in the ejected energy  $E_e$  may be written as

$$\sigma^{(3)}(\Omega_S, \Omega_e, E_e) = \sum_{j=1}^N \sigma_j^{(3)}(\Omega_S, \Omega_e, E_e) \quad (1)$$

where  $N$  is the number of molecular orbitals used in the description of the target and with  $\sigma_j^{(3)}$  expressed as a weighted sum of the atomic triply differential cross sections  $\sigma_{at,i}^{(3)}(\Omega_S, \Omega_e, E_e)$  corresponding to the different components

involved in the description of the  $N_2$  target ( $N_{1s}$ ,  $N_{2s}$ , and  $N_{2p}$  orbitals), namely,

$$\sigma_j^{(3)}(\Omega_S, \Omega_e, E_e) = \sum_i \xi_{j,i} \cdot \sigma_{at,i}^{(3)}(\Omega_S, \Omega_e, E_e) \quad (2)$$

where the effective number of electrons  $\xi_{j,i}$  as well as the corresponding binding energy are calculated in the gas phase with the Gaussian 09 software (see Frisch *et al* [46]). In order to assess the possible impact of different descriptions of  $N_2$  molecular wave functions on the DDCCS, *ab initio* calculations were carried out at both the RHF/6-311G and CCSD/cc-pVTZ levels of theory. The RHF/6-311G is a rather simple restricted Hartree–Fock description of the target with the medium accuracy Pople basis set 6-311G, while the CCSD/cc-pVTZ description is a more accurate coupled cluster calculation using both single and double substitutions from the Hartree–Fock determinant along with a much larger Dunning’s correlation-consistent polarized basis set with triple-zeta. The first ionization energy corrected for zero-point vibrational energy (ZPE) was 16.900 eV with RHF/6-311G and 16.527 eV with CCSD/cc-pVTZ using Koopman’s theorem. The ionization energy was further constrained to match the experimental value of  $15.581 \pm 0.008$  for  $N_2$  in the gas phase [47].

Thus, in the laboratory framework, the atomic triply differential cross sections  $\sigma_{at,i}^{(3)}$  were calculated from the atomic transition matrix element between the ground state to the 1st ionized level of the target. Then, by using the well-known frozen-core approximation which reduces the present multi-electron problem to a one active electron problem and considering the well-known partial-wave expansion of the plane wave as well as that of the Coulomb wave, the DDCCS could be analytically expressed for each molecular orbital, the target ionization cross sections being simply obtained by summing up all the subshell contributions. Finally, singly differential and total cross sections were obtained after the numerical integrations over the scattering direction and the ejected energy spectrum, respectively.

#### 3.2. CTMC model

The CTMC method is a non-perturbative method, where classical equations of motions are solved numerically [48–51]. In the present work the CTMC simulations were made in the three-body approximation, i.e. the many-electron target atom was replaced by a one-electron atom and the projectile ion was taken into account as one particle [52, 53]. For the target atom a central model potential has been used which is based on the Hartree–Fock method as developed by Green [54]. The potential can be written as:

$$V(r) = q \frac{Z - (N - 1)(1 - \Omega^{-1}(r))}{r} = q \frac{Z(r)}{r}, \quad (3)$$

where  $Z$  is the nuclear charge,  $N$  is the total number of electrons in the atom or ion,  $r$  is the distance between the nucleus and the test charge  $q$ , and

$$\Omega(r) = \frac{\eta}{\xi} (e^{r\xi} - 1) + 1. \quad (4)$$

The potential parameters  $\xi$  and  $\eta$  can be obtained in such a way that they minimize the energy for a given atom or ion [55]. We treat the  $N_2$  molecule as two  $N$  atoms in our simulation and accordingly we use  $\xi = 1.179$  a.u. and  $\eta = 2.27$  a.u. for the  $N$ -atom. Further, this type of potential has certain advantages, because it has a correct asymptotic form for both the small and large values of  $r$ .

In the present CTMC approach, Newton's classical non-relativistic equations of motions for a three-body system are solved numerically for a statistically large number of trajectories for given initial conditions. We have used an ensemble of  $5 \times 10^7$  trajectories. The equations of motion were solved using a standard Runge–Kutta method. A three-body, three-dimensional CTMC calculation is performed as described by Tőkési and Kövér [53]. The initial conditions of the individual collisions are chosen at sufficiently large internuclear separations from the collision center, where the interactions among the particles are negligible. These are selected in a similar fashion as described by Reinhold and Falcon [56] for non-Coulombic systems. A microcanonical ensemble characterizes the initial state of the target. The initial conditions were taken from this ensemble in such a way that initial binding energies of the N(2p) level ( $E_b = -0.5343$  a.u.) and N(2s) level ( $E_b = -1.371$  a.u.) were constrained. For ionization channel the energy and the scattering angles of the particles were recorded. These parameters were calculated at large separation of the projectile and the target nucleus.

The total and double differential cross-sections were computed using the following formulas:

$$\sigma = \frac{2\pi b_{\max}}{T_N} \sum_j b_j^{(i)}, \quad (5)$$

$$\frac{d^2\sigma}{dE d\Omega} = \frac{2\pi b_{\max}}{T_N \Delta E \Delta \Omega} \sum_j b_j^{(i)}. \quad (6)$$

In equations (5)–(6)  $T_N$  is the total number of trajectories calculated for impact parameters less than  $b_{\max}$ , and  $b_j^{(i)}$  is the actual impact parameter for the trajectory corresponding to the ionization process under consideration in the energy interval  $\Delta E$  and the emission angle interval  $\Delta \Omega$  of the electron.

### 3.3. CSP-ic model for TCS

In addition to comparing the data with the CB1 and CTMC models, the total ionization cross section (TCS) data have also been compared with a semi-empirical model, namely the CSP-ic model [22, 57] which is used for calculating the ionization and excitation of varieties of molecules under electron impact. Since it has already been discussed in earlier papers we are providing a brief outline. Initially the total inelastic cross sections are calculated based on a complex scattering potential  $V_{\text{CSC}}$ , constructed using the target molecular charge density which is obtained by a linear combination of the atomic charge densities. This potential can be expressed as:

$$V_{\text{CSC}}(E_i, r) = V_{\text{ST}}(r) + V_{\text{EX}}(E_i, r) + V_{\text{POL}}(E_i, r) + iV_{\text{ABS}}(E_i, r) \quad (7)$$

While the real part of this interaction potential takes into account the static effect ( $V_{\text{ST}}$ ), the exchange ( $V_{\text{EX}}$ ) between the projectile and a target electron and the polarization ( $V_{\text{POL}}$ ) of the charge density cloud, the imaginary part is an absorption term ( $V_{\text{ABS}}$ ) [59], responsible for the loss of scattered flux into the allowed channels of electronic excitation and ionization [58]. The partial wave approach under the spherical approximation is used to calculate the complex phase shifts  $\delta_l(k)$  which carry the signature of the interaction between the incident electrons and the molecule [60]. To compute the TCS we define a ratio between total ionization cross section and total inelastic cross sections,  $R(E_i)$  [57], such that,

$$R(E_i) = 1 - c_1 \left( \frac{c_2}{U+a} + \frac{\ln U}{U} \right) \quad (8)$$

where  $U = \frac{E_i}{I}$ ,  $E_i$  is impact energy and  $I$  is the ionization potential of the target. We evaluate the three constants  $c_1$ ,  $c_2$  and  $a$  to obtain  $R(E_i)$  and hence the total ionization cross sections.

## 4. Results and discussions

### 4.1. Energy distribution at fixed emission angles

Figure 1 displays the absolute DDCS of the secondary electrons emitted from  $N_2$  in collisions with 3 keV electrons. The DDCS spectra are shown for six different emission angles. The spectra fall by about four orders of magnitude in the measured emission energy range between 1 and 500 eV. The cross section is maximum in the lowest energy range corresponding to the soft collision mechanism and then falls rapidly with the increase in the emission energies. The soft collision mechanism involves very little momentum transfer from the projectile to the bound electrons of the target and hence these electrons are emitted for large impact parameter collisions. The intermediate part of the spectrum is normally dominated by the two-centre effect where the ejected electron is under the influence of both the projectile and the positively charged recoil target-ion. However, in case of electrons as projectiles, two centre effect does not play a major role unlike the case for a typical ion-molecule collision. The sharp peak observed at  $\sim 350$  eV corresponds to the K-LL Auger electron emission. The measured DDCS have been compared with the CB1 model calculations. The calculations have been performed using two different descriptions of the target wave functions at the RHF/6-311G and CCSD/cc-pVTZ levels of the theory. Both the calculations have been shown in figure 1 (solid and dash-dot-dot lines) and it is seen that in the log–log scale, the two models almost merge with each other. This suggests that the description of the target wave functions has very limited impact on the DDCS in the energy range considered here. In case of the forward angles, the CB1 model calculations underestimate the data upto about 60 eV, beyond which it shows overall good agreement with the data. For the intermediate angles, around  $90^\circ$ , the theory matches qualitatively and quantitatively with the measured DDCS above 50 eV. However, in case of backward angles, the model underestimates

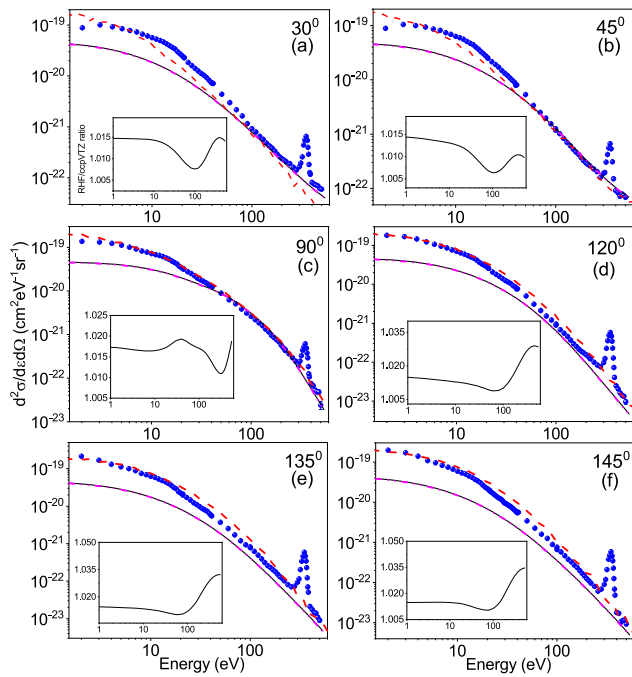


**Figure 1.** Absolute e-DDCS of N<sub>2</sub> in collisions with 3 keV electrons: The lines corresponding to the CB1 calculations with the RHF/6-311G (black solid line) and the CCSD/cc-pVTZ (magenta dash-dot-dot line) descriptions of the target wave function. The difference between these two calculations are too small and therefore the ratio between them are shown in the insets. The CTMC model calculations for 2N are shown by the red dashed lines.

the data over the entire spectra, with maximum discrepancy occurring in the low emission energies. The ratio between the CB1 predictions using two different wave functions is found to vary very little i.e. from 1.01 in the forward angles to 1.04 for the higher backward angles (see insets in figure 1). The experimental data have also been compared with CTMC model calculations for twice the atomic nitrogen or 2N (red dashed line). Overall an excellent agreement is observed with this model over the entire energy regime. In figures 2 and 3, we have shown the energy dependence of the e-DDCS for the projectile energies 4 and 5 keV, respectively. In both the cases the CTMC model is seen again to match well with the data points except for the lowest energy electrons, where it predicts slightly higher cross sections. On the other hand, the CB1 model show a good qualitative agreement reproducing the shape of the energy distribution accurately. However, this model quantitatively underestimates the data below 70 eV for all the angles. For higher beam energy i.e. at 5 keV (figure 3) the CB1 model although predicts somewhat different cross sections from the experiment, but the difference is quite less compared to that for the 3 keV and 4 keV electron beam. The insets in each panel in figures 2 and 3 show the magnified view of the K-LL Auger peak.

Figure 4 displays the theoretical (CB1) DDCS values as a function of the ejected electron energy for various emission angles. The calculated values are shown for incident electron energy of 3 keV. It may be noticed that in the low energy region, all the curves corresponding to the different

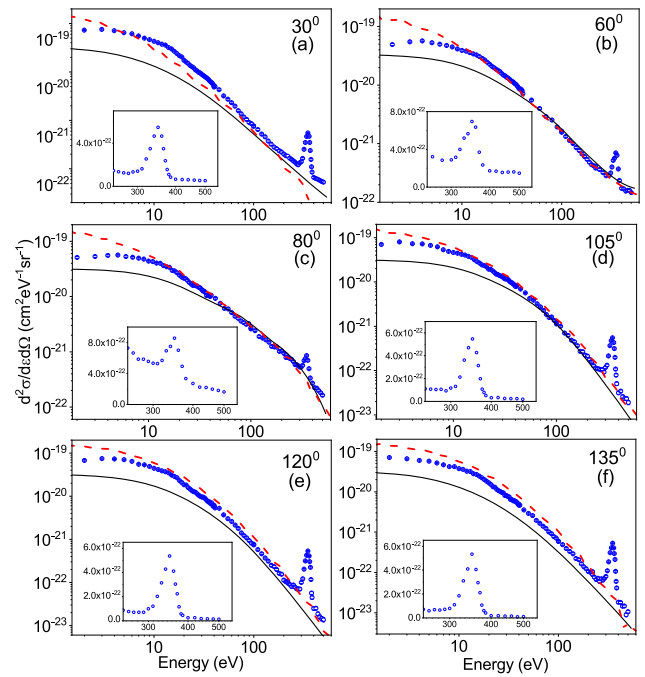


**Figure 2.** DDCS of secondary electrons in case of 4 keV projectile electrons. The CB1 calculations (with RHF/6-311G wavefunction) are shown by black solid lines. The CTMC calculations are shown by red dashed lines. Inset: K-LL Auger peak of nitrogen for each emission angle.

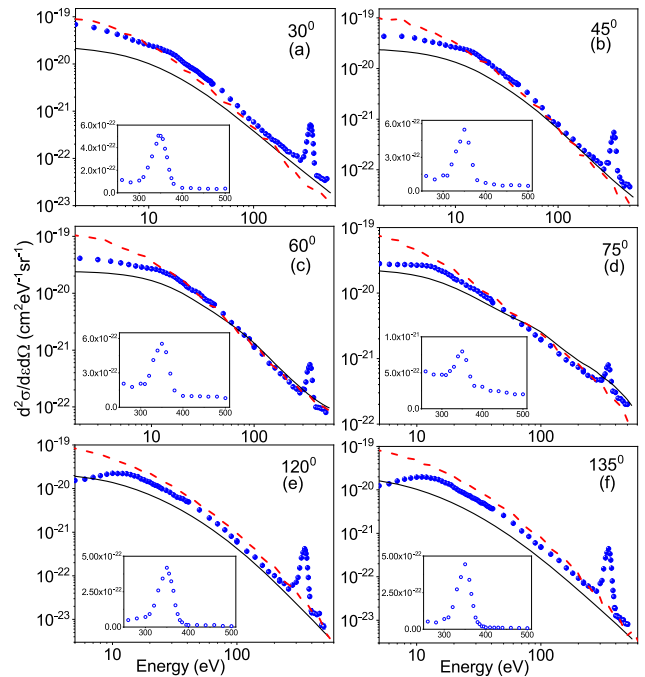


**Figure 3.** Similar to figure 2, except for 5 keV electrons.

emission angles bunch together. This region is dominated by the soft collision mechanism for which the DDCS remains almost independent of the emission angles. With the increase in the emission energies, the spectra corresponding to the intermediate angles, (i.e., 75°, 80° and 90°) start going up whereas the spectra for the forward and backward angles show a steady

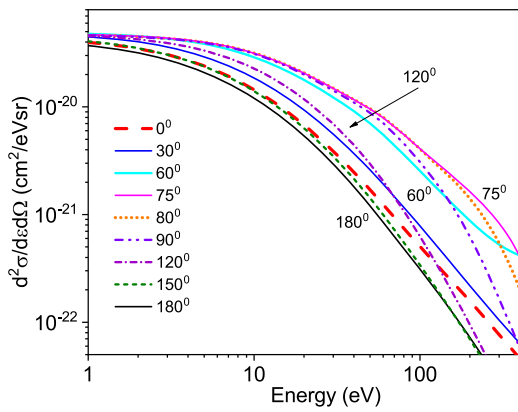


**Figure 4.** Theoretical (CB1) DDCS for different emission angles for 3 keV electron beam.

fall. The separation among different lines represent the angular distributions.

#### 4.2. Angular distribution at fixed emission energies

To have a better understanding of the features seen in figure 4, the absolute DDCS of the ejected electrons as a function of different emission angles have been displayed in figure 5 corresponding to the projectile beam energy of 3 keV. The six plots shown in figure 5 expand over the entire emission energy range revealing the signature of different features at different parts of the spectrum. In figure 5(a) an almost flat distribution is observed corresponding to the soft collision mechanism which is dominated by large impact parameter events. For higher electron emission energies, a peak like structure starts appearing around 80° which sharpens further with the increase in the emission energies. This peak is due to the binary nature of collision i.e. the direct two-body free-electron scattering between the incident electron and the target electron while the recoil-ion remains passive. The CB1 model (black solid and magenta dash-dot-dot lines) show a qualitative agreement only but quantitatively underestimates the data, except in the peak region, where it matches well with the measured quantities. With the increase in the emission energies, it is seen that the DDCS values for the forward angles are slightly higher compared to those for the backward angles. For ejected electron energy 160 eV (figure 5(d)), the measured DDCS for forward angle is 1.6 times higher compared to the backward angle, whereas for 260 eV, the difference goes up to 2.6 times (figure 5(f)). These numbers, i.e. forward-backward angular asymmetry parameters, are close to that predicted by the CB1 model.

It is seen that the CTMC model show very good agreement with the data at 7 eV (figure 5(a)). However, with increase in emission energies, it is observed that the CTMC model predicts a higher cross section for the backward angles compared to that for the forward angles. Thereby the forward-backward angular asymmetry is not reproduced properly by the CTMC model unlike the cases for the experimental measurements and the CB1 model. Similar features are also observed for the impact energies of 4 keV (figure 6) and 5 keV (figure 7). In order to understand and correct this behavior we made some

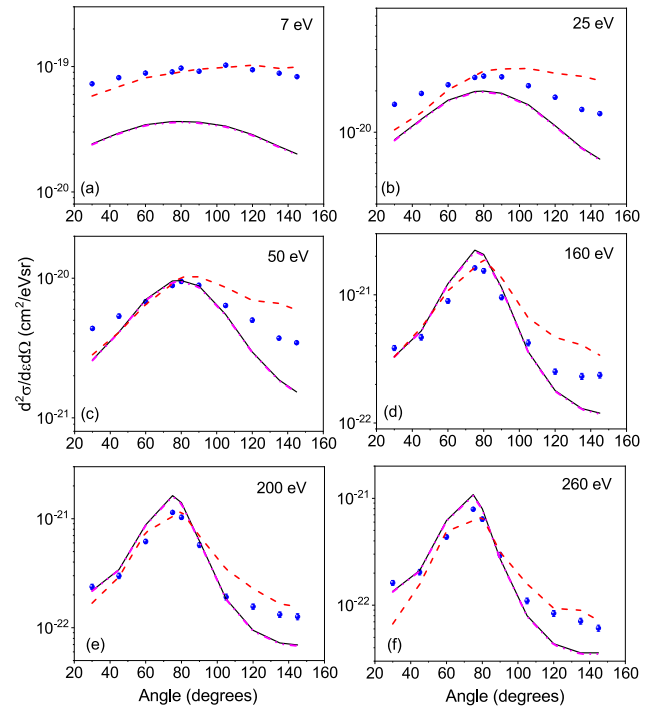


**Figure 5.** Angular distributions of e-DDCS for fixed secondary electron energies in case of incident energy 3 keV. Black solid and magenta dash-dot-dot lines represent the CB1(RHF/6-311G) and CB1(CCSD/cc-pVTZ), respectively. The CTMC calculations are shown by red dashed lines.

initial tests on the strength of the projectile electron and target electron interactions as modelled in the CTMC approach. As a result of the standard calculations (shown in the figures), the interaction between the two electrons is kept ‘ON’ during the entire motion of the particles till the asymptotic limit. However, as a initial test we also performed the simulations by switching off the e–e interaction in the exit channel. This indicated certain improvement in the distribution. However, further systematic calculations are required to be performed to improve the angular distribution. We conclude that the present CTMC model overestimate the strength of the electron–electron interactions particularly in the exit channel. The projectile electron sweep out the ejected target electron from the forward angles to the backward ones. The detailed analysis of this effect is in progress and will be published elsewhere.

#### 4.3. Single differential cross section

Integrating the e-DDCS spectrum over the emission energy or emission angle gives us the SDCS. Integrating over the emission energies, we obtain the SDCS i.e.  $d\sigma/d\Omega_e$ , as a function of angles which is given by:

$$\frac{d\sigma}{d\Omega_e} = \int \frac{d^2\sigma}{d\Omega_e d\epsilon_e} d\epsilon_e. \quad (9)$$

Similarly, integrating over the emission angles, we get the SDCS as a function of the emission energy:

$$\frac{d\sigma}{d\epsilon_e} = \int \frac{d^2\sigma}{d\epsilon_e d\Omega_e} d\Omega_e. \quad (10)$$

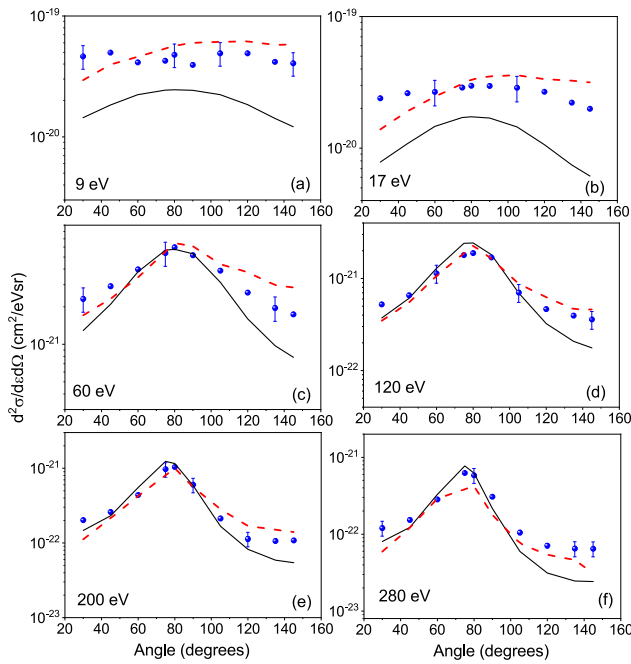


**Figure 6.** Similar to figure 5, shown for 4 keV electrons. The absolute errors are shown for some data points.

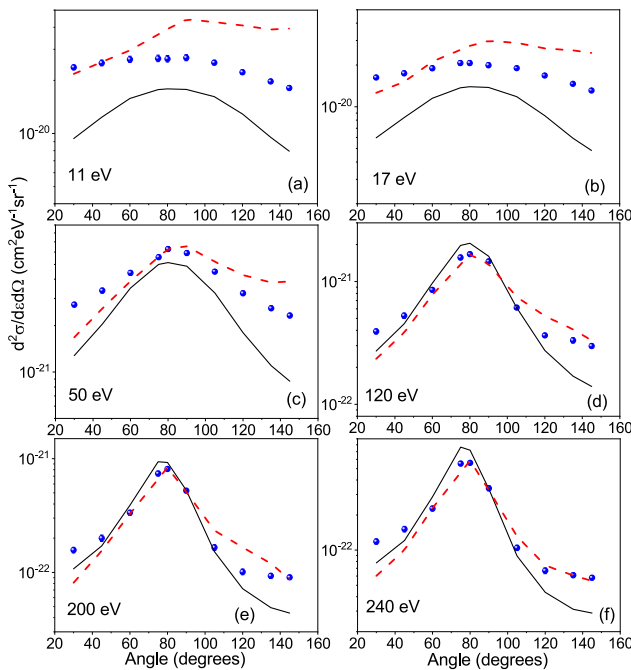


**Figure 7.** Similar to figure 5 for incident energy 5 keV.

Figure 8 displays the SDCS i.e.,  $d\sigma/d\epsilon_e$  as a function of the emission energies corresponding to 3, 4 and 5 keV incident energies. For all the three beam energies, the CB1 model predicts lower cross sections compared to the data upto  $\sim 50$ – $60$  eV, beyond which one can observe a very good agreement. The discrepancy is largest for incident energy 3 keV and least for the 5 keV electrons. The measured DDCS have also been compared with the CTMC model (red dashed line). Overall an excellent agreement is observed with the CTMC

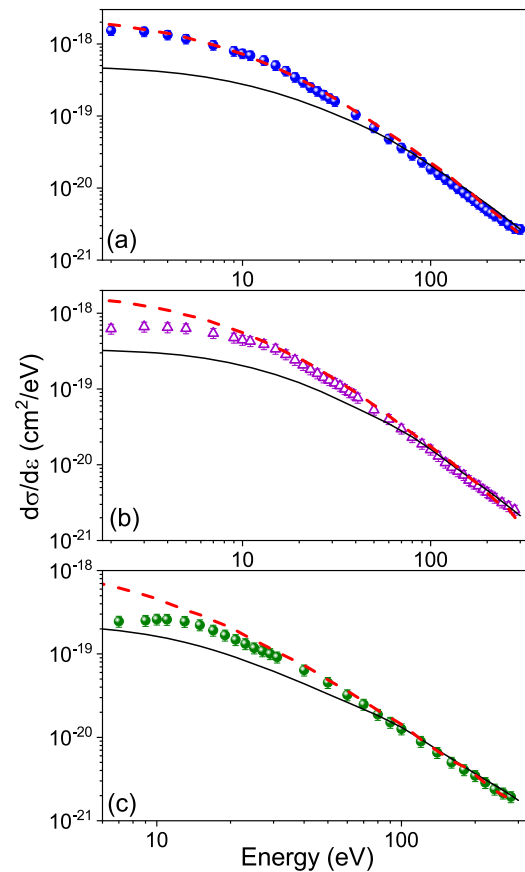


**Figure 8.**  $d\sigma/d\epsilon$  as a function of emission energies for (a) 3, (b) 4 and (c) 5 keV incident energies; data compared with CTMC (red dashed line) and CB1 (black solid line) models.

model over the entire energy regime for all the three beam energies under investigation. However, in case of 4 and 5 keV (see figures 8(b) and (c)), the model overestimates the data for the lowest energy electrons only by a little amount.

#### 4.4. Total ionization cross section

Integrating the SDCS over the emission energies or emission angles gives the total ionization cross section. The TCS were obtained by integrating over the electron energies between 1 and 500 eV and over the emission angles from  $\theta = 0^\circ$  to  $\theta = 180^\circ$ . The data points below  $30^\circ$  and above  $145^\circ$  were estimated by extrapolation to obtain the total cross section and the difference was found to be about 11%–13%. It was observed that the TCS values derived by integrating the SDCS over the emission angles and energies varied very little i.e. only by  $\sim 0.3\%$ – $0.4\%$ . In figure 9, the experimental and theoretical TCS values have been displayed which includes the data obtained for the incident energies of 7 keV [61] as well as for the 6 and 8 keV [62]. The total contribution of the K-shell ionization ( $\sigma_{K-LL}$ ) for 3, 4 and 5 keV beam energies are 0.23 Mb, 0.21 Mb and 0.19 Mb, respectively, whereas, the TCS at these three energies were found to be 26.3 Mb, 16.8 Mb and 14.2 Mb.

From figure 9 it is seen that the CB1 model falls well below the present experimental data but provides an excellent

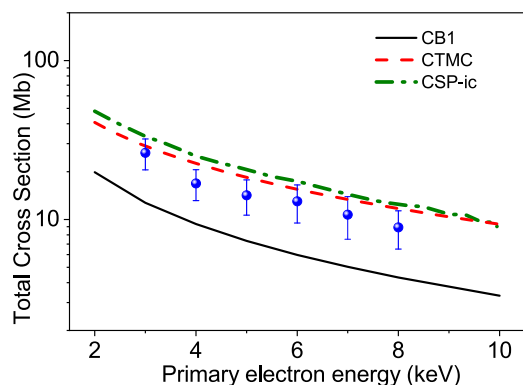


**Figure 9.** Total ionization cross section as a function of incident electron energy along with the predictions of three different models, i.e. the CB1, CTMC and CSP-ic.

qualitative agreement with the observed energy-dependence. The CTMC model, on the other hand, falls a bit higher compared to most of the data points but mostly within the experimental uncertainties which are about 22%–27%. The present TCS values are found to be lower than the existing data [7] by about 20% to 40% (not shown). The CTMC calculations also fall below these existing data and the difference increases for higher energy. The CB1 model is closer to the present measurements and has a large deviation from the existing data. The TCS values predicted by the CSP-ic model overestimates the measured data for all the energies, but provides a good qualitative behavior regarding the energy dependence. This discrepancy could be due to the consideration of the spherical charge density of the  $N_2$  molecule and other approximations [63] used in the semi-empirical model. It is to be noted that the TCS calculations obtained using the two *ab initio* models, (CB1 and CTMC), lie below and just above the experimental values, respectively. The CTMC model provides closest agreement to the present data.

## 5. Conclusions

We have measured the absolute DDCS, SDCS and TCS of the secondary electron emission in ionization of  $N_2$  under the impact of 3, 4 and 5 keV fast electrons for emission angles between  $30^\circ$  and  $145^\circ$ . The experimental DDCSs spectra have been compared with the CB1 model calculations with two different target wave functions as well as with the CTMC model for twice of atomic nitrogen. No significant difference has been observed between the two sets of the CB1 model calculations corresponding to the two wave functions at the RHF/6-311G and CCSD/cc-pVTZ levels of theory. This suggests that the description of the target wave functions have very limited impact on the DDCS in the energy range considered here. The CTMC model provided a very good agreement with the measured data for the entire emission spectra except for certain energy-angle window region. The CB1 model predicted lower cross section values compared to the experimental data for all emission energies, with maximum discrepancy lying in the low emission energy region. Although the CTMC gives the closest representation to the experimental values, the

forward-backward angular asymmetry of the DDCS is not reproduced properly by the CTMC model unlike the CB1 model and hence further investigations are required. The derived TCS values have been compared both with the *ab initio* CB1 and CTMC calculations as well as with the semi-empirical CSP-ic model. While qualitatively both the CB1 and the CSP-ic models show similar energy dependence, the CTMC gives the closest representation to the measured TCS values within experimental uncertainties.

## Acknowledgment

One of the authors (M R C) would like to acknowledge the financial assistance from CSIR for the execution of this project. We acknowledge the technical support provided by Mr Nilesh Mhatre and Mr. W Fernandes. Sandia National Laboratories is a multi-mission laboratory managed and operated by National Technology and Engineering Solutions of Sandia, LLC., a wholly owned subsidiary of Honeywell International, Inc., for the US Department of Energy's National Nuclear Security Administration under Contract DE-NA0003525. The views expressed in the article do not necessarily represent the views of the US DOE or the United States Government.

## ORCID iDs

Chetan G Limbachiya  <https://orcid.org/0000-0003-2845-1244>

Karoly Tórkési  <https://orcid.org/0000-0001-8772-8472>

Lokesh C Tribedi  <https://orcid.org/0000-0002-9282-9734>

## References

- [1] Mark T D and Dunn G H (ed) 1985 *Electron Impact Ionization* (Wien: Springer)
- [2] Bartschat K and Kushner M J 2016 *Proc. Natl Acad. Sci.* **113** 7026
- [3] Becker K H and Tarnovsky V 1995 *Plasma Sources Sci. Technol.* **4** 307
- [4] Janev R K (ed) 1995 *Atomic and Molecular Processes in Fusion Edge Plasmas* (New York: Plenum)
- [5] Jeffrey N L S, Kontar E P and Fletcher L 2019 *Astrophys. J.* **880** 136
- [6] Sanche L 2005 *Eur. Phys. J. D* **35** 367
- [7] Schram B L, De Heer F J, van der Wiel M J and Kistemaker J 1965 *Physica* **31** 94
- [8] Golden D E 1966 *Phys. Rev. Lett.* **17** 847
- [9] Mathur D and Hasted J B 1977 *J. Phys. B: At. Mol. Phys.* **10** L265
- [10] Weatherford C A and Temkin A 1994 *Phys. Rev. A* **49** 2580
- [11] Morgan L A 1986 *J. Phys. B: At. Mol. Phys.* **19** L439
- [12] Kennerly R E 1980 *Phys. Rev. A* **21** 1876
- [13] Sun W, Morrison M A, Isaacs W A, Trail W K, Alle D T, Gulley R J, Brennan M J and Buckman S J 1995 *Phys. Rev. A* **52** 1229
- [14] Garcia G, Perez A and Campos J 1988 *Phys. Rev. A* **38** 654
- [15] Schram B L, Moustafa H R, Schutzen J and De Heer F J 1966 *Physica* **32** 734
- [16] Rapp D and Englander-Golden P 1965 *J. Chem. Phys.* **43** 1464
- [17] Straub H C, Renault P, Lindsay B G, Smith K A and Stebbings R F 1996 *Phys. Rev. A* **54** 2146

- [18] Hwang W, Kim Y K and Rudd M E 1996 *J. Chem. Phys.* **104** 2956
- [19] Madison D H and Al-Hagan O 2010 *J. Phys. B: At. Mol. Opt. Phys.* **2010** 1
- [20] Margreiter D, Deutsch H, Schmidt M and Mark T D 1990 *Int. J. Mass Spectrom. Ion Process.* **100** 157
- [21] Mark T D 1975 *J. Chem. Phys.* **63** 3731
- [22] Joshipura K N, Gangopadhyay S S, Kothari H N and Shelat F A 2009 *Phys. Lett. A* **373** 2876
- [23] Deutsch H, Becker K, Matt S and Mark T D 2000 *Int. J. Mass Spectrom.* **197** 37
- [24] Hudson J E, Hamilton M L, Vallance C and Harland P W 2003 *Phys. Chem. Chem. Phys.* **5** 3162
- [25] Toth I, Campeanu R I, Chis V and Nagy L 2008 *Eur. Phys. J. D* **48** 351
- [26] Freund R S, Wetzel R C and Shul R J 1990 *Phys. Rev. A* **41** 5861
- [27] Keiffer I J and Dunn G H 1966 *Rev. Mod. Phys.* **38** 1–35
- [28] Kim Y K and Desclaux J-P 2002 *Phys. Rev. A* **66** 012708
- [29] Itikawa Y 2006 *J. Phys. Chem. Ref. Data* **35** 31
- [30] Opal C B, Peterson W K and Beaty E C 1971 *J. Chem. Phys.* **55** 4100
- [31] Opal C B, Beaty E C and Peterson W K 1972 *At. Data Nucl. Data Tables* **4** 209
- [32] Goruganthu R R, Wilson W G and Bonham R A 1987 *Phys. Rev. A* **35** 540
- [33] Chatterjee S, Kasthurirangan S, Kelkar A H, Stia C R, Fojón O A, Rivarola R D and Tribedi L C 2009 *J. Phys. B: At. Mol. Opt. Phys.* **42** 065201
- [34] Roy Chowdhury M, Stia C R, Tachino C A, Fojon O A, Rivarola R D and Tribedi L C 2016 *Phys. Rev. A* **94** 052703
- [35] Gao J, Madison D and Peacher J L 2005 *Phys. Rev. A* **72** 032721
- [36] Champion C, Hanssen J and Hervieux P-A 2004 *J. Chem. Phys.* **121** 9423
- [37] Milne-Brownlie D S, Cavanagh S J, Lohmann B, Champion C, Hervieux P-A and Hanssen J 2004 *Phys. Rev. A* **69** 032701
- [38] Champion C, Dal Cappello C, Houamer S and Mansouri A 2006 *Phys. Rev. A* **73** 012717
- [39] Champion C 2013 *J. Chem. Phys.* **138** 184306
- [40] Agnihotri A N *et al* 2012 *Phys. Rev. A* **85** 032711
- [41] Agnihotri A N, Nandi S, Kasthurirangan S, Kumar A, Galassi M E, Rivarola R D, Champion C and Tribedi L C 2013 *Phys. Rev. A* **87** 032716
- [42] Biswas S, Champion C, Weck P F and Tribedi L C 2017 *Sci. Rep.* **7** 5560
- [43] Jorge A, Horbatsch M, Illescas C and Kirchner T 2019 *Phys. Rev. A* **99** 062701
- [44] *Channel Electron Multiplier* (Germany: Dr. Sjuts Optotechnik GmbH)
- [45] Chowdhury M R and Tribedi L C 2017 *J. Phys. B: At. Mol. Opt. Phys.* **50** 155201
- [46] Frisch M J *et al* 2009 *Gaussian 09, Revision A.02* Gaussian, Inc Wallingford
- [47] Trickl T, Cromwell E F, Lee Y T and Kung A H 1989 *J. Chem. Phys.* **91** 6006
- [48] Abrines R and Percival I C 1966 *Proc. Phys. Soc.* **88** 861
- [49] Olson R E and Salop A 1977 *Phys. Rev. A* **16** 531
- [50] Tőkési K and Hock G 1994 *Nucl. Instrum. Methods Phys. Res. B* **86** 201–4
- [51] Tőkési K and Hock G 1996 *J. Phys. B: At. Mol. Opt. Phys.* **29** L119–25
- [52] Tőkési K and Kövér Á 1999 *Nucl. Instrum. Methods Phys. Res. B* **154** 259–62
- [53] Tőkési K and Kövér Á 2000 *J. Phys. B: At. Mol. Opt. Phys.* **33** 3067–77
- [54] Green A E S 1973 *Adv. Quantum Chem.* **7** 221
- [55] Garvey R H, Jackman C H and Green A E S 1975 *Phys. Rev. A* **12** 1144
- [56] Reinhold C O and Falcon C A 1986 *Phys. Rev. A* **33** 3859
- [57] Joshipura K N, Vinodkumar M, Limbachiya C G and Antony B K 2004 *Phys. Rev. A* **69** 022705
- [58] Swadia M, Thakar Y, Vinodkumar M and Limbachiya C 2017 *Eur. Phys. J. D* **71** 85
- [59] Staszewska G, Schwenke D W, Thirumalai D and Truhlar D G 1983 *Phys. Rev. A* **28** 2740
- [60] Vinodkumar M, Limbachiya C, Barot A and Mason N 2013 *Phys. Rev. A* **87** 012702
- [61] Roy Chowdhury M, Stia C R, Tachino C A, Fojon O A, Rivarola R D and Tribedi L C 2017 *Eur. Phys. J. D* **71** 218
- [62] Tribedi L C *et al* unpublished
- [63] Limbachiya C, Vinodkumar M, Swadia M and Barot A 2014 *Mol. Phys.* **112** 101

**Radiobiological effectiveness of iodouracil and the influence of atomic giant resonance**Anuvab Mandal,<sup>1</sup> Madhusree Roy Chowdhury,<sup>1</sup> Chandan Bagdia,<sup>1</sup> Juan M. Monti,<sup>2</sup> Roberto D. Rivarola,<sup>2</sup> P. F. Weck,<sup>3</sup> and Lokesh C. Tribedi<sup>1,\*</sup><sup>1</sup>*Department of Nuclear and Atomic Physics, Tata Institute of Fundamental Research, 1 Homi Bhabha Road, Colaba, Mumbai 400005, India*<sup>2</sup>*Instituto de Física Rosario (CONICET-UNR), Universidad Nacional de Rosario, 2000 Rosario, Argentina*<sup>3</sup>*Sandia National Laboratories, Albuquerque, New Mexico 87185, USA*

(Received 21 April 2020; accepted 12 November 2020; published 14 December 2020)

Hadron therapy combined with nanotechnology has been proposed as an elegant alternative for cancer treatment. Internal amplification of electron emission causing radiobiological effectiveness in nanoinserted biomolecules is of prime importance and has been measured here for the iodouracil molecule. Our experiment involves the measurement of angle and energy resolved double differential cross section (DDCS) of electron emission from iodouracil and uracil (and also water) in collisions with fast  $C^{6+}$  ions. The electron emission from iodouracil is substantially enhanced over that from uracil or water. The enhancement is much larger than the state-of-the-art model for Coulomb ionization based on the continuum distorted wave-eikonal initial state (CDW-EIS) approximation. The electron sensitizing factor ( $\approx 2.4$ ) is in excellent agreement with the strand-breaking sensitizing factor ( $\approx 2.0$ ) for metal nanoparticle embedded in a DNA. The enhancement is explained in terms of collective excitation of strongly correlated 4d electrons, known as atomic giant dipole resonance (GDR) in I atoms. The GDR contribution to the enhancement is derived, which is in excellent agreement with recent theoretical prediction, thereby providing conclusive experimental evidence of the crucial role of collective excitation in radio sensitization.

DOI: [10.1103/PhysRevA.102.062811](https://doi.org/10.1103/PhysRevA.102.062811)**I. INTRODUCTION**

Hadron therapy, which relies on charged-particle beams to treat large cancerous tumors or those resistant to conventional therapies, can be elegantly combined with nanotechnology through the use of nanosensitizers to increase cancer cells' sensitivity toward radiotherapy [1,2]. The study of interaction of the biomolecules and water with fast ions is of immense importance for its application in radiobiology as well as molecular collision physics [3–15]. The high-energy ion-beam induced cancer therapy has the added advantage of delivering a higher dose directly to the target region, in comparison to the conventional photon therapy. A large number of low-energy electrons are emitted in such interaction with biological matter including biomolecules and water. Most of these secondary electrons are emitted near the end of the projectile's trajectory where the energy loss exhibits a peak known as the Bragg peak [16]. It is now well known that the lowest energy electrons (up to about 30 eV) are efficient at breaking the DNA or RNA strands of the cancerous cells through dissociative electron attachment (DEA) [17–20]. A major goal of radiotherapy is to enhance the radiobiological effectiveness, i.e., to generate the same or required amount of damage to the cancerous cells with relatively lower dosage of the ion-beam radiation. Metal nanoparticles (NPs), made of hundreds or thousands of Pt or Au atoms, have been proposed as candidates for radio sensitizers; for example, see, Refs. [21–23]. The most important parameter is the sensitizing factor, i.e., the ratio of

the single-strand break (SSB) (or double-strand break, DSB) event with and without an NP in the DNA.

This factor is closely related to the enhancement of low-energy electron emission in the presence of such inserted atoms. The sensitizing factor or radiobiological effectiveness for the isolated Pt atom attached in a plasmid DNA is found to be  $\approx 1.6$  [21] and that for inserted Au NP is  $\approx 2.0$  [22]. The influence of plasmon excitation to provide enhancement in e-emission has been addressed in experiments involving  $C_{60}$ -fullerene [24–26] as well as in models involving metal nanoparticles by Solovyov and coworkers [2,27]. This model has also predicted enhancements due to the atomic giant resonance (GDR) for which there has not been any quantitative measurement. It was shown that insertion of a 3-nm-diameter Pt NP provides an efficient way to induce lethal damage in DNA. However, the sensitizing effect, in terms of the enhancement of electron yields for such inserted NPs or a metallic atom, has yet to be investigated experimentally. We present here the measurement of the sensitizing factor  $F_S$  using an iodouracil molecule.

The class of 5-halouracil molecules ( $C_4H_3XN_2O_2$ ,  $X = F, Cl, Br, I$ ) are structurally similar to uracil ( $C_4H_4N_2O_2$ ), which is one of the RNA base molecules. Iodouracil is obtained by replacing one of the H atoms of uracil by an I atom. Collision studies using iodouracil (as well as other halouracil molecules) can be enlightening toward the search for a radio sensitizer. A few studies on the low-energy electron induced radio sensitivity through DEA [28–31] are available in the literature. The dehalogenation of halouracils by proton impact has been studied by Champeaux *et al.* [32]. The e-emission spectra from the uracil molecule in collisions with fast protons

\*Corresponding author: [lokesh@tifr.res.in](mailto:lokesh@tifr.res.in)

and bare carbon ions have been studied by Itoh *et al.* [33] and Agnihotri *et al.* [34].

Iodine is known to exhibit atomic giant dipole resonance (GDR) involving the  $4d \rightarrow \epsilon f$  excitation in response to the electromagnetic field [35–39]. Similar GDR has been known to exist also for Xe [40–42] and has been predicted [2] for other metal elements such as Ag, Au, and Pt. The resonance is associated with the collective dipolar oscillatory motion of the entire 4d-shell electrons [35]. Such resonances are strongly damped and decay typically within one period of oscillation [43]. The resonance primarily decays by emission of low-energy electrons. For iodine [39], the GDR occurs at an energy around  $\approx 90$  eV with a width of  $\approx 40$  eV which is also studied in other I-based compounds (i.e.  $\text{CH}_3\text{I}$ ,  $\text{I}_2$ , HI, etc.) [39].

In this article, the e-emission cross sections from 5-iodouracil as well as uracil upon the impact of 5.5-MeV/u C ions are presented. The angular and energy distributions of the e-DDCS ( $d^2\sigma/d\Omega d\epsilon$ ), i.e., ionization cross sections differential in both the solid angle ( $\Omega$ ) and the ejected electron energy ( $\epsilon$ ) are measured. Experimental results are compared with the *ab initio* and state-of-the-art quantum mechanical model based on the continuum distorted wave-eikonal initial state (CDW-EIS) approximation [44]. The total electron emission cross section (TCS), derived by integrating the DDCS over electron energy and emission angles, are also compared with that for the similar results for ionization of water molecule, measured recently.

## II. EXPERIMENTAL PROCEDURE

The details of the experimental techniques are given elsewhere [24,34,45]. In brief, a well-collimated beam of bare C ions with 5.5 MeV/u of energy was obtained from the BARC-TIFR Pelletron accelerator which collided with the targets of iodouracil in a scattering chamber with a base pressure less than  $1 \times 10^{-7}$  mbar. The target was prepared by heating the powder sample in an oven assembly inside the scattering chamber. A nozzle of aspect ratio (length-to-diameter ratio) 10 and of diameter 1.5 mm was used to obtain the effusive vapor jet. The temperature of the oven was raised very slowly, i.e., over a period of  $\approx 24$  hours to  $\approx 120^\circ\text{C}$  to get a sufficient vapor density. Under dry conditions, complete DNA degradation occurs at above  $190^\circ\text{C}$  [46]. Previous studies [32] on fragmentation of different halouracils clearly indicate that there is no thermal decomposition of the sample at  $\approx 120^\circ\text{C}$ . The uniform flow of molecules is ensured by monitoring the deposition rate on a quartz crystal based thickness monitor. The variation in the deposition rate is found to be less than 10%.

The ejected electrons are energy analyzed and detected using an electrostatic hemispherical analyzer with a channel electron multiplier (CEM) detector [47]. A positive voltage of 100 V is applied to the CEM front in order to achieve a uniform detection efficiency ( $\approx 0.9$ ) throughout the detection energy range. The residual electric and magnetic fields, in the interaction region, which were reduced drastically can affect the trajectories of the very-low-energy electrons ( $< 5$  eV). In order to increase the collection efficiency of these electrons, a small preacceleration voltage of 6 V is applied to the entrance and exit apertures of the spectrometer. Additionally,

two  $\mu$ -metal sheets are placed inside the chamber along its inner surface in order to reduce the Earth's magnetic field drastically. The energy resolution of the spectrometer depends mainly on the exit-slit width and the acceptance angle of the entrance slit and is found to be 6% of the detected electron energy.

Electron yields are measured in the range from 1 to 340 eV at different emission angles ranging from  $20^\circ$  to  $160^\circ$ . Background spectra are also recorded. A separate set of experiment was performed with the  $\text{CH}_4$  gas under static pressure condition and the carbon KLL Auger electron spectrum has been used for the normalization to obtain the absolute DDCS values for the iodouracil, as given in Refs. [24,34,45]. The total uncertainty in the deduction of the absolute values of the DDCS is  $\approx 25$ –30%, primarily arising from the vapor density fluctuation  $\approx 10\%$ , the normalization procedure (15–18%), the statistical uncertainty ( $\approx 5\%$ ), solid-angle path length (8–10%), etc.

## III. THEORETICAL DESCRIPTION

An independent particle approximation is employed to describe the single ionization reaction. The treatment of the case of atomic targets [48] is extended to the case of molecular ones. It means that only one electron of each one of the molecular orbitals is considered to be promoted to a continuum state whereas all the other target electrons (the passive electrons) are considered to remain as frozen in their initial states. This procedure is then applied to each one of the molecular orbitals. The dynamics of the process is described within the prior form of the continuum distorted wave-eikonal initial state (CDW-EIS) formalism. The straight line version of the impact parameter approximation is used for the calculations [49].

The interest is focused only in the spectra of the final ejected electron parameters (energy and angle), considering that the contribution of all molecular orientations are averaged. Thus, it is assumed that the interaction between the projectile and the passive electrons does not affect the ionization process itself and the corresponding potentials can be eliminated from the total electronic Hamiltonian [48].

Into the CDW-EIS model the initial and final distorted wave functions for each one of the molecular orbitals are chosen as

$$\chi_i^+ = \varphi_i \exp\left[-i\frac{Z_P}{v} \ln(v\mathbf{s} + \vec{v} \cdot \vec{s})\right] \exp(-i\epsilon_j t) \quad (1)$$

and

$$\begin{aligned} \chi_f^+ &= \varphi_f(\vec{x}) N^*(Z_T^*/k) {}_1F_1(-iZ_T^*/k, 1; -ikx - i\vec{k} \cdot \vec{x}) \\ &\times N^*(Z_P/p) {}_1F_1(-iZ_P/p, 1; -ips - i\vec{p} \cdot \vec{s}) \\ &\times \exp\left(-i\frac{k^2}{2}t\right). \end{aligned} \quad (2)$$

In these equations,  $\varphi_i$  and  $\varphi_f$  are the initial orbital and final plane-wave functions. The vectors  $\vec{x}$  and  $\vec{s}$  are the position of the electron with respect to the target nucleus and projectile respectively, and  $\epsilon_j$  is the initial orbital energy of the  $j$ -molecular orbital. Also,  $\vec{v}$  is the collision velocity,  $\vec{k}$  and  $\vec{p} = \vec{k} - \vec{v}$  are the momentum of the electron with respect to the target and projectile respectively, with  $Z_P$  being the

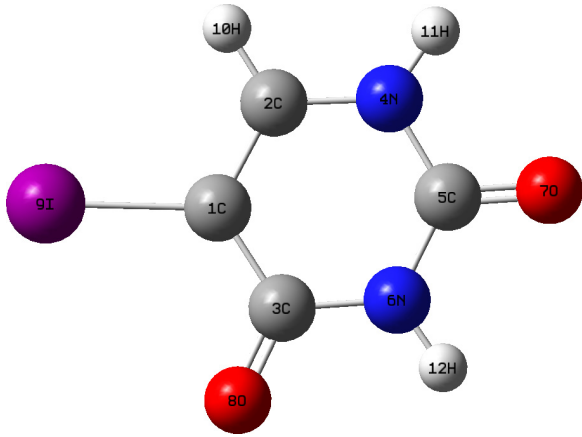


FIG. 1. A geometrical representation of the ground-state equilibrium structure of the 5-iodouracil.

projectile nuclear charge and  $Z_T^*$  being an effective target nuclear charge to describe the interaction of the active electron with the residual target with an effective Coulomb potential.  $N(a) = \exp(\pi a/2)\Gamma(1 - ia)$  with  $Z_T^*/k$  and  $Z_p/p$  are normalization factors, with  $\Gamma$  representing the Gamma function.

In order to describe  $\varphi_i$ , each molecular orbital was expressed as a linear combination of the atomic orbitals (LCAO). A geometrical representation of the ground-state equilibrium structure of the 5-iodouracil molecule is given in Fig. 1. The atoms are labeled with a number that allows us to identify which of them correspond to each one of the different molecular orbitals. *Ab initio* calculations were performed in the gas phase using the restricted Hartree-Fock (RHF) method implemented in the GAUSSIAN 09 software [50]. The C, O, H, and N atoms were represented using Pople's split-valence triple-zeta basis set 6-311G, while iodine was described using a Douglas-Kroll-Hess (DKH) contracted Gaussian basis set of triple zeta valence quality plus polarization functions (TZP), including explicitly all electrons and scalar relativistic effects [51]. The resulting ionization energy is 9.69 eV, which is very close to the 9.93-eV experimental value.

No symmetry constraints were applied in the relaxation calculation; the resulting equilibrium structure of the iodouracil molecule adopts the Cs point group symmetry (mirror plane). A population analysis of all occupied orbitals was carried out using the self-consistent field (SCF) density, with the minimum contribution percentage to include in individual orbital population analysis set to 1%. For each  $j$ -molecular orbital, the effective number of  $\xi_{j,i}$  electrons, relative to the atomic component  $i$ , was obtained from a standard Mulliken population analysis. Then, taken into account that experimentally the orientation of the molecular target is not distinguished, an average over all initial positions appears as necessary. In order to simulate this average, all atomic compounds of the molecular orbitals are considered centered on a unique center, but preserving the corresponding population analysis described above. Thus, the calculation for the different target orientations is avoided. This approximation has been previously employed with success to describe the existing experimental spectra for ionization and electron capture in ion impact on DNA nucleobases and Uracil (see, for example,

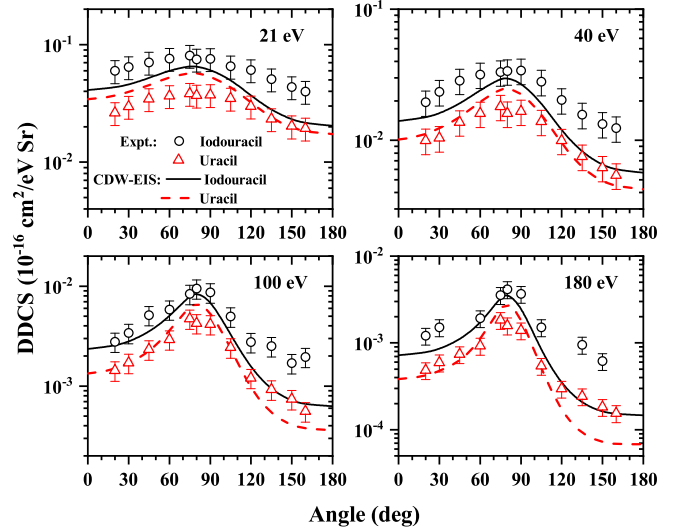


FIG. 2. Angular dependence of DDCS of electron emission from 5-iodouracil and uracil induced by 5.5-MeV/u  $C^{6+}$  ions.

Refs. [52,53]). The final continuum wave function associated with each one of the atomic components of the different molecular orbitals is described using an effective target charge  $Z_T^* = Z_{ji} = (-2n_{ji}^2\varepsilon_j)^{1/2}$ , where  $n_{ji}$  is the principal quantum number corresponding to the quantum state of the considered atom.

Proceeding in the same way as Galassi *et al.* [53], we obtained double differential cross sections  $d^2\sigma_j/d\Omega d\epsilon$  corresponding to each molecular orbital, as a function of the energy  $\epsilon$  and the solid angle  $\Omega$  subtended by the ejected electron, using the expression

$$\frac{d^2\sigma_j}{d\Omega d\epsilon} = \sum_{i=1}^{N_j} \xi_{ji} \frac{d^2\sigma_{ji}}{d\Omega d\epsilon}, \quad (3)$$

where  $\xi_{ji}$  corresponds to the population of the  $i$  atomic component of the  $j$  molecular orbital and  $d^2\sigma_{ji}/d\Omega d\epsilon$  represents the double differential cross section for ionization of this atom.  $N_j$  is the total number of the atomic components of each  $j$  molecular orbital. Then, the double differential cross section of the complete molecule can be calculated summing over all molecular orbital contributions,

$$\frac{d^2\sigma}{d\Omega d\epsilon} = \sum_{j=1}^N \frac{d^2\sigma_j}{d\Omega d\epsilon}. \quad (4)$$

In this equation,  $N$  is the total number of molecular orbitals. Population and binding energies of the uracil molecular orbitals as well as a representation of their equilibrium geometries were given in Galassi *et al.* [53].

#### IV. RESULTS AND DISCUSSION

The angular dependence of the observed DDCS are plotted and compared with the values calculated from the CDW-EIS model at four selected energies (i.e., 21, 40, 100, and 180 eV) in Fig. 2. The observed data show broad peaks around  $80^\circ$  at all the energies and such a peaking behavior is well explained

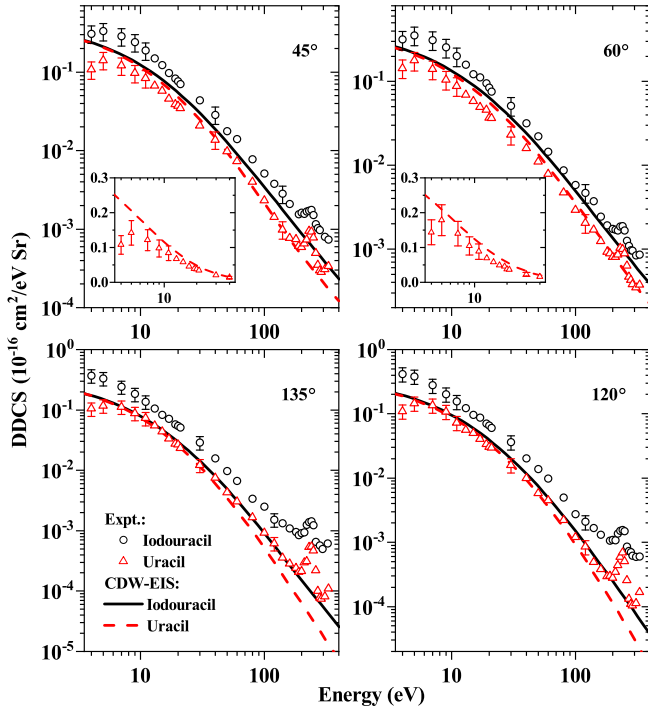


FIG. 3. Energy dependence of DDCS of electron emission from 5-iodouracil and uracil induced by 5.5-MeV/u  $C^{6+}$  ions. The DDCS below 40 eV for uracil at forward angles are shown in insets.

in terms of binary-collision mechanism in ion-atom collisions. Accordingly, the behavior is consistent with the CDW-EIS model as shown in Fig. 2.

Ejected energy dependence of the e-DDCS for the iodouracil and uracil at four different emission angles are shown in Fig. 3. The DDCS spectra starting from a few eV to 330 eV are displayed. The carbon KLL Auger electron peak is observed at  $\approx 240$  eV. The DDCS spectra show a rapid decrease, i.e., by  $\approx 3$  orders of magnitudes, with the increasing electron energy (cf. Fig. 3) indicating the dominant contribution of the low-energy electrons. For iodouracil the experiment-theory agreement is not so good, but for uracil the agreement is reasonably good. In particular, the model (dashed lines) explains the uracil data quite well for backward angles over the whole energy range. For the forward angles, the theory agrees with the data quite well above 30 eV. Even at lower energies, the calculations fall slightly higher than the data but remain within experimental uncertainties. To explain this, we have used two insets (for the forward angles) in which the low-energy data (up to 40 eV) are plotted for uracil. The larger disagreement with the iodouracil data, particularly at lower energies in the case of forward angles, is interesting since this energy range is quite important for the hadron therapy. This different could be related to the atomic GDR which is not included in the model calculation (see below). The angular dependence of the iodouracil-to-uracil DDCS ratio is plotted in Fig. 4(a). The CDW-EIS model underestimates the DDCS ratio values at all four energies. The observed energy dependence of iodouracil-to-uracil DDCS ratios are plotted in Fig. 4(b) for fixed emission angles. The enhancement of e-DDCS is found to be almost independent

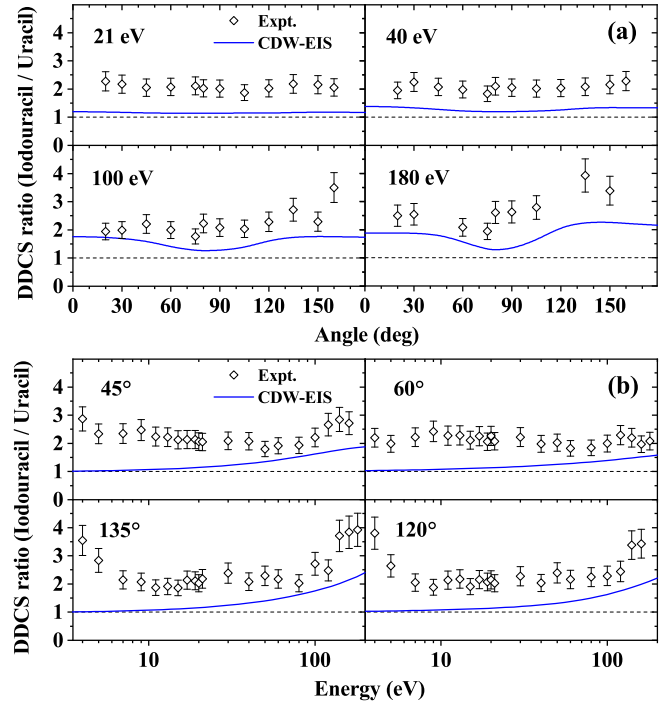


FIG. 4. (a) Angle and (b) energy dependence of the DDCS ratio of iodouracil to uracil. The dashed lines represent the ratio value of one.

of e-emission angle. The average ratios at the forward and backward angles are about 2.3. This implies that the introduction of the I atom in the uracil molecule enhances the e-emission from iodouracil substantially, giving rise to sensitizing factor  $F_S^{el} \approx 2.3$ . However, according to the CDW-EIS model which includes all the orbitals (29 for uracil and 55 for iodouracil), the calculated (Fig. 5) ratio is less than 1.05 for around 3 eV. Then it increases to about 1.05–1.10 for 10 eV, 1.10–1.15 for 15 eV, and 1.15–1.23 for 25 eV. For 30 eV energy, this ratio is between 1.17 to 1.30. An average enhancement of  $f_{ionz} \approx 1.15$  is estimated for the energy range of 1 to 30 eV, which is relevant for the present purpose. Therefore, experimentally measured  $F_S^{el} \approx 2.3$  cannot be explained in terms of the CDW-EIS based on independent electron approximation. The Auger cascade can contribute only little, i.e.,  $\approx 12\%$ , considering only the  $N_{4,4}OO$  Auger lines [54], giving the Auger factor  $f_A \approx 1.12$

The atomic GDR of the  $4d$  electrons decays by the emission of the low-energy electrons, causing an enhancement

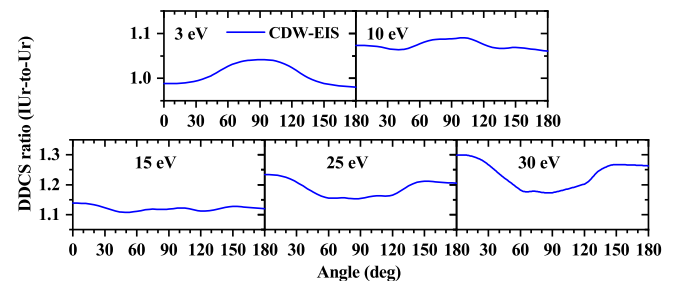


FIG. 5. Angle dependence of the theoretical DDCS ratio of iodouracil to uracil in low emission energies.

as predicted in Refs. [2,27]. The GDR induced enhancement  $f_{GDR}$  is thereby derived from the total enhancement as,  $2.3/(f_{ionz} \cdot f_A)$ , i.e.,  $f_{GDR} \approx 1.8$ . This is also close to the observed enhancement due to collective plasmon excitation in  $C_{60}$  fullerene for which the enhancement factor was about 1.5 [24,55,56]. In the present study, any structure in the electron DDCS spectrum due to the deexcitation of the GDR (with energy  $E_{GDR}$ ) is not visible. Such electron peak should appear at an energy lower than  $E_{GDR}$  since some energy must be spent to ionize these bound electrons. The width of the GDR peak (i.e., about 40 eV) is too large for the resonance to be observable on top of the steep energy dependence of the DDCS.

The measured TCS for iodouracil and uracil are  $8.51 \times 10^{-15}$  and  $4.44 \times 10^{-15}$  cm<sup>2</sup>, respectively. To understand the radio-sensitizing effect one important aspect is to compare the DDCS or TCS with that for the water molecule, since water constitutes about 60% of the human body. The TCS for e-emission from iodouracil is found to be  $\approx 15$  times larger than that for a water molecule having a TCS,  $\approx 5.6 \times 10^{-16}$  cm<sup>2</sup> [57]. If one normalizes the TCS for the equal volume of water and iodouracil, then the sensitizing factor ( $F_S^{el}$ ) becomes  $15/6 = 2.5$  since the volume of iodouracil is six times larger than that of the water molecule. However, the theoretical (CDW-EIS) prediction [14], based on Coulomb ionization alone, for the iodouracil-to-water molecule ratio [ $f_{ionz}$ ] is only 6.2 [=  $5.47 \times 10^{-15}$  cm<sup>2</sup>/ $8.8 \times 10^{-16}$  cm<sup>2</sup>] and  $\approx 1.0$  based on the volume-normalization. Assuming the rest of the e-emission process is mostly governed by the GDR in I atom (apart from Auger cascade) one again obtains the GDR contribution as  $f_{GDR} = 15/(6.2f_A)$ , i.e., about  $2.20 \pm 0.44$  (which is independent of single molecule since molecules of same volume are considered). This value is in excellent agreement with that derived above, i.e.,  $1.80 \pm 0.36$  from the iodouracil-to-uracil ratio. Since they are very close to each other one may use an average value of  $f_{GDR} \approx 2.0$ . It may also be noted that the sensitizing factor  $F_S^{sb}$ , measured from the DNA strand-breaking statistics, for an isolated Pt atom embedded in a plasmid DNA was found to be quite close, i.e.,  $\approx 1.6$  [21] and that for an inserted Au NP of bigger size was  $\approx 2.0$  [22], again in excellent agreement with the measured  $F_S^{el}$  of  $2.3 \pm 0.5$  between an iodouracil and uracil and 2.5 between iodouracil and water. We may therefore conclude that  $F_S^{sb} \sim F_S^{el}$ .

To get insight into the derived value of  $f_{GDR}$  ( $\approx 2.0$ ) involving iodine, we may refer to the predicted values [2] for the Ag atom. In both the atoms, all 10 electrons in the  $4d$ -subshell contribute to the atomic GDR. However, in real application with nanoparticle (NP) inserted in a DNA a large number of atoms are involved. For example, in the case of the Ag NP of diameter 1 nm the predicted enhancement (over water of same volume) was about 15 to 30 times in the e-energy range of 0 to 25 eV due to the atomic GDR excited by protons of velocity ( $v$ ) 6.35 a.u. This implies an enhancement of a factor of  $\approx 1.0$  to 2.0 (over 0 to 25 eV) per Ag atom since the

number of contributing Ag atoms were about 1/3 of the total of 40 atoms [58] in the NP based on the impact parameter ( $b$ ) consideration [2]. This enhancement was re-estimated for the present collision velocity using the scaling approach. At  $v \approx 15$  a.u., the range of  $b$  and therefore the fraction of Ag atoms contributing to the GDR increases to about 85–90%. The reduction in the GDR cross section was also accounted for by using Eqs. (18) and (19) in Ref. [27]. Finally, the reduction in the TCS of water was also considered using the  $v^{-1.7}$  scaling rule [57]. Thus, the enhancement per Ag atom over water would be a factor of  $\approx 3.0$  [2,27,58] at 25 eV. Therefore, over the e-energy 0 to 25 eV, this factor will be 1.5 to 3.0, giving an average value of  $f_{GDR}^{Ag} \approx 2.25$ . This value is in excellent agreement to that derived  $f_{GDR}^I \approx 2.0 \pm 0.4$  for the I atom and thereby confirming the theoretical prediction on the GDR contribution to the sensitizing effect.

## V. CONCLUSIONS

In conclusion, the DDCS and TCS of e-emission from iodouracil and uracil upon the bombardment of 5.5-MeV/u bare C ions have been measured. The measured radio-sensitizing or electron enhancement factors of 2.3 and 2.5 over uracil and water, respectively, are in excellent agreement with the radio-sensitizing factors measured in the case of Pt or Au NP embedded in a DNA from the strand-breaking studies. The enhancement is substantially large compared to the prediction of the state-of-the-art CDW-EIS model but the atomic GDR of the strongly correlated  $4d$  electrons in the I atom is shown to play a crucial role. The GDR contribution provides an enhancement of a factor of  $2.0 \pm 0.4$ , which is in excellent agreement with the theoretical prediction based on the GDR in an atom with filled  $4d$  subshell (such as Ag). This provides conclusive experimental evidence of the crucial role of the collective excitation in radio sensitization. It is evident that introduction of a single halogen atom, I, in the biomolecule, can indeed cause a substantial nanosensitizing effect. Therefore, the halouracil molecules, in particular, iodouracil, may have potential as a prototypical system for the radio sensitizer, provided it satisfies other practical considerations.

## ACKNOWLEDGMENTS

The authors thank the staff of the BARC-TIFR Pelletron accelerator facility and A. Verkhovtsev and A. Solovyov for communications about their published work. Sandia National Laboratories is a multimission laboratory managed and operated by National Technology and Engineering Solutions of Sandia, LLC, a wholly owned subsidiary of Honeywell International, Inc., for the US Department of Energy's National Nuclear Security Administration under Contract No. DE-NA0003525. The views expressed in the article do not necessarily represent the views of the US DOE or the US Government.

[1] E. Porcel, S. Liehn, H. Remita, N. Usami, K. Kobayashi, Y. Furusawa, C. L. Sech, and S. Lacombe, *Nanotechnology* **21**, 085103 (2010).

[2] A. V. Verkhovtsev, A. V. Korol, and A. V. Solov'yov, *Phys. Rev. Lett.* **114**, 063401 (2015).

- [3] P. Håkansson, E. Jayasinghe, A. Johansson, I. Kamensky, and B. Sundqvist, *Phys. Rev. Lett.* **47**, 1227 (1981).
- [4] B. Coupier, B. Farizon, M. Farizon, M. J. Gaillard, F. Gobet, N. V. de Castro Faria, G. Jalbert, S. Ouaskit, M. Carré, B. Gstir, G. Hanel, S. Denifl, L. Feketeova, P. Scheier, and T. D. Märk, *Eur. Phys. J. D* **20**, 459 (2002).
- [5] J. Tabet, S. Eden, S. Feil, H. Abdoul-Carime, B. Farizon, M. Farizon, S. Ouaskit, and T. Märk, *Int. J. Mass Spectrometry* **292**, 53 (2010).
- [6] Y. Iriki, Y. Kikuchi, M. Imai, and A. Itoh, *Phys. Rev. A* **84**, 052719 (2011).
- [7] A. N. Agnihotri, S. Kasthurirangan, S. Nandi, A. Kumar, M. E. Galassi, R. D. Rivarola, O. Fojón, C. Champion, J. Hanssen, H. Lekadir, P. F. Weck, and L. C. Tribedi, *Phys. Rev. A* **85**, 032711 (2012).
- [8] A. N. Agnihotri, S. Kasthurirangan, S. Nandi, A. Kumar, C. Champion, H. Lekadir, J. Hanssen, P. F. Weck, M. E. Galassi, R. D. Rivarola, O. Fojón, and L. C. Tribedi, *J. Phys. B: At., Mol. Opt. Phys.* **46**, 185201 (2013).
- [9] L. C. Tribedi, A. N. Agnihotri, M. E. Galassi, R. D. Rivarola, and C. Champion, *Eur. Phys. J. D* **66**, 303 (2012).
- [10] M. A. Bolorizadeh and M. E. Rudd, *Phys. Rev. A* **33**, 888 (1986).
- [11] M. E. Rudd, T. V. Goffe, R. D. DuBois, and L. H. Toburen, *Phys. Rev. A* **31**, 492 (1985).
- [12] L. H. Toburen, W. E. Wilson, and R. J. Popowich, *Radiat. Res.* **82**, 27 (1980).
- [13] C. Dal Cappello, C. Champion, O. Boudrioua, H. Lekadir, Y. Sato, and D. Ohsawa, *Nucl. Instr. Meth. Phys. Res. B* **267**, 781 (2009).
- [14] S. Bhattacharjee, S. Biswas, J. M. Monti, R. D. Rivarola, and L. C. Tribedi, *Phys. Rev. A* **96**, 052707 (2017).
- [15] S. Bhattacharjee, S. Biswas, C. Bagdia, M. Roychowdhury, S. Nandi, D. Misra, J. M. Monti, C. A. Tachino, R. D. Rivarola, C. Champion, and L. C. Tribedi, *J. Phys. B At. Mol. Opt. Phys.* **49**, 065202 (2016).
- [16] G. F. Knoll, *Radiation Detection and Measurement*, 3rd ed. (Wiley, New York, 2000), Chap. 2, p. 32.
- [17] B. Boudaïffa, P. Cloutier, D. Hunting, M. A. Huels, and L. Sanche, *Science* **287**, 1658 (2000).
- [18] S. Gohlke, A. Rosa, E. Illenberger, F. Brüning, and M. A. Huels, *J. Chem. Phys.* **116**, 10164 (2002).
- [19] H. Abdoul-Carime, S. Gohlke, and E. Illenberger, *Phys. Rev. Lett.* **92**, 168103 (2004).
- [20] C. König, J. Kopyra, I. Bald, and E. Illenberger, *Phys. Rev. Lett.* **97**, 018105 (2006).
- [21] E. Porcel, O. Tillement, F. Lux, P. Mowat, N. Usami, K. Kobayashi, Y. Furusawa, C. L. Sech, S. Li, and S. Lacombe, *Nanomedicine: Nanotechnol., Biol. Med.* **10**, 1601 (2014).
- [22] K. T. Butterworth, J. A. Wyer, M. Brennan-Fournet, C. J. Latimer, M. B. Shah, F. J. Currell, and D. G. Hirst, *Radiat. Res.* **170**, 381 (2008).
- [23] F. Xiao, Y. Zheng, P. Cloutier, Y. He, D. Hunting, and L. Sanche, *Nanotechnology* **22**, 465101 (2011).
- [24] A. H. Kelkar, L. Gulyás, and L. C. Tribedi, *Phys. Rev. A* **92**, 052708 (2015).
- [25] A.H. Kelkar, D. Misra, L. Gulyas, and L.C. Tribedi, *Eur. Phys. J. D* **74**, 157 (2020).
- [26] A. V. Verkhovtsev, A. V. Korol, A. V. Solov'yov, P. Bolognesi, A. Ruocco, and L. Avaldi, *J. Phys. B: At. Mol. Opt. Phys.* **45**, 141002 (2012).
- [27] A. V. Verkhovtsev, A. V. Korol, and A. V. Solov'yov, *J. Phys. Chem. C* **119**, 11000 (2015).
- [28] H. Abdoul-Carime, M. A. Huels, F. Brüning, E. Illenberger, and L. Sanche, *J. Chem. Phys.* **113**, 2517 (2000).
- [29] M.-A. Herve du Penhoat, M. A. Huels, P. Cloutier, J.-P. Jay-Gerin, and L. Sanche, *Phys. Chem. Chem. Phys.* **5**, 3270 (2003).
- [30] H. Abdoul-Carime, M. A. Huels, E. Illenberger, and L. Sanche, *Int. J. Mass Spectr.* **228**, 703 (2003).
- [31] D. V. Klyachko, M. A. Huels, and L. Sanche, *Rad. Res.* **151**, 177 (1999).
- [32] J.-P. Champeaux, P. Carcabal, J. Rabier, P. Cafarelli, M. Sence, and P. Moretto-Capelle, *Phys. Chem. Chem. Phys.* **12**, 5454 (2010).
- [33] A. Itoh, Y. Iriki, M. Imai, C. Champion, and R. D. Rivarola, *Phys. Rev. A* **88**, 052711 (2013).
- [34] A. N. Agnihotri, S. Nandi, S. Kasthurirangan, A. Kumar, M. E. Galassi, R. D. Rivarola, C. Champion, and L. C. Tribedi, *Phys. Rev. A* **87**, 032716 (2013).
- [35] G. Wendin, *J. Phys. B* **6**, 42 (1973).
- [36] D. W. Lindle, P. H. Kobra, C. M. Truesdale, T. A. Ferrett, P. A. Heimann, H. G. Kerkhoff, U. Becker, and D. A. Shirley, *Phys. Rev. A* **30**, 239 (1984).
- [37] A. P. Hitchcock and C. E. Brion, *J. Elec. Spectr. Rel. Phenomena* **13**, 193 (1978).
- [38] F. J. Comes, U. Nielsen, and W. H. E. Schwarz, *J. Chem. Phys.* **58**, 2230 (1973).
- [39] L. Nahon, A. Svensson, and P. Morin, *Phys. Rev. A* **43**, 2328 (1991).
- [40] D. L. Ederer, *Phys. Rev. Lett.* **13**, 760 (1964).
- [41] U. Becker, T. Prescher, E. Schmidt, B. Sonntag, and H. E. Wetzel, *Phys. Rev. A* **33**, 3891 (1986).
- [42] B. Kammerling, H. Kossman, and V. Schmidt, *J. Phys. B At. Mol. Opt. Phys.* **22**, 841 (1989).
- [43] J.-P. Connerade, J.-M. Esteve, and R. Karnatak, editors, *Giant Resonances in Atoms, Molecules, and Solids* (Springer, New York, 1987).
- [44] P. D. Fainstein, L. Gulyás, F. Martín, and A. Salin, *Phys. Rev. A* **53**, 3243 (1996).
- [45] S. Bhattacharjee, C. Bagdia, M. R. Chowdhury, A. Mandal, J. M. Monti, R. D. Rivarola, and L. C. Tribedi, *Phys. Rev. A* **100**, 012703 (2019).
- [46] M. Karni, D. Zidon, P. Polak, Z. Zalevsky, and O. Shefi, *DNA and Cell Biology* **32**, 298 (2013).
- [47] D. Misra, K. V. Thulasiram, W. Fernandes, A. H. Kelkar, U. Kadhane, A. Kumar, Y. Singh, L. Gulyás, and L. C. Tribedi, *Nucl. Instr. Meth. Phys. Res. B* **267**, 157 (2009).
- [48] P. D. Fainstein, V. H. Ponce, and R. D. Rivarola, *J. Phys. B At. Mol. Opt. Phys.* **21**, 287 (1988).
- [49] S. E. Corchs, R. D. Rivarola, and J. H. McGuire, *Phys. Rev. A* **47**, 3937 (1993).
- [50] M. J. Frisch, G. W. Trucks, H. B. Schlegel, G. E. Scuseria, M. A. Robb, J. R. Cheeseman, G. Scalmani, V. Barone, B. Mennucci, G. A. Petersson, H. Nakatsuji, M. Caricato, X. Li, H. P. Hratchian, A. F. Izmaylov, J. Bloino, G. Zheng, J. L.

- Sonnenberg, M. Hada, M. Ehara, K. Toyota, R. Fukuda, J. Hasegawa, M. Ishida, T. Nakajima, Y. Honda, O. Kitao, H. Nakai, T. Vreven, J. A. Montgomery Jr., J. E. Peralta, F. Ogliaro, M. Bearpark, J. J. Heyd, E. Brothers, K. N. Kudin, V. N. Staroverov, R. Kobayashi, J. Normand, K. Raghavachari, A. Rendell, J. C. Burant, S. S. Iyengar, J. Tomasi, M. Cossi, N. Rega, J. M. Millam, M. Klene, J. E. Knox, J. B. Cross, V. Bakken, C. Adamo, J. Jaramillo, R. Gomperts, R. E. Stratmann, O. Yazyev, A. J. Austin, R. Cammi, C. Pomelli, J. W. Ochterski, R. L. Martin, K. Morokuma, V. G. Zakrzewski, G. A. Voth, P. Salvador, J. J. Dannenberg, S. Dapprich, A. D. Daniels, À. Farkas, J. B. Foresman, J. V. Ortiz, J. Cioslowski, and D. J. Fox, *Gaussian 09 rev. A.02* (Gaussian, Wallingford, CT, 2009).
- [51] F. E. Jorge, A. Canal Neto, G. G. Camiletti, and S. F. Machado, *J. Chem. Phys.* **130**, 064108 (2009).
- [52] C. Champion, P. F. Weck, H. Lekadir, M. E. Galassi, O. A. Fojón, P. Abufager, R. D. Rivarola, and J. Hanssen, *Phys. Med. Biol.* **57**, 3039 (2012).
- [53] M. E. Galassi, C. Champion, P. F. Weck, R. D. Rivarola, O. Fojón, and J. Hanssen, *Phys. Med. Biol.* **57**, 2081 (2012).
- [54] L. O. Werme, T. Bergmark, and K. Siegbahn, *Phys. Scr.* **6**, 141 (1972).
- [55] S. Cheng, H. G. Berry, R. W. Dunford, H. Esbensen, D. S. Gemmell, E. P. Kanter, T. LeBrun, and W. Bauer, *Phys. Rev. A* **54**, 3182 (1996).
- [56] H. Tsuchida, A. Itoh, K. Miyabe, Y. Bitoh, and N. Imanishi, *J. Phys. B At. Mol. Opt. Phys.* **32**, 5289 (1999).
- [57] S. Bhattacharjee, C. Bagdia, M. R. Chowdhury, J. M. Monti, R. D. Rivarola, and L. C. Tribedi, *Eur. Phys. J. D* **72**, 15 (2018).
- [58] A. V. Verkhovtsev and A. V. Solov'yov (private communication).

# Coherent electron emission from O<sub>2</sub> in collisions with fast electrons

Madhusree Roy Chowdhury<sup>1</sup>, Carlos R. Stia<sup>2</sup>, Carmen A. Tachino<sup>2</sup>, Omar A. Fojón<sup>2</sup>, Roberto D. Rivarola<sup>2</sup>, and Lokesh C. Tribedi<sup>1,a</sup>

<sup>1</sup> Tata Institute of Fundamental Research, Homi Bhabha Road, 400005 Mumbai, India

<sup>2</sup> Instituto de Física Rosario (CONICET-UNR), 2000 Rosario, Argentina

Received 6 December 2016 / Received in final form 21 February 2017

Published online 29 August 2017 – © EDP Sciences, Società Italiana di Fisica, Springer-Verlag 2017

**Abstract.** Absolute double differential cross sections (DDCS) of secondary electrons emitted in ionization of O<sub>2</sub> by fast electrons have been measured for different emission angles. Theoretical calculations of atomic DDCS were obtained using the first Born approximation with an asymptotic charge of  $Z_T = 1$ . The measured molecular DDCS were divided by twice the theoretical atomic DDCS to detect the presence of interference effects which was the aim of the experiment. The experimental to theoretical DDCS ratios showed clear signature of first order interference oscillation for all emission angles. The ratios were fitted by a first order Cohen-Fano type model. The variation of the oscillation amplitudes as a function of the electron emission angle showed a parabolic behaviour which goes through a minimum at 90°. The single differential and total ionization cross sections have also been deduced, besides the KLL Auger cross sections. In order to make a comparative study, we have discussed these results along with our recent experimental data obtained for N<sub>2</sub> molecule.

## 1 Introduction

Cross section measurements of electron impact ionization of different atoms and molecules have been a subject of study over decades. Several theoretical and experimental works have been executed to measure the total ionization cross section (TCS) or single differential cross section (SDCS) for different target species. The cross sections, differential over electron emission energy and angle, provide more detailed picture of the collision mechanisms. The DDCS measurements of O<sub>2</sub> and N<sub>2</sub> induced by intermediate energy electrons have been performed previously [1].

Apart from differential cross section measurements, another interesting feature of diatomic molecules is its resemblance with Young's double slit for electron waves where the two nuclei act as the two slits, as predicted by Cohen and Fano in 1966 [2]. Electrons are emitted coherently from the two centers of the molecule giving rise to interference oscillations. Several works towards the interference effect have been carried out in case of the simplest diatomic molecule, H<sub>2</sub> in collisions with fast electrons, heavy ions or photons [3–6]. Extending the work further from H<sub>2</sub> to more complex diatomic molecules, such as N<sub>2</sub> and O<sub>2</sub>, oscillation has been observed in individual orbitals when impacted with photons [7]. The oscillations observed in individual orbitals were phase shifted from each other. For heavy ion impact, there lies some controversy about the evidence of oscillation both for

N<sub>2</sub> and O<sub>2</sub> [8–10]. However, for proton impact on N<sub>2</sub>, it has been theoretically shown that interference signatures appear in double differential cross sections (DDCS) for the two innermost molecular orbitals, being them in phase opposition [11]. Recently, the interference related experiments have also been performed for heteronuclear molecules [12,13].

In this work, we aim to investigate the presence of interference effect for the multi-electronic target O<sub>2</sub> upon impact with fast electrons of energy 7 keV. Recently interference oscillation have been observed in triple [14] and double [15] differential cross section measurements of N<sub>2</sub> by intermediate and high energy electrons respectively. To our knowledge, no such observation has been reported for electron impact ionization of O<sub>2</sub> (except a very recent work, indicated below). In case of fast electron beam as projectile, the Coulomb perturbation strength is quite small compared to fast heavy ions (e.g. C or O ions) of similar velocity for which simultaneous multiple ionization of different orbitals are quite strong. In this respect the electrons can be considered as a “gentle” projectile resulting in negligible multiple ionization. In this work we will mainly talk about the interference oscillations observed for oxygen molecule from the DDCS ratios. Though detailed discussions about interference oscillations for N<sub>2</sub> have been reported in reference [15], to make a comparative study for the two molecules we have added some of our recent and detailed data of N<sub>2</sub> which are not shown in [15] along with the data for molecular oxygen. As explained below,

<sup>a</sup> e-mail: lokesh@tifr.res.in

the ratio of DDCS for  $O_2$ -to-2O (i.e. twice the atomic DDCS) was used to derive the interference oscillation.

In the absence of experimental atomic cross sections, the DDCS for atomic oxygen were obtained from a theoretical formalism, where the multielectronic system was reduced to a single effective electron problem. In a similar manner, the DDCS for atomic  $N$  were also obtained. Since the main goal of this work is to explore the interference oscillation through the study of DDCS ratios, we do not make any attempt to predict the molecular DDCS, as proper molecular calculations are at present in progress. Detailed discussion on the theoretical formalisms concerning the coherent electron emission from different target molecules are discussed in reference [16]. Further details of theoretical work in connection with the  $N_2$  ionization is given in our recent work [15]. Atomic units are used unless otherwise stated.

## 2 Experimental details

The projectile electrons of energy 7 keV was obtained from a commercially available electron gun. The beam was focussed and collimated using Einzel lens, electrostatic deflectors and several apertures of different diameters. Magnetic coils were also used for better alignment. A stable beam of about 900 nA current was used throughout the experiment with minor fluctuations in the presence and absence of gas.

The experiment was performed in high vacuum condition at a base pressure of  $5 \times 10^{-8}$  mbar. The chamber was flooded with the target gases ( $O_2$ ,  $N_2$ ) at an absolute pressure of 0.15 mTorr which was monitored with a capacitance manometer. The electrons ejected after collision with the projectile beam were energy analyzed with the help of a hemispherical analyzer and further detected by a channel electron multiplier (CEM). The entire spectrometer was kept on a motorized turntable. The front of the CEM was biased at positive potential of 100 V, since the detection efficiency of CEM remains fairly constant ( $\sim 85\%$ ) within an electron energy range of about 100–700 eV. The entrance and exit slits were biased with a pre-acceleration voltage of 6 V which enhanced the collection of the low energy electrons. The Earth's magnetic field was reduced to about 10 mG near the interaction region. The low magnetic field was achieved with two sets of  $\mu$ -metal sheets lined on the inner wall of the scattering chamber. The incident beam was collected on a Faraday Cup for beam normalization purpose. The Faraday Cup was sufficiently long in order to prohibit the back scattered electrons from reaching the interaction region. The projectile beam transmission was obtained by comparing the current from two positions of the analyzer, i.e. aligned along  $0^\circ$  and then by moving it away from the beam path. When the analyzer is placed in-line with the beam direction, the projectile beam had to pass through several (i.e. five) apertures on the spectrometer, apart from the ones used for beam collimation, before falling on the Faraday cup. In the present experiment, the beam transmission was  $\sim 85\%$ .

The secondary electrons were collected for different emission angles between  $15^\circ$  and  $145^\circ$ . At each angle, electrons emitted with energy from 1–600 eV and 1–550 eV were detected for  $O_2$  and  $N_2$  respectively. The energy resolution of the analyser was  $\sim 6\%$  where the contribution from acceptance angle is about 1%. The sources of uncertainties in the DDCS measurement were from the statistical fluctuation (2%–10%), gas pressure fluctuation (6%–7%), efficiency (10%), resolution (5%–10%) and solid-angle-path-length integral (10%–12%). Overall error was estimated to be around 20%.

## 3 Theory

In the present study the interest is focused in the case of electrons as projectiles. A detailed analysis of the calculation of DDCS for electron emission from diatomic molecules by impact of protons and electrons was given in a recent review [16] and references therein.

As the possible existence of interference patterns is explored here from the ratio between experimental molecular DDCS and atomic DDCS corresponding to each one of the atomic compounds of the molecule, we pay particular attention to the determination of the latter ones.

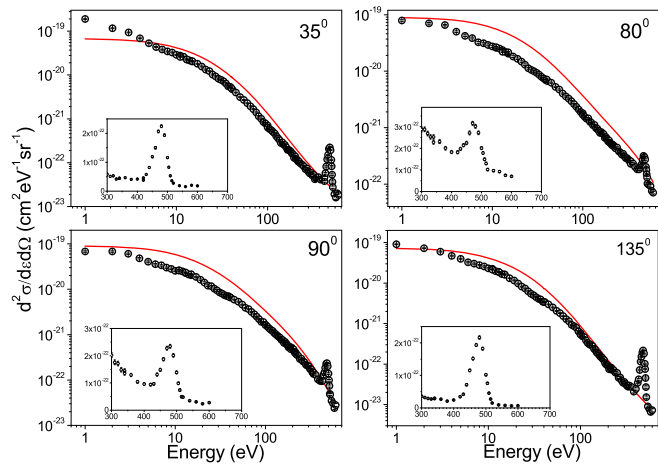
In order to calculate the atomic cross sections, within the framework of an independent electron model, it is assumed that only one target electron (the *active* one) is ionized in the final channel of the reaction, whereas the remaining *passive* electrons are considered as frozen in their initial orbitals during the reaction. In this context, DDCS were determined within a first-order Born approximation (B1), where the projectile dynamics is described through a plane-wave, in both the initial and final channels. In the entry channel, a Roothaan-Hartree-Fock representation of the different atomic orbitals was employed [17] and in the exit one, a Coulomb residual continuum function with an effective charge  $Z_T$  of unity was taken. This charge may be interpreted as the asymptotic one felt by the ionized electron due to its interaction with the residual target.

## 4 Results and discussions

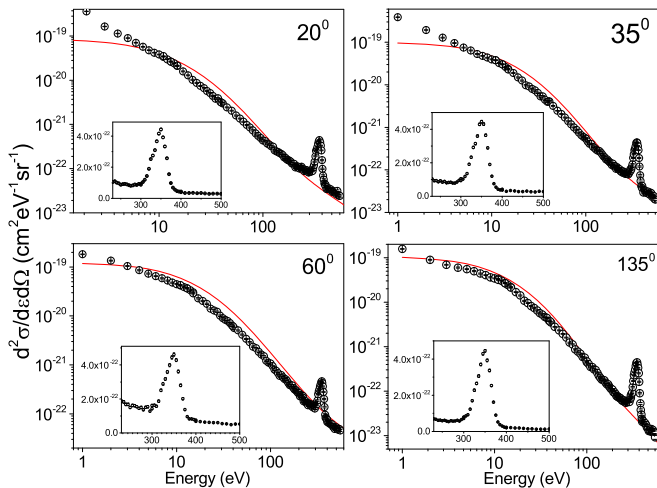
### 4.1 Energy distribution of DDCS spectrum

Figure 1 displays the energy distributions of the secondary electrons ejected from  $O_2$  molecules. The solid line corresponds to twice the atomic oxygen calculations. They are seen to be close to data points for the extreme forward and backward angles, whereas the difference is largest in case of angles near  $90^\circ$ . The sharp peak around 480 eV for all emission angles correspond to the K-LL Auger electron emission which is shown in the insets in Figure 1.

The energy distribution of the secondary electrons emitted in collision of 7 keV electrons with  $N_2$  target is shown in Figure 2 for different emission angles. Theoretical calculations for twice the atomic nitrogen are also shown. The K-LL Auger electrons for nitrogen are emitted around



**Fig. 1.** The measured absolute DDCS of O<sub>2</sub> for different emission angles. The red solid line corresponds to twice atomic O calculation using  $Z_T = 1$ . The Auger peak for each angle is shown separately in the insets.



**Fig. 2.** Absolute electron DDCS of N<sub>2</sub> at different forward and backward emission angles; Auger peaks are shown in the insets. The theoretical cross sections for twice atomic nitrogen (red solid line) are calculated using  $Z_T = 1$ .

355 eV, which is seen by the sharp peak in the DDCS spectrum (insets in Fig. 2). In case of extreme forward angles (20° and 35°), the cross section is seen to have a sharp rise for lowest emission energies ( $\leq 5$  eV) unlike that observed from the calculations. Although the origin of such unusual rise is not understood, but a systematic error due to un-subtracted slit-scattering background can not be ruled out completely.

#### 4.2 Angular distribution of DDCS spectrum

The angular distribution of the secondary electrons emitted from O<sub>2</sub> and N<sub>2</sub> are displayed in Figures 3 and 4 respectively. Tables 1 and 2 display some of the selected DDCS values, for a ready reference. The solid lines in

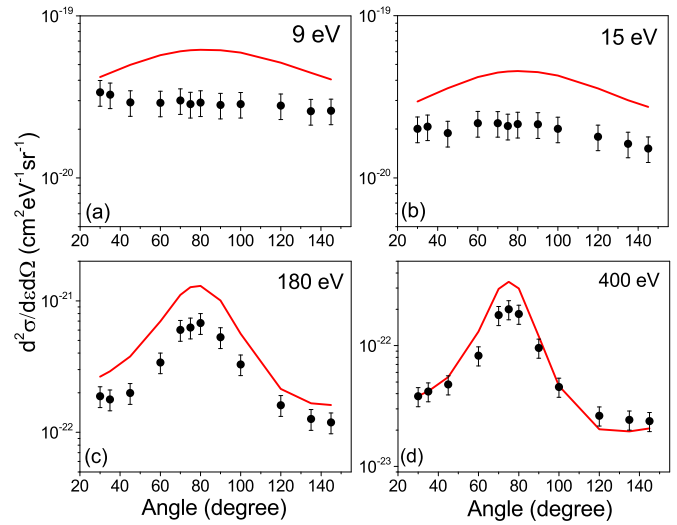


**Fig. 3.** DDCS at fixed electron emission energies for O<sub>2</sub>. The red solid line corresponds to the theoretical calculations for 2O.

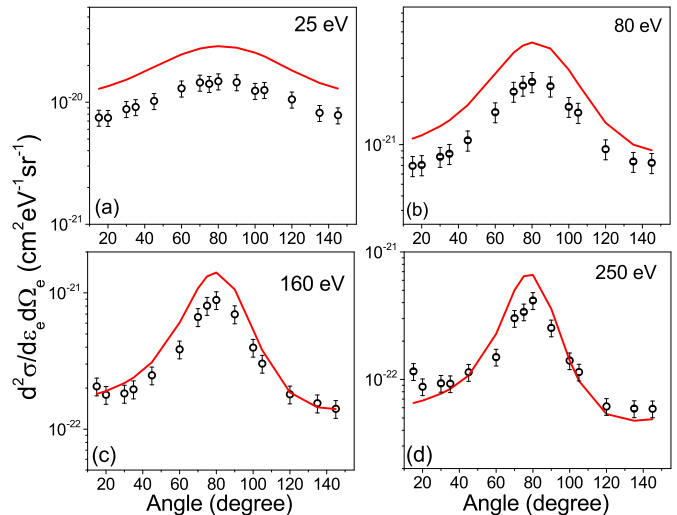


**Fig. 4.** DDCS for N<sub>2</sub> at fixed electron emission energies along with theoretical calculations for 2N (solid lines).

Figure 3 correspond to twice the theoretical calculations of atomic oxygen. The atomic cross sections are seen to be larger than the measured DDCS for molecular target with the discrepancy being largest for low emission energies. The distribution is seen to be almost flat for low emission energies which is governed by soft collision mechanisms. Here the electrons are emitted with large impact parameter. With increase in emission energy, a peaking is observed around 80° which is explained in terms of the binary nature of the collision. Similar distributions for N<sub>2</sub> are also observed (shown in Fig. 4). The red curves represent the theoretical calculations for 2N. Though overall qualitative matching is observed, theory underestimates the data for all cases. A minor signature of forward-backward asymmetry is observed for O<sub>2</sub> for higher emission energies.

**Table 1.** Measured DDCS for N<sub>2</sub> in units of Mb eV<sup>-1</sup> sr<sup>-1</sup> for different emission angles.

Energy (eV)	15°	20°	35°	45°	60°	70°	75°	80°	90°	100°	105°	120°	135°	145°
3	–	0.163	0.128	0.113	0.105	0.102	0.0983	0.092	0.0778	0.0568	0.0818	0.0644	0.0693	0.0724
5	–	0.089	0.075	0.0713	0.073	0.0725	0.0719	0.0684	0.0655	0.051	0.0647	0.0512	0.0554	0.0554
10	0.045	0.038	0.039	0.0394	0.0446	0.047	0.0458	0.0456	0.0444	0.0403	0.043	0.0346	0.0342	0.0334
21	0.0106	0.0102	0.0126	0.0135	0.0176	0.018	0.0184	0.0188	0.0186	0.0161	0.0169	0.013	0.0107	0.0105
41	3.1E-3	2.9E-3	4.1E-3	4.5E-3	5.6E-3	6.5E-3	7.1E-3	7.8E-3	7.6E-3	6.4E-3	6.7E-3	4.4E-3	3.5E-3	3.1E-3
60	1.4E-3	1.4E-3	1.7E-3	1.9E-3	2.9E-3	3.6E-3	4.2E-3	4.1E-3	3.9E-3	3.1E-3	2.9E-3	1.9E-3	1.6E-3	1.4E-3
100	4.6E-4	4.3E-4	5.5E-4	6.5E-4	1.1E-3	1.5E-3	1.7E-3	1.8E-3	1.7E-3	1.2E-3	1.02E-3	5.7E-4	4.5E-4	4.4E-4
140	2.8E-4	2.4E-4	2.8E-4	3.3E-4	5.2E-4	8.0E-4	1.1E-3	1.1E-3	9.4E-4	5.2E-4	4.3E-4	2.6E-4	2.01E-4	1.9E-4
180	1.7E-4	1.5E-4	1.5E-4	1.9E-4	3.1E-4	5.7E-4	7.4E-4	7.6E-4	5.6E-4	2.9E-4	2.4E-4	1.3E-4	1.2E-4	1.1E-4
220	1.3E-4	1.1E-4	1.1E-4	1.5E-4	2.3E-4	3.9E-4	5.2E-4	5.4E-4	4.0E-4	1.7E-4	1.6E-4	8.6E-5	7.3E-5	7.4E-5
250	1.1E-4	8.8E-5	9.3E-5	1.1E-4	1.5E-4	3.0E-4	3.4E-4	4.2E-4	2.5E-4	1.4E-4	1.1E-4	6.1E-5	5.9E-5	5.9E-5

**Table 2.** Measured DDCS for O<sub>2</sub> in units of Mb eV<sup>-1</sup> sr<sup>-1</sup> for different emission angles.

Energy (eV)	30°	35°	45°	60°	70°	75°	80°	90°	100°	120°	135°	145°
3	0.0993	0.0933	0.071	0.0672	0.0655	0.0632	0.0654	0.0606	0.0542	0.0675	0.0601	0.0646
5	0.0586	0.0533	0.0445	0.0421	0.0419	0.0415	0.0424	0.0405	0.0401	0.0408	0.0398	0.0383
10	0.0303	0.0288	0.0265	0.0279	0.0282	0.0284	0.0273	0.0256	0.0278	0.0257	0.0232	0.0238
21	0.0146	0.013	0.0137	0.0151	0.0152	0.0148	0.0147	0.014	0.0142	0.0114	9.7E-3	8.6E-3
41	4.4E-3	4.7E-3	4.9E-3	6.5E-3	6.9E-3	6.6E-3	6.6E-3	6.6E-3	5.4E-3	4.1E-3	3.4E-3	3.03E-3
60	2.2E-3	2.3E-3	2.7E-3	3.3E-3	4.1E-3	3.8E-3	4.0E-3	3.9E-3	3.4E-3	2.4E-3	1.8E-3	1.7E-3
100	6.4E-4	7.0E-4	8.6E-4	1.2E-3	1.5E-3	1.7E-3	1.8E-3	1.7E-3	1.3E-3	6.9E-4	5.8E-4	5.4E-4
140	2.8E-4	2.8E-4	3.7E-4	6.1E-4	9.5E-4	9.4E-4	9.7E-4	8.9E-4	5.8E-4	3.1E-4	2.4E-4	2.5E-4
180	1.8E-4	1.8E-4	1.9E-4	3.4E-4	6.0E-4	6.2E-4	6.8E-4	5.3E-4	3.3E-4	1.6E-4	1.3E-4	1.2E-4
220	1.1E-4	1.0E-4	1.3E-4	2.5E-4	4.1E-4	4.9E-4	4.8E-4	3.7E-4	2.0E-4	8.7E-5	7.2E-5	7.7E-5
260	7.3E-5	7.1E-5	8.8E-5	1.7E-4	3.4E-4	3.4E-4	3.6E-4	2.6E-4	1.2E-4	5.3E-5	4.6E-5	5.0E-5
300	6.2E-5	5.9E-5	6.9E-5	1.3E-4	2.8E-4	2.9E-4	2.9E-4	2.01E-4	7.8E-5	4.4E-5	3.6E-5	3.02E-5
340	4.9E-5	4.4E-5	4.8E-5	9.7E-5	2.3E-4	2.4E-4	2.5E-4	1.5E-4	5.5E-5	3.2E-5	2.8E-5	2.5E-5
400	3.8E-5	4.2E-5	4.8E-5	8.3E-5	1.8E-4	2.0E-4	1.8E-4	9.6E-5	4.5E-5	2.6E-5	2.4E-5	2.4E-5

In Figure 5 we have shown the angular distribution of the Auger electron peak for O<sub>2</sub> and N<sub>2</sub>. The KLL Auger electrons are emitted when K-shell ionization of the target atom takes place. As already seen from Figures 1 and 2, the peaks for O<sub>2</sub> and N<sub>2</sub> are seen around 480 eV and 355 eV, respectively, as expected. We have obtained the area under the Auger peak for each case. For an atom one may expect an isotropic angular distribution of the KLL Auger electron. In case of the O<sub>2</sub> molecule we do see such an isotropic behaviour (Fig. 5a). However, in the case of the N<sub>2</sub> molecules although the general behaviour is almost isotropic within about 15%, there is a oscillatory structure in the distribution (shown by the blue solid line in Fig. 5b, which is a guide to eye). The origin of such behaviour in the case of N<sub>2</sub> is not obvious. For the N and O atoms, the fluorescence yields are negligible. The total K-shell ionization cross sections, thus, derived from the K-LL Auger yield, are found to be 0.095 Mb for O<sub>2</sub> and 0.163 Mb for N<sub>2</sub>.

### 4.3 Experimental-to-theoretical DDCS ratio

From Figures 1 and 2, it is seen that the cross sections for both molecular and atomic targets fall by several orders of magnitude within the detected electron energy range. On

the other hand, the variation due to interference effects contributing from the molecule is rather small and hence cannot be observed readily from the DDCS spectrum.

In a previous work [15], DDCS for impact of electron beams on N<sub>2</sub> targets have been approximated by,

$$\sigma_{mol} = 2\sigma_{at}(k) \left[ 1 + \frac{\sin[kc(\theta)d]}{kc(\theta)d} \right] \quad (1)$$

where  $\sigma_{at}$  is the atomic cross section corresponding to each individual molecular compound, and  $\frac{\sin[kc(\theta)d]}{kc(\theta)d}$  is a Cohen-Fano type term originated from the coherent electron emission from the molecule. Here  $k$  is the electron momentum,  $d$  is the internuclear distance of the diatomic molecule, and  $c(\theta)$  is an adjustable frequency parameter. This expression has been employed just as an extension of the one obtained in collisions between ion beams and H<sub>2</sub> targets [2,5,18–20].

Therefore, to reveal the contribution due to interference effects, it is necessary to omit the variation of the cross section over the emission energy by dividing the molecular DDCS by twice the corresponding atomic cross section (see Eq. (1)). Due to the absence of measured data for the atomic target, the DDCS for O<sub>2</sub> are divided by the theoretical atomic calculations. In Figure 6, the DDCS ratios of O<sub>2</sub> to twice the theoretical cross sections of atomic

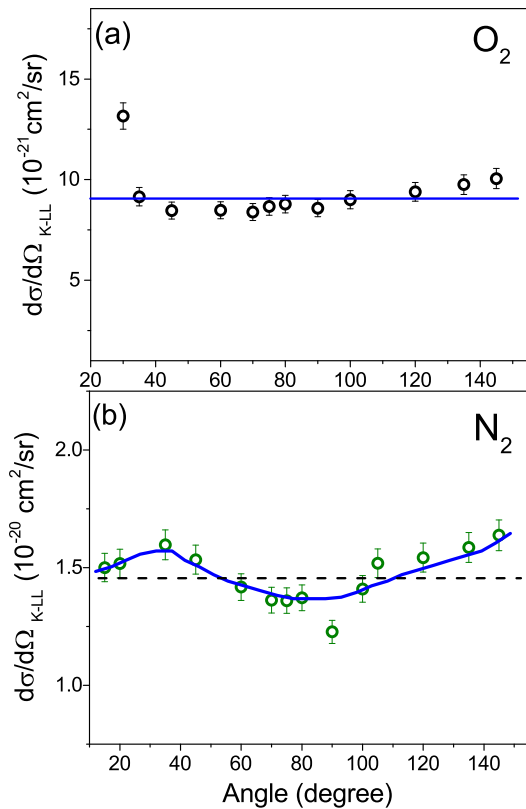


**Fig. 5.** Angular distribution of K-LL Auger electron emission for O<sub>2</sub> in (a) and N<sub>2</sub> in (b). Blue solid lines are a guide to eye.

oxygen are displayed for several forward and backward angles. The ratios reveal clear oscillatory structures for all the emission angles. In the case of 30° and 35°, half sinusoidal oscillatory structure is observed about a horizontal line. However, for other angles, full oscillation is observed. It may also be noticed that the oscillatory structure for the backward angles rides over a straight line of small positive slope. Also, a finer look into the ratio plots reveal that the oscillations are around 0.5–0.6, instead of the expected value of 1.0. These differences may be attributed to the fact, that the calculated atomic cross sections overestimate the data for all cases as can be readily seen from the energy distribution in Figure 1. To get a quantitative idea of the oscillatory structure with respect to electron velocity, the ratios have been fitted with the Cohen-Fano type model which is expressed as follows:

$$\frac{\sigma_{molecule}}{2\sigma_{atom}} = D + F(\theta) \frac{\sin[kc(\theta)d]}{kc(\theta)d}. \quad (2)$$

In this equation,  $F(\theta)$  is the amplitude of the oscillation,  $k$  is the electron momentum,  $d$  is the internuclear distance (2.28 a.u. for O<sub>2</sub>), and  $c(\theta)$  is the variable frequency parameter. For most of the backward angles, to account for the minor increasing trend in the oscillation, we have added a linear term in equation (2) along with the Cohen-Fano term. The slope was found to be almost same for these angles. The fitting is seen to match quite well for all the angles.

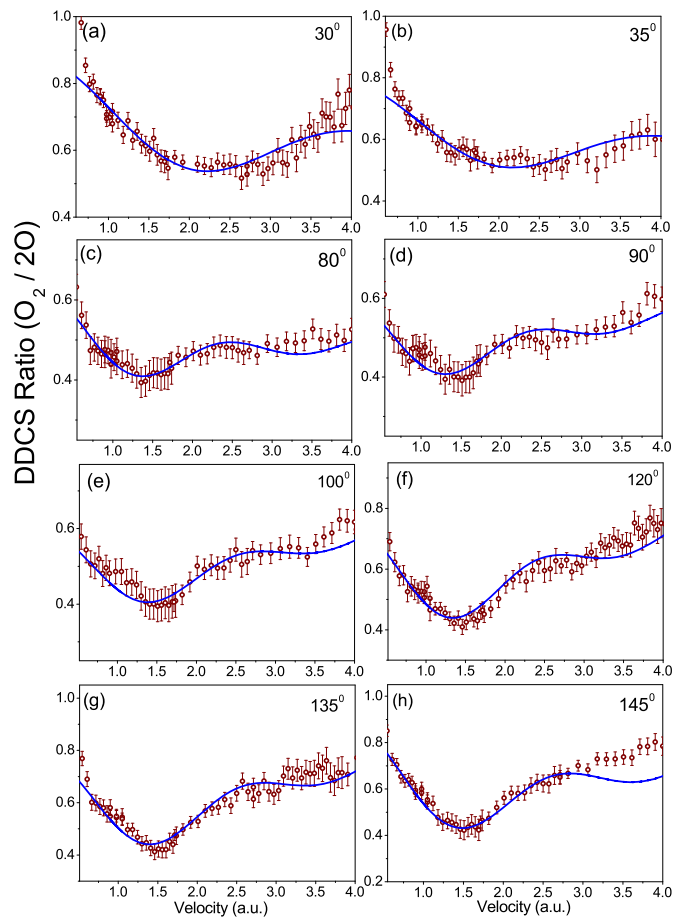


**Fig. 6.** Molecular to atomic cross section ratio ( $\sigma_{O_2}/2\sigma_O$ ). Solid line represents the Cohen-Fano fitting given by equation (2).

Similar DDCS ratios for nitrogen molecule are shown in Figure 7. In the case of N<sub>2</sub>, the data have been divided by the calculated cross sections of 2N. Half sinusoidal oscillations for all emission angles are also observed for N<sub>2</sub>. The blue curve in each plot corresponds to the fitting given by equation (2). Here, a half sinusoidal oscillation is observed for all angles between 0.5 and 3.5 a.u. The fitted curve is seen to match well upto 3 a.u. for all angles except for 135°. By comparing Figures 6 and 7, it may be observed that for extreme forward angles (20°, 30°, 35°) the frequency of oscillation is almost same for O<sub>2</sub> and N<sub>2</sub>. However, for extreme backward angles (e.g. 135°), the frequency for O<sub>2</sub> is much larger than that for N<sub>2</sub>.

The variation of the oscillation amplitude as a function of the emission angle for both O<sub>2</sub> and N<sub>2</sub> is shown in Figure 8. The green open circles correspond to the amplitude variation for O<sub>2</sub> whereas the blue open triangles are that for N<sub>2</sub>. For both the targets, the amplitude is seen to be higher for the extreme forward and backward angles with the minimum being observed around 90°. Additional experimental and theoretical investigations need to be taken up in order to understand this behaviour. Though qualitatively the variation of the amplitude with angle is seen to be the same for O<sub>2</sub> and N<sub>2</sub>, but quantitatively

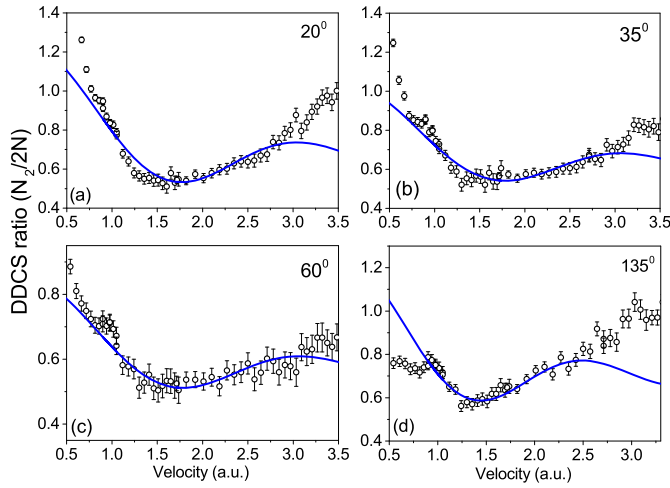


**Fig. 7.** DDCCS ratio ( $\sigma_{N_2}/2\sigma_N$ ). Blue solid line is the Cohen-Fano model fitting to the ratio points.

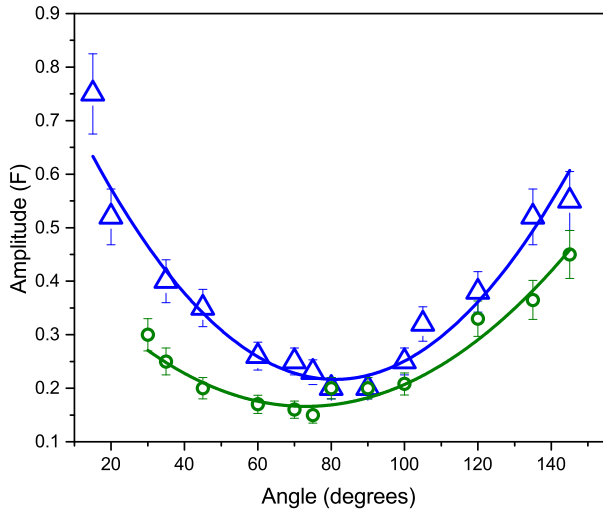


**Fig. 8.** Variation of oscillation amplitude as a function of the emission angle for  $O_2$  and  $N_2$ . The blue open triangles and green open circles represent the data for  $N_2$  and  $O_2$  respectively. The fitted parabolic lines are shown as a guide to eye.

it is observed that the DDCCS ratios for  $N_2$  have higher amplitude of oscillation compared to that for  $O_2$ . In a very recent work [21] on e-impact ionization of  $O_2$ , the interference oscillation has been observed from the forward-backward angular asymmetry parameter which does not require any theoretical cross section.

#### 4.4 Single differential cross section

The DDCCS spectrum when integrated over the electron emission energy or emission angle gives the single differential cross section (SDCS). Integrating the DDCCS spectrum over the emission energy gives the SDCS as a function of the emission angle:

$$\frac{d\sigma}{d\Omega_e} = \int \frac{d^2\sigma}{d\Omega_e d\epsilon_e} d\epsilon_e. \quad (3)$$

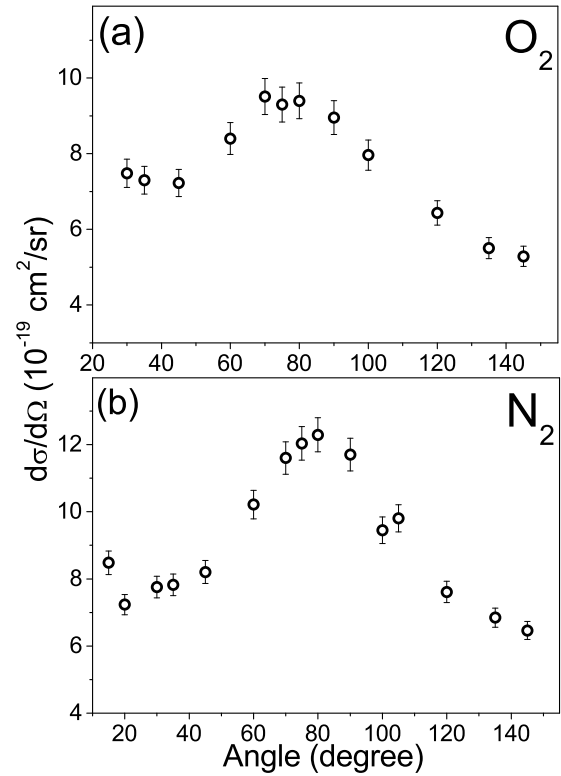


**Fig. 9.** Absolute electron SDCS for  $O_2$  (a) and  $N_2$  (b) as a function of the emission angle.

Similarly, integrating the DDCCS spectrum over the emission angle provides the SDCS as a function of the emission energy:

$$\frac{d\sigma}{d\epsilon_e} = \int \frac{d^2\sigma}{d\epsilon_e d\Omega_e} d\Omega_e. \quad (4)$$

The variation of SDCS as a function of the emission angle is shown in Figures 9a and 9b for  $O_2$  and  $N_2$  respectively. The integration of the DDCCS spectrum has been performed over an energy range of 5–340 eV for  $O_2$  and 5–300 eV for  $N_2$ . From the figure, it is seen that the SDCS for the extreme forward angles remain almost constant. A peaking structure is observed around  $80^\circ$ . Minor signature of forward-backward asymmetry is seen in the SDCS spectrum for  $O_2$  but no such angular asymmetry is observed for  $N_2$ .

Finally by integrating the DDCCS spectrum over the energy and angular range we obtained the total cross section (TCS). The TCS was found to be  $11.2 (\pm 2.2)$  Mb for  $O_2$  and  $14.6 (\pm 2.9)$  Mb for  $N_2$ .

## 5 Conclusion

The absolute DDCCS of the secondary electrons emitted in ionization of  $O_2$  by 7 keV electrons were measured for different forward and backward angles. The secondary electrons having energies between 1 and 600 eV have been detected. The evidence of interference oscillations for the diatomic molecules have been revealed in the DDCCS-ratios. The oscillations were further fitted

by the Cohen-Fano model for interference in molecular double-slit. The frequency of the oscillation for O<sub>2</sub> was found to be higher than that for N<sub>2</sub> for extreme backward angles. Though in the case of fast heavy ion impact, interference oscillations for these molecules are not consensual, the present work reveals a clear signature of interference. This result, however, is in qualitative agreement with the observed oscillations in photoionization. In addition, the SDCS, the TCS and the KLL Auger electron cross sections have also been deduced.

The authors would like to thank Mr. W.A. Fernandes and Mr. Nilesh Mhatre for their help during the experiment.

### Author contribution statement

L.C.T. had initiated the idea and developed the research; conducting experiment, analysis and interpretation were done jointly by M.R.C. and L.C.T.; C.R.S., C.A.T., O.A.F. and R.D.R. provided the theoretical calculations for the atomic targets; M.R.C. and L.C.T. wrote the paper with necessary inputs from R.D.R. and O.A.F.

### References

1. C.B. Opal, W.K. Peterson, E.C. Beaty, *J. Chem. Phys.* **55**, 4100 (1971)
2. H.D. Cohen, U. Fano, *Phys. Rev.* **150**, 30 (1966)
3. N. Stolterfoht, B. Sulik, V. Hoffmann, B. Skogvall, J.Y. Chesnel, J. Rangama, F. Frémont, D. Hennecart, A. Cassimi, X. Husson, A.L. Landers, J.A. Tanis, M.E. Galassi, R.D. Rivarola, *Phys. Rev. Lett.* **87**, 023201 (2001)
4. D. Misra, U. Kadhane, Y.P. Singh, L.C. Tribedi, P.D. Fainstein, P. Richard, *Phys. Rev. Lett.* **92**, 153201 (2004)
5. D. Misra, A. Kelkar, U. Kadhane, A. Kumar, Y.P. Singh, L.C. Tribedi, P.D. Fainstein, *Phys. Rev. A* **75**, 052712 (2007)
6. S. Chatterjee, D. Misra, A.H. Kelkar, Lokesh C. Tribedi, C.R. Stia, O.A. Fojón, R.D. Rivarola, *J. Phys. B* **42**, 065201 (2009)
7. M. Ilchen, L. Glaser, F. Scholz, P. Walter, S. Deinert, A. Rothkirch, J. Seltmann, J. Vieffhaus, P. Decleva, B. Langer, A. Knie, A. Ehresmann, M. Braune, G. Hartmann, A. Meissner, L. Tribedi, M. Al-Khaldi, O. Al-Dossary, U. Becker, *Phys. Rev. Lett.* **112**, 023001 (2014)
8. J.L. Baran, S. Das, F. Járai-Szábo, K. Póra, L. Nagy, J.A. Tanis, *Phys. Rev. A* **78**, 012710 (2008)
9. S. Nandi, A.N. Agnihotri, S. Kasthurirangan, A. Kumar, C.A. Tachino, R.D. Rivarola, F. Martín, L.C. Tribedi, *Phys. Rev. A* **85**, 062705 (2012)
10. S. Nandi, S. Biswas, C.A. Tachino, R.D. Rivarola, L.C. Tribedi, *Eur. Phys. J. D* **69**, 192 (2015)
11. C.A. Tachino, F. Martín, R.D. Rivarola, *J. Phys. B* **45**, 025201 (2012)
12. S.E. Canton, E. Plésiat, J.D. Bozek, B.S. Rude, P. Decleva, F. Martin, *Proc. Natl. Acad. Sci.* **108**, 7302 (2011)
13. R.K. Kushawaha, M. Patanen, R. Guillemin, L. Journel, C. Miron, M. Simon, M.N. Piancastelli, C. Stakes, P. Decleva, *Proc. Natl. Acad. Sci.* **110**, 15201 (2013)
14. H. Chaluvadi, N.O. Zehra, M. Dogan, C. Ning, J. Colgan, D. Madison, *J. Phys. B* **48**, 155203 (2015)
15. M. Roy Chowdhury, C.R. Stia, C.A. Tachino, O.A. Fojón, R.D. Rivarola, L.C. Tribedi, *Phys. Rev. A* **94**, 053703 (2016)
16. M.F. Ciappina, O.A. Fojón, R.D. Rivarola, *J. Phys. B* **47**, 042001 (2014)
17. E. Clementi, C. Roetti, *At. Data Nucl. Data Tables* **14**, 177 (1974)
18. L. Nagy, L. Kocbach, K. Póra, J.P. Hansen, *J. Phys. B* **35**, L453 (2002)
19. N. Stolterfoht, B. Sulik, L. Gulyás, B. Skogvall, J.Y. Chesnel, F. Frémont, D. Hennecart, A. Cassimi, L. Adoui, S. Hossain, J.A. Tanis, *Phys. Rev. A* **67**, 030702(R) (2003)
20. M.E. Galassi, R.D. Rivarola, P.D. Fainstein, *Phys. Rev. A* **70**, 032721 (2004)
21. M. Roy Chowdhury, L.C. Tribedi, *J. Phys. B* **50**, 155201 (2017)

# Electron impact ionization of O<sub>2</sub> and the interference effect from forward–backward asymmetry

Madhusree Roy Chowdhury and Lokesh C Tribedi

Tata Institute of Fundamental Research, Colaba, Mumbai 400005, India

E-mail: [lokesh@tifr.res.in](mailto:lokesh@tifr.res.in) and [ltribedi@gmail.com](mailto:ltribedi@gmail.com)

Received 9 December 2016, revised 15 May 2017

Accepted for publication 19 June 2017

Published 12 July 2017



CrossMark

## Abstract

Absolute double differential cross sections (DDCSs) of secondary electrons emitted from O<sub>2</sub> under the impact of 7 keV electrons were measured for different emission angles between 30° and 145° having energies from 1–600 eV. The forward–backward angular asymmetry was observed from angular distribution of the DDCS of secondary electrons. The asymmetry parameter, thus obtained from the DDCS of two complementary angles, showed a clear signature of interference oscillation. The Cohen–Fano model of Young type electron interference at a molecular double slit is found to provide a good fit to the observed oscillatory structures. The present observation is in qualitative agreement with the recent results obtained from photoionization.

Keywords: ionization, di-atomic molecule, Young type interference, electron emission, angular asymmetry

(Some figures may appear in colour only in the online journal)

## 1. Introduction

The proposition of Cohen and Fano [1] regarding the analogy of electron emission from a homonuclear di-atomic molecule to that of the two slits of Young's double slit experiment for interference effect attracted a great deal of experimental and theoretical work for more than a decade and still continues to be an interesting field of research. Although the initial prediction was in connection with the photoionization of di-atomic molecules, the first set of experiments revealing evidence of the interference effect were carried out using fast heavy ions as projectiles colliding on a H<sub>2</sub> molecule [2–6]. Several experimental and theoretical works have been carried out henceforth to investigate interference oscillation in the ionization of H<sub>2</sub> with heavy ions, electrons and photons as probes [7–12]. The first experimental evidence of the interference effect for fast electrons impacting on D<sub>2</sub> was shown by Fremont and co workers [13]. Further progression from the simplest homonuclear di-atomic molecules H<sub>2</sub> and D<sub>2</sub>, the interference effect was studied in photoionization of a N<sub>2</sub> molecule [14–16]. In the case of heavy ion impact ionization of N<sub>2</sub> and O<sub>2</sub>, the evidence of such an interference effect is not fully conclusive

[17–20]. According to a theoretical prescription by Tachino *et al*, [21] for the proton impact ionization of N<sub>2</sub>, it was inferred that the interference oscillations may not be readily observed in multi-electronic targets due to the cancellation of phase mismatched oscillation contributing from each individual orbitals. Recently, Ilchen *et al* [22] have shown clear interference oscillations in individual orbitals of N<sub>2</sub> and O<sub>2</sub> by photoionization, but the oscillations are out of phase for different orbitals. A detailed theoretical review, along with experimental evidence on coherent electron emission from di-atomic molecules using different probes can be found in [23]. In recent times, apart from investigating the existence of interference oscillations in double differential cross section (DDCS) ratios, some of the other studies involve various aspects of interference oscillations and its application towards the precise structural determination of the molecules [24, 25].

Electrons impart less perturbation to the target system with respect to heavy ions, causing mostly single ionization and less multiple ionization from different orbitals of the target molecules. Therefore, electrons can be considered as a better probe for studying interference phenomena in N<sub>2</sub> and O<sub>2</sub>. Recently, experiments on low and high energy electron

impact ionization of  $N_2$ , measuring the triple differential cross sections (TDCSs) [26] and DDCSs [27], respectively, have been reported. Both the TDCSs and DDCSs ratios revealed signatures of interference oscillations. Extending this work further, we have now investigated for interference oscillation from the electron DDCS spectra, obtained from collisions of fast electrons with  $O_2$ . To the best of our knowledge, such evidence of the interference effect in the case of  $O_2$  with electrons as projectile has not been reported earlier.

In most of the previous work cited above, the interference effect has been revealed from the ratio of molecular-to-atomic cross sections. This method is applied based on the fact that the effect due to interference is very small compared to the steep fall of DDCSs with energy. Hence, interference oscillation is not readily observed in the DDCS spectrum. To enhance the visibility of oscillation, it is necessary to eliminate the variation of cross sections over electron energy and hence the molecular DDCS is divided by the atomic DDCS. Another possible method to look for the interference effect is the use of forward-backward asymmetry, obtained from the measured angular distribution of the electrons emitted from the molecular target [9].

In this work, we report the energy and angular distributions of the DDCS of secondary electrons emitted in ionization of  $O_2$  induced by fast electrons of 7 keV. Further, the interference effect in the case of  $O_2$  has been explored from the asymmetry parameter ( $\alpha(k)$ ) which showed a clear signature of oscillation. In addition to the measurements for  $O_2$ , similar measurements have also been performed for an atomic target, helium, in order to show that Young type interference is absent in the case of such a monocentric target.

## 2. Experimental details

A brief outline of the experimental arrangement is presented here. The projectile electrons of energy 7 keV were obtained from a commercially available electron gun. These fast electrons were guided up to the interaction region in the scattering chamber with the help of Einzel lenses and electrostatic deflectors. In addition to the lenses and deflectors, a pair of magnetic coils were also added in the beamline. Several apertures were used to cut the beam, ensuring a well collimated parallel electron beam with a current of  $\sim 800$  nA, which was used for the present experiment.

The scattering chamber houses a motorized turntable and a hemispherical electrostatic analyzer used for measuring the energy and angular distributions of the secondary electrons. The base pressure in the scattering chamber was  $5 \times 10^{-8}$  mbar, which was achieved with the help of a 2000 l/sec turbo molecular pump backed by a tri-scroll pump. The chamber was flooded with molecular oxygen at an absolute pressure of 0.15 mTorr. To maintain the pressure difference between the scattering chamber and the electron gun, a differentially pumped chamber was connected just before the scattering chamber. The voltages applied on the two electrodes of the

analyzer were set using the following formulae

$$HV_1 = (V_c + \epsilon_e) \frac{R_2 - R_1}{R_1} + V_c \quad (1)$$

$$HV_2 = -(V_c + \epsilon_e) \frac{R_2 - R_1}{R_2} + V_c, \quad (2)$$

where  $R_1$  and  $R_2$  are the radii of the inner and outer hemispheres, respectively, and  $\epsilon_e$  denotes the electron energy. A pre-acceleration voltage ( $V_c$ ) of 6V was applied at the entrance and exit slits of the spectrometer to increase the collection efficiency of the low energy electrons. The Earth's magnetic field was reduced to about 10 mGauss near the interaction region by lining the inner walls of the scattering chamber with  $\mu$ -metal sheets. The electrons ejected from  $O_2$  in collisions with 7 keV projectile electrons were scanned with the hemispherical analyzer for energies between 1–600 eV. The electrons emitted in all directions were scanned by placing the analyzer at different forward and backward angles ( $30^\circ$ ,  $35^\circ$ ,  $45^\circ$ ,  $60^\circ$ ,  $70^\circ$ ,  $75^\circ$ ,  $80^\circ$ ,  $90^\circ$ ,  $100^\circ$ ,  $120^\circ$ ,  $135^\circ$  and  $145^\circ$ ) with respect to the incident beam direction. For the helium target, however, the data were collected for a few forward and backward angles. The number of electrons of a particular energy were detected by a channel electron multiplier (CEM). The front of the CEM was biased to +100 V, since the efficiency of the CEM for electron detection remains almost constant ( $\sim 0.85$ ) for energies between 100 and 700 eV (obtained from the manual). The energy resolution of the analyzer is about 6% of the pass energy and the angular acceptance of the analyzer is  $\pm 3.5^\circ$ . Figure 1 shows a detailed view of the experimental setup.

The absolute DDCS was obtained using the following formula

$$\frac{d^2\sigma}{d\epsilon d\Omega} = \frac{\frac{N_e}{N_p} - \frac{N_b}{N'_p}}{n\Delta\epsilon\eta(I\Omega)_{\text{eff}}}, \quad (3)$$

where  $N_e$  and  $N_b$  are the number of electrons detected in the presence and absence of the target gas inside the interaction chamber,  $N_p$  and  $N'_p$  are the number of projectile electrons with and without the target gas, respectively,  $n$  is the target number density under static gas pressure condition,  $\Delta\epsilon$  is the efficiency of the detector,  $\eta$  is the energy resolution of the analyzer and  $(I\Omega)_{\text{eff}}$  is the solid angle path length integral which is given by

$$(I\Omega)_{\text{eff}} = \frac{w_1 w_2 h_2}{LR \sin(\theta)}, \quad (4)$$

where  $w_1$ ,  $w_2$  and  $h_2$  are the widths and height of the rectangular apertures on the front and back of the collimator,  $L$  is the length of the collimator and  $R$  is the distance of the collimator from the center of the interaction region.

The overall error in the present experiment was about 15%–19%, having contributions from pressure fluctuation, counting statistics, detector efficiency, solid-angle path length integral and resolution of analyzer. The error due to statistical fluctuations was about 2%–5%, except at high energies and extreme backward angles, where the statistical fluctuations were maximum up to 9%–10%.

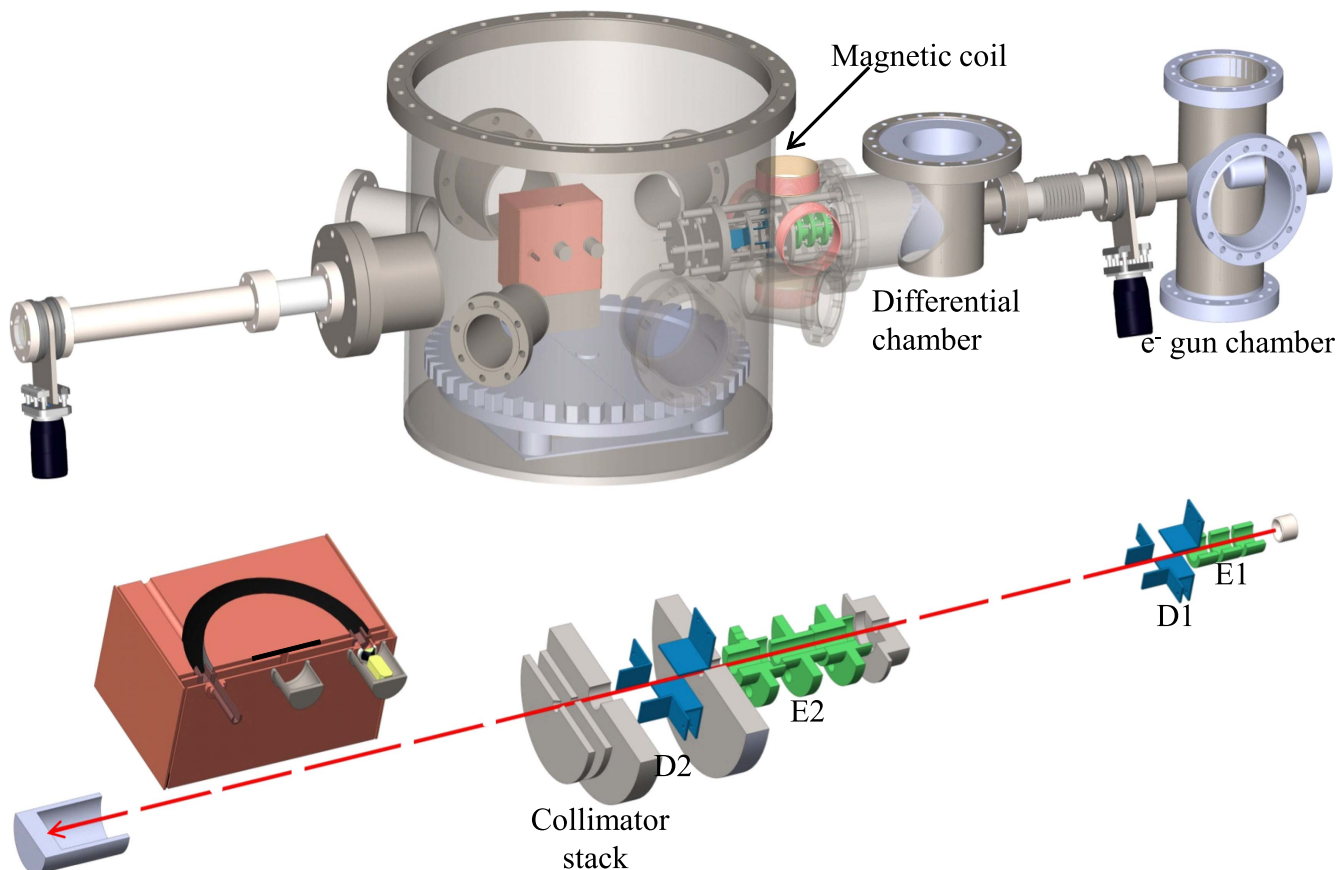


**Figure 1.** Graphical representation of the experimental setup. Upper panel: scattering chamber housing the spectrometer, turntable and the focussing elements; the differential pumping chamber; and electron-gun housing chamber. Three turbo pumping stations attached with these three chambers are not shown. Lower panel: Magnified, cross sectional view of the beamline components (not to scale) along with the spectrometer and Faraday Cup. E1 and D1 are the Einzel lens and electrostatic deflectors, respectively, mounted in the e-gun assembly; similarly, another set of Einzel lens (E2) and deflectors (D2) are mounted in the beamline. Several apertures, placed at different points along the beamline are also shown.

### 3. Results and discussions

#### 3.1. Energy and angular distribution of the electron DDCS

The absolute DDCSs of the emitted electrons from  $O_2$  for fixed electron emission angles are displayed in figure 2. From the figure, it is seen that the cross section decreases by several orders of magnitude in the scanned secondary electron energy range. The DDCS is seen to be maximum in the low energy part of the spectrum. This region is dominated by the soft collision process, where the momentum transfer from the projectile is very less, and hence the electrons are ejected with a large impact parameter. The intermediate part of the spectrum is dominated by the two center effect, where the ejected electron is under the influence of both the projectile and the recoil target nucleus. In the case of electrons as a probe, the two center effect is not a dominant feature compared to highly charged ions. Going further down the spectrum, a sharp peak is observed, at around 480 eV, which is contributed by the K-LL Auger electrons. Since the peak is sitting over a rapidly falling background, the peak position for different angles may vary slightly. However, from the inset in figure 2 it is clear that the peak appears at the expected energy i.e. 480 eV for all the angles.

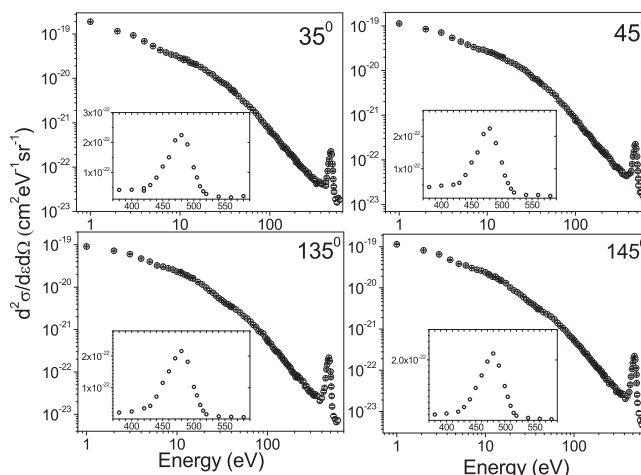


**Figure 2.** Absolute electron DDCS for different forward and backward emission angles. The Auger peaks are displayed in the inset. The statistical errors are shown, which are within the symbol sizes.

Figure 3 displays the measured absolute DDCS of emitted electrons as a function of emission angles for six different electron energies namely 5 eV, 8 eV, 11 eV, 35 eV, 90 eV and 320 eV. The total errors are shown for some points. The angular distributions are seen to be almost flat for the low

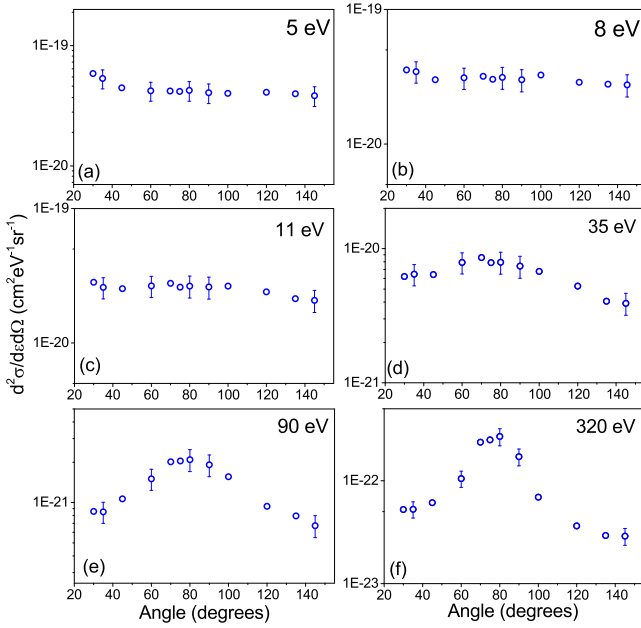


**Figure 3.** The measured absolute DDCS for the fixed electron emission energies as indicated in the different panels. The total errors are shown for few data points.

emission energies. This feature is explained by the fact that in the soft collision region, the cross section is independent of the angle, resulting in a uniform distribution over the measured angular range. At a relatively higher emission energy, the cross section for extreme forward angles is seen to be slightly higher compared to the extreme backward angles. For example, in the case of 90 eV, the cross section for the forward angle ( $30^\circ$ ) is higher than that for the backward angle ( $145^\circ$ ) by a factor of 1.3. Similarly for 320 eV, this factor is about 1.8. This difference in cross section is attributed by the forward–backward angular asymmetry. The peak like structure around  $80^\circ$  for high energies is observed due to the binary nature of collision, where the electrons are elastically scattered by the target nucleus.

### 3.2. Asymmetry parameter

The forward–backward angular asymmetry in the angular distribution spectra arises due to the motion of the electron in the field of two charged particles in the final state and due to the non-Coulombic potential of the multi-electronic target. In the case of electron impact ionization, the former process does not have a major contribution towards asymmetry. The angular asymmetry parameter  $\alpha(k)$  is defined as follows:

$$\alpha(k, \theta) = \frac{\sigma(k, \theta) - \sigma(k, \pi - \theta)}{\sigma(k, \theta) + \sigma(k, \pi - \theta)}, \quad (5)$$

where the electron energy  $\epsilon_k = \frac{k^2}{2}$  is in au and  $\theta$  is the low forward angle. Expanding  $\sigma_k$  in terms of the Legendre polynomials

$$\sigma(k, \theta) = \frac{d^2\sigma}{d\epsilon_e d\Omega_e} = \sum \beta_L P_L(\cos \theta), \quad (6)$$

where  $P_L(\cos \theta)$  is the Legendre polynomial. As already shown by Fainstein *et al* [28], values up to  $L = 2$  contribute mainly to the asymmetry parameter. Calculating  $\alpha(k)$  for  $\theta = 0$  and considering the first few terms of the series expansion, we get

$$\alpha(k) = \frac{\sum_j \beta_{2j+1}(k)}{\sum_j \beta_{2j}(k)} \simeq \frac{\beta_1(k)}{\beta_0(k) + \beta_2(k)}. \quad (7)$$

Thus,  $\alpha(k)$  is the ratio of the odd terms to the summation of even terms. In the present case, we have used  $\theta = 35^\circ$  and  $45^\circ$  for calculating  $\alpha(k, \theta)$ .

### 3.3. Interference oscillation from the asymmetry parameter

From figure 2, it is readily observed, that the variation of cross section over electron emission energies is by several orders of magnitude within few hundreds of eV. On the other hand, the variation due to the interference effect is rather small, and hence it is almost impossible to observe interference oscillations from the energy distribution spectrum. One of the most commonly used tools for deducing the interference oscillations is by dividing the molecular cross section by twice the corresponding atomic cross section. By using this technique, we can negate the cross section variation over energy, and only the oscillatory structures arising from the interference effect, if any, are observed. The drawback of this well known technique is that, it may be a difficult task to produce atomic oxygen for the measurement of the electron emission cross sections. In the absence of measured atomic DDCSs, one uses the theoretical cross sections for the atomic targets, and thus the DDCS ratios are obtained by dividing the measured molecular cross sections by twice the theoretical cross sections of the atomic target to reveal the interference oscillations. As shown in our earlier work [27], the shape and value of the experimental-to-theoretical DDCS ratios are highly sensitive to the different effective charges used for atomic cross section calculations. Thus, it is important to check for interference oscillation which is devoid of the choice of effective charge used in the atomic calculations. On the other hand, the theoretical calculation for ionization of molecular  $O_2$ , which needs a proper description of molecular wavefunction, is not presently available to us. Therefore, a complete theoretical DDCS ratio ( $O_2$ -to-2O) is also not available.

In this regard, the other method used for observing the interference oscillation is from the forward–backward asymmetry parameter (FBAP). In this process, only the measured DDCS, at forward and backward angles, for the molecular target are used for deriving the oscillatory structures. Since this method essentially uses the ratios of measured DDCS, hence it is free from the normalization procedure used to obtain the absolute DDCS. Also, it does not require the DDCS of an atomic target and hence is independent of the choice of effective charge. Therefore in this paper, instead of studying the experimental-to-theoretical DDCS ratios, we present the results on the FBAP.

We have calculated the FBAP [ $\alpha(k, \theta)$ ] from the measured DDCS for two sets of complementary angles i.e.  $35^\circ$ – $145^\circ$  and  $45^\circ$ – $135^\circ$ . Figures 4 and 5 display the variation of  $\alpha(k, \theta)$  as a

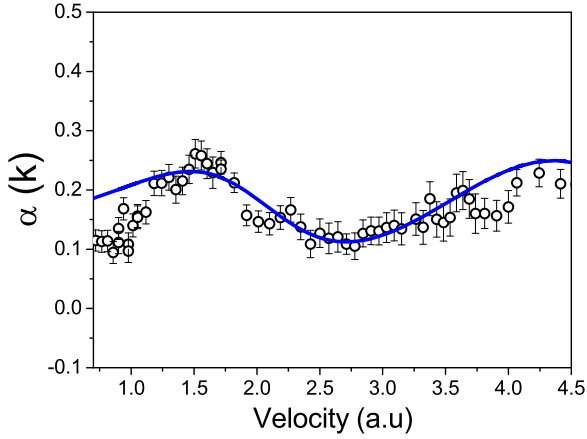


**Figure 4.** Forward–backward asymmetry parameter obtained from the DDCS of two complementary angles i.e.,  $35^\circ$  and  $145^\circ$ . The solid line represents the fitted curve (equation (9)).

function of emitted electron velocity. A full sinusoidal oscillation is observed in both the figures within the ejected electron velocity range of 0.7 to 4.5 au (in figure 4) and 1.0 to 4.2 au (figure 5). In agreement with earlier studies [2, 3], the frequency of oscillation is found to be more in the case of backward angles compared to the forward angles. This difference in frequency between the two complementary angles produces the oscillation in  $\alpha(k)$ . Though in the case of  $\theta = 35^\circ$ , the oscillation is observed about a horizontal line around 0.16, but for  $\theta = 45^\circ$ , the oscillation is seen to vary between 0.06 and 0.3 with an increasing trend in the high velocity region. The entire experiment was performed with good counting statistics, which ensured that the observed oscillations in  $\alpha(k)$  were not contributed from statistical fluctuations. In addition to the observed oscillatory structure in  $\alpha(k)$  for  $O_2$ , the inset of figure 5 displays the variation of  $\alpha(k)$  as a function of velocity in the case of an atomic target, such as, helium. The FBAP for helium is seen to increase monotonically with velocity. Such a monotonic behaviour is well known and a quite general phenomenon for ion–atom collisions involving atomic H, He and multi-electronic atoms [29, 30]. The black dashed line in the inset is a guiding line to indicate the steady increase of the FBAP for He atom, in contrast to the oscillations seen for the  $O_2$  molecule.

The asymmetry parameter for  $O_2$  has been fitted with a model based on the formalism proposed by Cohen and Fano on Young type interference from a molecular double slit. The DDCS for  $O_2$  (under dipole approximation) can be written as [2]

$$\sigma_{O_2}(k, \theta) = A(k) \left[ 1 + \frac{\sin(kc(\theta)d)}{kc(\theta)d} \right]. \quad (8)$$

Here  $k$  represents the electron momentum in au,  $d$  is the internuclear distance (2.28 au for  $O_2$ ) and  $A(k)$  is an exponentially decreasing function of velocity, which attributes to the incoherent non-oscillatory part that corresponds to the atomic cross section. The quantity  $c(\theta)$  is an adjustable frequency parameter and the term  $\frac{\sin(kc(\theta)d)}{kc(\theta)d}$  is known as the

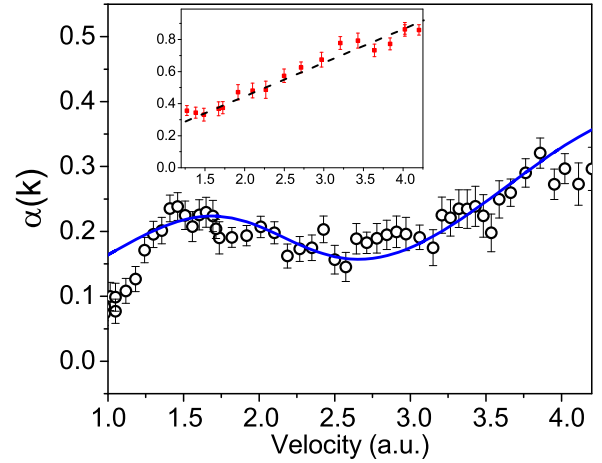


**Figure 5.** Asymmetry parameter for angles  $45^\circ$  and  $135^\circ$  along with the fitting (solid line). Inset: asymmetry parameter derived for He using the same complementary angles, black dashed line is a guide to eye.

Cohen–Fano term [1, 2]. As shown by Nagy *et al* [31], if the momentum transfer is neglected completely, then  $c = 1$ , whereas if only the transverse component of momentum transfer is neglected then, using a peaking approximation it is found that the frequency  $c = \cos(\theta)$ . In the case of  $H_2$ , it has been observed that for backward emission angles, the oscillation frequency is higher than the corresponding forward angles, indicating a deviation from the  $\cos(\theta)$  dependence [8, 9]. Considering both the electron and heavy ion impact on  $H_2$ , Chatterjee *et al* [32] have given a functional form of  $c(\theta)$ . On the other hand, for  $N_2$ , it has been shown recently [27] that the functional form  $c(\theta)$  differs from that observed in the case of  $H_2$ .

It was shown by Stolterfoht *et al* [2] that the oscillatory term survived in the DDCS expression (in equation (8)) even after integrating over all possible orientations of the molecule. The expression was applied in the case of  $H_2$ . However, the same behaviour is expected even for other homonuclear diatomic molecules, such as,  $O_2$ .

Replacing  $\sigma(k, \theta)$  in equation (5) by that in equation (8), we get the following expression for  $\alpha(k)$  :

$$\alpha(k) = \frac{k\beta c(\theta)d(A - B) + [A\beta \sin(kc(\theta)d) - B \sin(k\beta c(\theta)d)]}{k\beta c(\theta)d(A + B) + [A\beta \sin(kc(\theta)d) + B \sin(k\beta c(\theta)d)]}, \quad (9)$$

where,  $A$  and  $B$  are the amplitudes of oscillation for the two complementary angles,  $c(\theta)$  is the frequency of the forward angle,  $\theta$  ( $= 35^\circ$  and  $45^\circ$  in the present case),  $\beta$  is the ratio of oscillation frequency for backward to forward angles, i.e.  $c(\pi - \theta)/c(\theta)$  and other symbols remain same as those in equation (8). The model fitting, as a function of velocity is shown by the solid blue lines in figures 4 and 5. The fitted curve is seen to have an overall good agreement with the calculated values of  $\alpha(k)$ , except for the very low velocity region. In this region, though a qualitative agreement is seen, but quantitatively, the fitting overestimates the derived values of  $\alpha(k)$ . The fitting parameter  $\beta$ , which was found to be 1.14

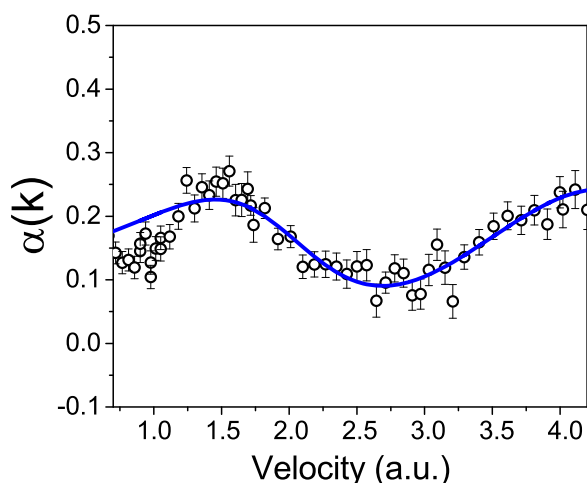


**Figure 6.** Asymmetry parameter for angles  $30^\circ$  and  $145^\circ$ . Blue solid line showing the fitted curve (equation (9)).

for  $\theta = 35^\circ$  and 1.15 for  $\theta = 45^\circ$ , provided a good fitting to the asymmetry parameter.

The asymmetry parameter has also been derived for two non-complementary angles i.e.  $30^\circ$  and  $145^\circ$  (shown in figure 6). A clear oscillatory structure is seen about a horizontal line in the velocity range of 0.7 to 4.2 au. The fitted curve matches well beyond 1.25 au. The oscillatory structure in figure 6 looks similar to those observed in figures 4 and 5. This behaviour is due to the fact that the DDCS values for angles near  $35^\circ$  do not vary much, which can be seen in figure 3. Hence, it is seen that exactly two complementary angles are not an absolute necessity for observing the oscillations in  $\alpha(k)$ . Preferably, one low forward angle and a high backward angle suffice for revealing the oscillation in asymmetry parameter.

#### 4. Conclusions

We have measured the absolute DDCS of the secondary electrons emitted from 7 keV electron impact ionization of  $O_2$  molecule. The cross sections were measured for electron energies between 1 and 600 eV within an angular range of  $30^\circ$ – $145^\circ$ . The angular distribution of the DDCS spectra showed forward–backward asymmetry. The asymmetry parameter,  $\alpha(k)$ , was derived from the measured DDCS for two sets of complementary angles which revealed clear signature of oscillations. A good fitting to the asymmetry parameter by the Cohen–Fano model, provided unambiguous evidence of the interference effect in the case of electron impact ionization of  $O_2$ . To make a comparative study between the molecular and atomic target, the asymmetry parameter was also calculated for helium, which showed monotonically increasing behaviour as compared to the oscillations observed for the  $O_2$  molecule.

#### References

- [1] Cohen H D and Fano U 1966 *Phys. Rev.* **150** 30
- [2] Stolterfoht N *et al* 2001 *Phys. Rev. Lett.* **87** 023201
- [3] Misra D, Kadhane U, Singh Y P, Tribedi L C, Fainstein P D and Richard P 2004 *Phys. Rev. Lett.* **92** 153201
- [4] Hossain S, Landers A L, Stolterfoht N and Tanis J A 2005 *Phys. Rev. A* **72** 010701(R)
- [5] Tanis J A, Hossain S, Sulik B and Stolterfoht N 2005 *Phys. Rev. Lett.* **95** 079301
- [6] Misra D, Kadhane U, Singh Y P, Tribedi L C, Fainstein P D and Richard P 2005 *Phys. Rev. Lett.* **95** 079302
- [7] Galassi M E, Rivarola R D, Fainstein P D and Stolterfoht N 2002 *Phys. Rev. A* **66** 052705
- [8] Stolterfoht N *et al* 2003 *Phys. Rev. A* **67** 030702(R)
- [9] Misra D, Kelkar A, Kadhane U, Kumar A and Tribedi L C 2006 *Phys. Rev. A* **74** 060701(R)
- [10] Misra D, Kelkar A, Kadhane U, Kumar A, Singh Y P, Tribedi L C and Fainstein P D 2007 *Phys. Rev. A* **75** 052712
- [11] Chatterjee S, Misra D, Kelkar A H, Tribedi L C, Stia C R, Fojón O A and Rivarola R D 2009 *J. Phys. B: At. Mol. Opt. Phys.* **42** 065201
- [12] Akoury D *et al* 2007 *Science* **318** 949
- [13] Kamalou O, Chesnel J Y, Martina D, Hanssen J, Stia C R, Fojon O A, Rivarola R D and Fremont F 2005 *Phys. Rev. A* **71** 010702(R)
- [14] Rolles D *et al* 2005 *Nature* **437** 711
- [15] Liu X J *et al* 2006 *J. Phys. B: At. Mol. Opt. Phys.* **39** 4801
- [16] Ueda K *et al* 2006 *Chem. Phys.* **329** 329
- [17] Winkworth M, Fainstein P D, Galassi M E, Baran J L, Dassanayake B S, Das S, Kayani A and Tanis J A 2009 *Nucl. Instrum. Methods Phys. Res., Sect. B* **267** 373
- [18] Baran J L, Das S, Járfai-Szábó F, Póra K, Nagy L and Tanis J A 2008 *Phys. Rev. A* **78** 012710
- [19] Nandi S, Agnihotri A N, Kasthurirangan S, Kumar A, Tachino C A, Rivarola R D, Martin F and Tribedi L C 2012 *Phys. Rev. A* **85** 062705
- [20] Nandi S, Biswas S, Tachino C A, Rivarola R D and Tribedi L C 2015 *Eur. Phys. J. D* **69** 192
- [21] Tachino C A, Martin F and Rivarola R D 2012 *J. Phys. B: At. Mol. Opt. Phys.* **45** 025201
- [22] Ilchen M *et al* 2014 *Phys. Rev. Lett.* **112** 023001
- [23] Ciappina M F, Fojon O A and Rivarola R D 2014 *J. Phys. B: At. Mol. Opt. Phys.* **47** 042001
- [24] Canton S E, Plésiat E, Bozek J D, Rude B S, Decleva P and Martin F 2011 *Proc. Natl Acad. Sci. USA* **108** 7302
- [25] Kushawaha R K, Patanen M, Guillemin R, Journel L, Miron C, Simon M, Piancastelli M N, Stakes C and Decleva P 2013 *Proc. Natl Acad. Sci. USA* **110** 15201
- [26] Chaluvadi H, Zehra N O, Dogan M, Ning C, Colgan J and Madison D 2015 *J. Phys. B: At. Mol. Opt. Phys.* **48** 155203
- [27] Chowdhury M R, Stia C R, Tachino C A, Fojon O A, Rivarola R D and Tribedi L C 2016 *Phys. Rev. A* **94** 052703
- [28] Fainstein P D, Gulyás L, Martin F and Salin A 1996 *Phys. Rev. A* **53** 3243
- [29] Tribedi L C, Richard P, DeHaven W, Gulyas L, Gealy M W and Rudd M E 1998 *J. Phys. B: At. Mol. Opt. Phys.* **31** L369
- [30] Biswas S, Misra D, Monti J M, Tachino C A, Rivarola R D and Tribedi L C 2014 *Phys. Rev. A* **90** 052714
- [31] Nagy L, Kocbach L, Pora K and Hansen J P 2002 *J. Phys. B: At. Mol. Opt. Phys.* **35** L453
- [32] Chatterjee S, Misra D, Fainstein P D and Tribedi L C 2011 *Phys. Scr.* **T144** 014040

**Ionization of N<sub>2</sub> in collisions with fast electrons: Evidence of an interference effect**Madhusree Roy Chowdhury,<sup>1</sup> C. R. Stia,<sup>2</sup> C. A. Tachino,<sup>2</sup> O. A. Fojon,<sup>2</sup> Roberto D. Rivarola,<sup>2</sup> and Lokesh C. Tribedi<sup>1,\*</sup><sup>1</sup>Tata Institute of Fundamental Research, Colaba, Mumbai 400005, India<sup>2</sup>Institute de Fisica Rosario (CONICET-UNR), Universidad Nacional de Rosario, 2000 Rosario, Argentina

(Received 21 August 2016; published 14 November 2016)

Absolute double differential cross sections (DDCS) of electron emission were measured for ionization of N<sub>2</sub> by fast electrons with energy 7 keV. Measurements were performed for different electron emission angles and energies. Evidence of oscillation due to Young-type interference was observed in the DDCS ratios for all angles. The frequency for large backward angle is found to be larger compared to that for small forward angle. Consequently, the forward-backward asymmetry parameter reveals the oscillatory structure even more clearly. The oscillations observed for both experimental-to-theoretical DDCS ratios and forward-backward asymmetry were well explained by the Cohen-Fano model of interference in a molecular double slit. A periodic deviation of the Cohen-Fano model from the asymmetry parameter data reveals the presence of a higher-frequency component. The first Born model was employed to explain the results of molecular nitrogen for which a complete-neglect-of-differential-overlap approximation was used along with an effective atomic number.

DOI: [10.1103/PhysRevA.94.052703](https://doi.org/10.1103/PhysRevA.94.052703)**I. INTRODUCTION**

Electron-impact ionization of atoms and molecules is an important field in the study of basic atomic collision physics. There have been numerous experimental and theoretical investigations in this field for many decades. Many aspects of electron-induced ionization are being investigated, such as total cross sections, single and double differential cross section (DDCS), e-2e and e-3e collision processes, as well as double and multiple ionizations [1,2]. The e-DDCS spectrum carries rich information regarding the collision mechanisms compared to the single differential and total cross sections. Such measurements of the absolute cross sections at the DDCS level are scarce, although it has major applications in other fields, such as plasma physics, astrophysics, cluster physics, and, in general, atomic collision physics involving photons, electrons, and ions as projectiles.

However, other fundamental processes which have implications for basic quantum physics, such as Young-type electron interference from a molecular double slit which is a relatively new feature, can be well investigated from an electron DDCS spectrum arising from such collisions. Such an interference and the resulting oscillation in the electron spectrum was predicted by Cohen and Fano in 1966 [3]. Investigation of the interference effect in the electron emission spectrum arising from a diatomic molecule in collision with photons, electrons, and fast heavy ions has been the subject of intensive experimental and theoretical studies. For homonuclear diatomic molecules, since the two atomic centers are indistinguishable, the probability of electron emission from either atom is expected to add coherently, resulting in an interference effect. The two atoms are analogous to the two slits in Young's double-slit experiment on light scattering, which played a major role in the formation and progress of quantum mechanics.

Experiments on ionization of H<sub>2</sub> by heavy ions, electrons, and photons [4–11] were performed to investigate the interference effect. Similarly, other diatomic molecules, such as

N<sub>2</sub>, O<sub>2</sub>, and CO [11–23], have been the subject of study in recent years to look for an interference effect. Although in the case of H<sub>2</sub>, evidence of an interference effect was seen for both heavy-ion and electron impact, for multielectronic targets such as O<sub>2</sub> and N<sub>2</sub>, there is an ambiguity in such observation in the case of heavy-ion impact. For the N<sub>2</sub> molecule, the oscillation which was observed by proton impact [12] has been interpreted to have the signature of a second-order scattering process only. On the other hand, in the case of H<sub>2</sub>, a double-collision model was used [24,25] to explain the observed double-frequency component (second-order process), along with the presence of a first-order Cohen-Fano oscillation. According to the continuum distorted wave-eikonal initial state (CDW-EIS) model [26], for proton impact ionization of N<sub>2</sub>, oscillations are visible in individual orbitals, which are phase shifted from each other. Thus, adding up the contributions from all orbitals leads to the cancellation of intensities and therefore the DDCS spectra may not reveal any signature of oscillation. The recent experimental work on the DDCS measurement of N<sub>2</sub> [16] did not show any appreciable oscillation, also for O<sub>2</sub>, where no oscillation was observed [17]. On the contrary, Ilchen *et al.* [18] demonstrated the existence of interference oscillation in photoionization of 1σ<sub>g</sub> and 1σ<sub>u</sub> orbitals of N<sub>2</sub> molecule. There exists a phase mismatch in the oscillations of these two individual orbitals. Similarly, interference oscillation was observed clearly in the vibrationally resolved states of N<sub>2</sub> [11].

Fast electrons impart much weaker perturbation to the target as compared to fast heavy ions during collision. It is well known that heavy ions cause simultaneous multiple ionization of outer shells of atoms along with single ionization. Thus, multiple ionization of different orbitals complicates the process, which as a result may create difficulty in observing the oscillations. In the case of fast electron collisions, the probability of multiple ionization is much less compared to that for heavy-ion collisions [27]. In this work, we present the DDCS spectra of the secondary electrons ejected due to the collision of fast electrons with N<sub>2</sub> and a clear signature of first-order interference effect is visible from the DDCS ratios, which is in partial agreement with the observation in [14]. The DDCSs are measured as a function of emitted electron

\*lokesh@tifr.res.in; ltribedi@gmail.com

energy and angle. The forward-backward angular asymmetry parameter and the details of the interference oscillation are deduced from the measured DDCS spectra.

## II. EXPERIMENTAL DETAILS

We present a brief sketch of the experimental setup used for the measurement of energy and angular distributions of the secondary electrons. The experiment has been performed with a 7 keV (projectile velocity  $v_p \sim 22.7$  a.u.) electron beam obtained from a commercially available electron gun. These fast electrons were initially focused using a set of einzel lens and deflectors present within the electron gun assembly. Electron being a light mass particle and the distance between the electron gun filament and interaction region in the scattering chamber being quite large ( $\sim 1.5$  m), one set of lens and deflectors was not sufficient to get a well-collimated parallel beam near the interaction region. Another set of einzel lens, a pair of electrostatic deflectors, and a collimator stack with three collimators were incorporated in the beam line to focus the beam. The last aperture of 2.5 mm diameter was used to cut the beam before it reached the interaction region. For better alignment, two sets of magnetic coils were also introduced in the beam line. Finally, a well-collimated parallel beam was directed to the  $N_2$  target gas present in the scattering chamber. The beam current was typically around 900 nA, which remained almost stable throughout the experimental process with minor fluctuation in the presence and absence of gas.

The collision processes took place in a high vacuum scattering chamber made of stainless steel having diameter of 18 inches. It is equipped with a motorized turntable and a hemispherical electrostatic analyzer. A base pressure of  $7 \times 10^{-8}$  mbar was achieved with a 2000 l/sec turbo molecular pump backed by a triscroll pump. The chamber was flooded with the target gas (molecular nitrogen) at an absolute pressure of 0.15 mTorr, which was measured by a capacitance manometer (MKS Baratron). The Earth's magnetic field was reduced to about 5–10 mGauss near the interaction region by placing two  $\mu$  metal sheets on the inner side of the scattering chamber. In addition, it was also ensured that the electric and magnetic field due to the lens and deflectors in the beam line did not have any effect on the emitted secondary electron spectrum, particularly for the low-energy electrons. The electrons ejected from the target after the collision process were energy analyzed by the hemispherical electrostatic analyzer sitting on the turntable. The hemispherical analyzer has an inner and outer diameter of 25 and 35 mm, respectively. A preacceleration voltage of 6 V was applied at the entrance and exit slit of the spectrometer to enhance the collection efficiency of the low-energy electrons ( $< 5$  eV) which otherwise may be deflected by the presence of any stray electric or magnetic field near the interaction region. The energy-analyzed electrons were detected by a channel electron multiplier (CEM) placed after the exit slit of the hemispherical analyzer. The cone of the CEM was kept at a positive potential of 100 V because the detection efficiency of the CEM remains constant (0.85) for electron energies between 100–500 eV, as obtained from the operation manual of the detector. Since the chamber is flooded with target gas, the collision volume is extended along the electron beam and therefore the acceptance angle of the

analyzer varies between  $3.4^\circ$  to  $3.6^\circ$  based on the emission angle. The corresponding estimated average uncertainty in electron emission angle is about  $3.7^\circ$ . Energy resolution of the analyzer is about 6% in which the contribution due to the acceptance angle is about 1% (see Ref. [28]). At each energy, the number of electrons ejected were detected for a specified amount of incident projectile charge collected on a Faraday cup. A LABVIEW-based data acquisition system was used for scanning the voltages on the hemispheres and to collect the data for different electron energies.

The secondary electrons having energies of 1–550 eV were detected for different angles from  $15^\circ$  to  $145^\circ$ . The error due to statistical fluctuation was low (4%–6%) throughout the experiment. Gas pressure fluctuation was about 6% to 7%. The maximum absolute error in the data for the present experiment was about 15%.

## III. THEORETICAL MODELS

The DDCS of ionization of  $N_2$  molecules is obtained by the method proposed by Senger *et al.* [29], developed in the framework of the complete neglect of differential overlap (CNDO) approximation [30]. Briefly, molecular orbitals (MOs) are constructed from a linear combination of atomic orbitals in a self-consistent field approach by using a minimal basis size: only atomic orbitals of those which are occupied in the ground state of the atoms of the molecule are utilized. In this treatment, the weight of such atomic contributions is expressed in terms of the electronic population.

For the ground state of the  $N_2$  molecule, the electronic configuration is  $(N 1s)^4 (\sigma_g 2s)^2 (\sigma_u 2s)^2 (\pi_u 2p)^4 (\sigma_g 2p)^2$ . The contribution of the different atomic states to the MO extracted from Ref. [31] is shown in Table I, as well as the corresponding measured MO binding energies taken from Ref. [32]. As a consequence, in the monocentric CNDO model, the DDCS for a particular MO reduces to a sum of the cross sections for N atomic compounds weighted by the weights resulting from the Mulliken population analysis for the considered MO (see Table I) [29]. The total DDCS for the molecule is obtained then as a sum of all MO contributions.

The electronic configuration of the ground state  $^4S_{3/2}$  of the N atom is  $(1s)^2(2s)^2(2p)^3$ . Within the framework of an independent electron model, the multielectronic problem is reduced to a single-electron one under the following assumption. It is supposed that one of the target electrons (the *active* electron) is ionized in the final channel of the reaction, whereas the other ones (the *passive* electrons) remain as frozen in their initial orbitals. Hence, no appreciable relaxation of the target is assumed during the effective collision time, which is

TABLE I. Population and experimental binding energies of the  $N_2$  molecular orbitals (MOs).

MO	Population [31]	Expt. energy (eV) [32]
$N 1s$	4.00 $N 1s$	−409.90
$\sigma_g 2s$	1.50 $N 2s$ + 0.50 $N 2p$	−37.23
$\sigma_u 2s$	1.47 $N 2s$ + 0.53 $N 2p$	−18.60
$\pi_u 2p$	4.00 $N 2p$	−16.80
$\sigma_g 2p$	0.5 $N 2s$ + 1.50 $N 2p$	−15.50

justified as the latter is much less than the relaxation time of the target at the impact energies of interest [33].

The DDCCS for a particular orbital of the N target is obtained from the following expression:

$$\frac{d^2\sigma}{d\Omega_e dE_e} = (2\pi)^4 \frac{k k_s}{k_i} \int d\Omega_s |t_{fi}|^2, \quad (1)$$

where  $\mathbf{k}$  and  $\mathbf{k}_s$  are the momenta of the *active* ejected electron and the scattered one, respectively, whereas  $d\Omega_e$  and  $d\Omega_s$  represent the corresponding differential solid angles with respect to the incidence direction defined by the incident-electron momentum  $\mathbf{k}_i$ . Moreover,  $E_e = k^2/2$  is the energy of the emitted electron.

The *prior* version of the transition-matrix element reads

$$t_{fi} = \langle \psi_f^- | V_i | \psi_i \rangle, \quad (2)$$

where  $\psi_i$  is the wave function in the initial channel and  $\psi_f^-$  is the final wave function with correct asymptotic conditions.  $V_i$  is the perturbation in the entrance channel.

The initial wave function is chosen as a product between a plane wave for the incident projectile and a bound-state wave function  $\phi_j$  for the active electron,

$$\psi_i = \frac{e^{i\mathbf{k}_i \cdot \mathbf{R}}}{(2\pi)^{3/2}} \phi_j(\mathbf{r}), \quad (3)$$

where  $\mathbf{R}$  and  $\mathbf{r}$  are the position vectors of the incident electron and the active electron, respectively. Atomic orbitals  $\phi_j$  ( $j = 1s, 2s, 2p$ ) are described here within the Roothaan-Hartree-Fock approximation [34].

In the first Born approximation, the final-state wave function is chosen as

$$\psi_f^- \cong \frac{e^{i\mathbf{k}_f \cdot \mathbf{R}}}{(2\pi)^{3/2}} C(\mathbf{k}, \mathbf{r}, \gamma), \quad (4)$$

where

$$C(\mathbf{k}, \mathbf{r}, \nu) = \Gamma(1 - i\gamma) \frac{e^{i\mathbf{k} \cdot \mathbf{r}}}{(2\pi)^{3/2}} e^{-\pi\gamma/2} \times {}_1F_1[i\gamma; 1; -i(kr + \mathbf{k} \cdot \mathbf{r})] \quad (5)$$

describes the ionized electron in the field of the residual target at asymptotically large distances.  ${}_1F_1$  is the confluent hypergeometric function and  $\gamma = -Z_T/k$  is the corresponding Sommerfeld parameter. Here,  $Z_T$  is an effective charge corresponding to the residual target *seen* by the active electron.

According to the choice of the initial state, the perturbation  $V_i$  in the initial channel is taken as

$$V_i = \frac{1}{r_p} - \frac{1}{R}, \quad (6)$$

where  $\mathbf{r}_p = \mathbf{r} - \mathbf{R}$  is the position vector of the active electron with respect to the projectile. The perturbation  $V_i$  corresponds to the interaction of the projectile with the *active* electron and with a net charge equal to unity. This is compatible with the complete screened charge of the nuclei by the *passive* electrons.

In order to evaluate the influence of the passive electrons in the final channel, either an asymptotic charge  $Z_T = 1$ , which corresponds to a total screening of the nucleus, or

$Z_T = Z_{bk} = \sqrt{-2n_j^2\epsilon_j}$  [35] is used in the DDCCS calculations for both N and N<sub>2</sub> targets. For the case of atomic cross-section calculations,  $\epsilon_j$  is the Roothaan-Hartree-Fock energy [34], whereas for N<sub>2</sub> computations,  $\epsilon_j$  represents the MO energies shown in Table I. In both cases,  $n_j$  is the principal quantum number of the atomic orbital involved in the calculations. Further details can be found in Ref. [36].

## IV. RESULTS AND DISCUSSIONS

In this section, the experimentally observed DDCCS spectra for the N<sub>2</sub> target and consequently the interference oscillations obtained from the DDCCS ratios are discussed along with the forward-backward asymmetry.

### A. Energy distribution of electron DDCCS at fixed emission angles

The measured absolute electron DDCCSs for N<sub>2</sub> as a function of emitted electron energy for four different emission angles are shown in Fig. 1. The theoretical cross sections for N<sub>2</sub> and 2N, calculated using effective charges  $Z_T = 1$  and  $Z_T = Z_{bk}$ , are also plotted. From the figure, it is seen that the cross section decreases over four orders of magnitude in the measured electron energy range. In the low-energy part of the spectrum, the cross section reaches a maximum due to the contribution from the soft electron emission process where the momentum transfer is small and the electrons are emitted with very large impact parameter. The calculations for N<sub>2</sub> and 2N are seen to merge almost completely for either values of  $Z_T$ . The calculation with  $Z_T = 1$  matches with the experimental data qualitatively, but overestimates it for all angles. The calculation corresponding to  $Z_{bk}$  is seen to have better agreement with data beyond 20 eV for all angles. For extreme backward angles,  $Z_T = Z_{bk}$  underestimates the data. In the low-energy region,

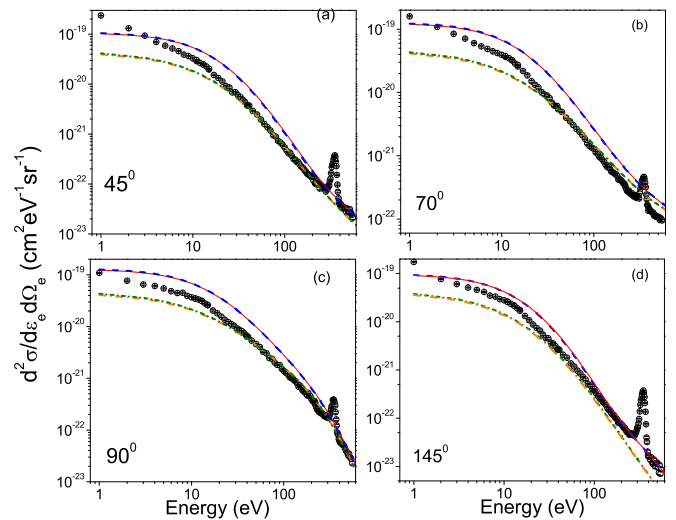


FIG. 1. Absolute DDCCS for different emission angles: Theoretical cross sections for N<sub>2</sub> (red solid line) and 2N (blue dashed line) corresponding to  $Z_T = 1$  are displayed. The calculations using  $Z_T = Z_{bk}$  are also shown by the orange dash-dotted line (N<sub>2</sub>) and green dotted line (2N). The calculations for N<sub>2</sub> and 2N, being almost identical, cannot be distinguished.

the discrepancy between data and theoretical calculation using  $Z_{bk}$  is larger in the case of forward angles compared to the backward angles. The sharp peak observed at about 355 eV corresponds to the K-LL Auger electron emission, which is not taken into account in the theoretical calculations. The DDCS for  $N_2$  (under dipole approximation) can be written as [4]

$$\sigma_{N_2}(k, \theta) = \sigma_{2N}(k) \left[ 1 + \frac{\sin[kc(\theta)d]}{kc(\theta)d} \right]. \quad (7)$$

Here,  $k$  represents the electron momentum in a.u. and  $d$  is the internuclear distance (2.1 a.u. for  $N_2$ ). The quantity  $c(\theta)$  is an adjustable frequency parameter, and the term  $\frac{\sin[kc(\theta)d]}{kc(\theta)d}$  is known as the Cohen-Fano term [3,4,37]. The DDCS for 2N ( $\sigma_{2N}$ ) was obtained from theoretical calculations. The ratio  $\text{DDCS}(N_2)/2\text{DDCS}(N)$  shows the interference oscillation, which is discussed in the following section.

### B. Angular distribution of electron DDCS at fixed emission energies

Figure 2 displays the angular distribution of DDCS for different electron emission energies. An absolute error of 15% is shown for some data points. The four theoretical curves correspond to the cross sections for  $N_2$  and 2N with the effective charge  $Z_T = 1$  and  $Z_T = Z_{bk}$ . The theoretical calculations match qualitatively with the data, but  $Z_T = 1$  overestimates the measured values in all cases. The calculations with  $Z_{bk}$  underestimate the data for 9 eV, but match qualitatively for higher energies. A closer inspection into the plots for 120 and 200 eV show that the curves for  $Z_T = Z_{bk}$  are below the measured values for extreme forward and backward angles. In the case of low emission energies, the distributions are almost flat, but with the increase in electron emission energy, the distributions gradually show a peaking structure around  $80^\circ$ . This difference in the shape of the distribution for low and high energy is understood in terms of the binary nature of collisions. Further, from the figure it is readily seen that for lower electron energies, the DDCS values are almost the same for extreme forward and backward angles. However, with the increase in energy, the DDCS for forward angles is

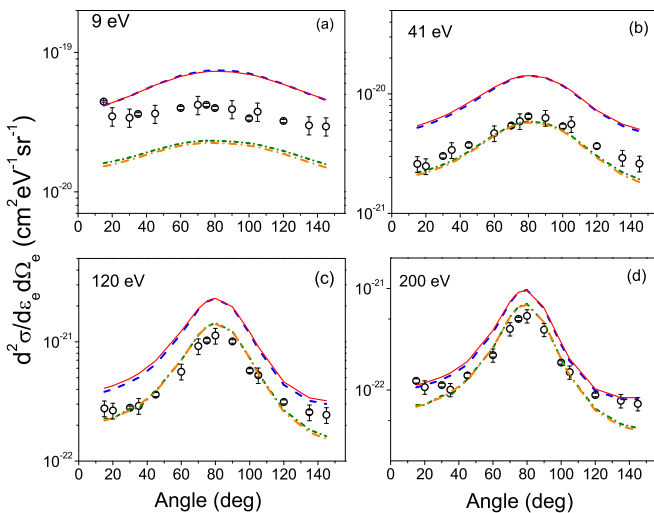


FIG. 2. Absolute DDCS for fixed electron emission energies. Legends are similar to that mentioned in Fig. 1.

slightly greater than for backward angles. This behavior is also reproduced qualitatively by the theoretical calculations, although they do not match quantitatively with data. It can be inferred that there is only minor signature of forward-backward angular asymmetry in the case of electron-impact collisions.

### C. DDCS ratios

#### 1. Experimental-to-theoretical DDCS ratios

As seen from Fig. 1, the DDCSs for  $N_2$  and independent N atoms fall by several orders of magnitude with the electron energy, whereas the variation due to the interference effect is rather small. To enhance the visibility of interference oscillation, it is essential to omit the variation of cross section with electron energy. Therefore, the DDCS for  $N_2$  should be divided by the corresponding DDCS of the two N atoms. In the absence of experimental data for atomic N, the experimental DDCSs for  $N_2$  were divided by theoretical DDCS for 2N, which has been calculated using the effective charges  $Z_T = 1$  and  $Z_T = Z_{bk}$ . Figures 3 and 4 show the DDCS ratios obtained using  $Z_T = 1$  and  $Z_T = Z_{bk}$ , respectively. In Fig. 3, a half sinusoidal oscillatory structure is observed about a horizontal line around a value of 0.5 forward angles and around 0.6 for  $145^\circ$ . The oscillations are expected to be around a horizontal line near 1.0, but as seen from Fig. 1, the calculations using  $Z_T = 1$  overestimate the measured data for all angles, resulting in the oscillations being observed below 1.0. In the case of  $145^\circ$ , the oscillation frequency is seen to be much higher compared to the other angles. The ratios are fitted by the Cohen-Fano-type function (shown by solid lines in Fig. 3) given by

$$\sigma_{\text{norm}}(k, \theta) = A + F \frac{\sin[kc(\theta)d]}{kc(\theta)d}, \quad (8)$$

where  $\sigma_{\text{norm}}(k, \theta)$  represents the DDCS ratio, i.e.,  $(\sigma_{N_2}/\sigma_{2N})$ . The fitted curve matches quite well with the ratios except for  $145^\circ$ , where large discrepancy can be observed beyond 2.5 a.u. Such mismatch may be ascribed to the difference between the measured data and theory for 2N.

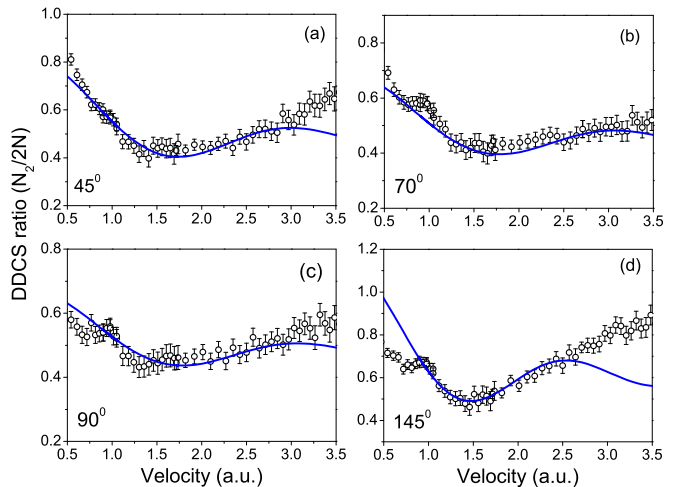


FIG. 3. Experimental-to-theoretical DDCS ratios ( $\sigma_{N_2}/\sigma_{2N}$ ) at different scattering angles for  $Z_T = 1$ . The solid line corresponds to the analytical fitting function given in Eq. (8).

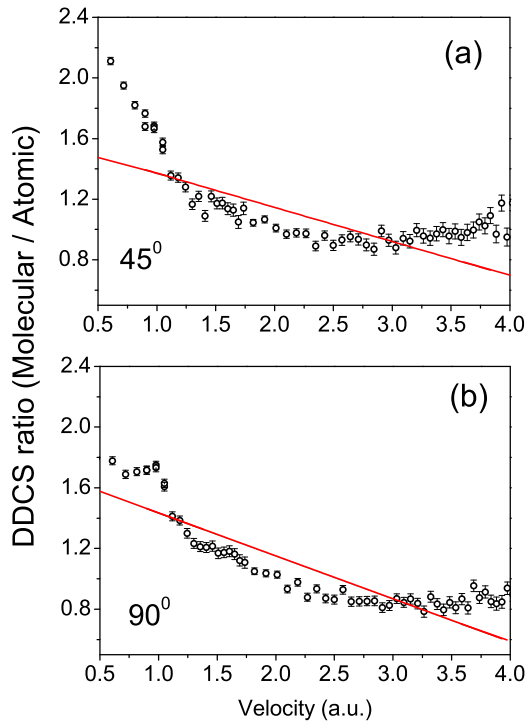


FIG. 4. Ratio of N<sub>2</sub> DDCS to twice atomic nitrogen DDCS obtained using  $Z_T = Z_{bk}$  for atomic N cross section. The solid line corresponds to a linear function of negative slope used for fitting the ratios.

Figure 4 shows similar DDCS ratios which have been obtained using the effective charge  $Z_T = Z_{bk}$  for 2N. The ratios show an oscillatory structure overriding on a straight line of negative slope. To reveal the oscillations clearly, a linear function (shown by the red line) was fitted to the ratios. The cross-section ratios were then divided by the fitted line and the resulting DDCS ratios are shown by the blue circles in Fig. 5 for four different angles. The linear fitting was performed to observe the oscillation about a horizontal line. Half sinusoidal oscillatory structures are observed around a horizontal line

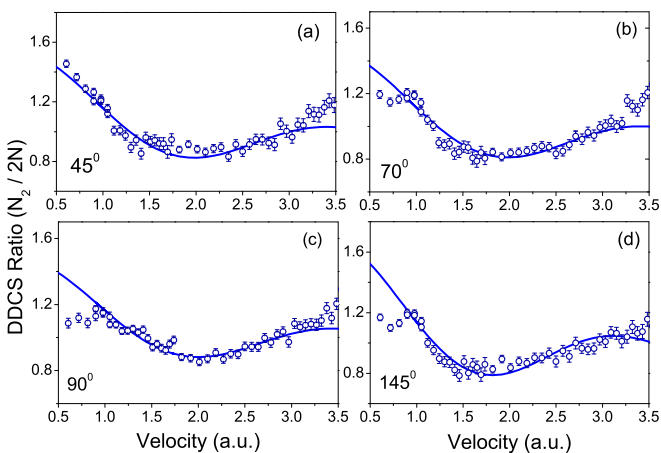


FIG. 5. DDCS ratios ( $\sigma_{N_2}/\sigma_{2N}$ ) obtained after dividing by the linear fitted line in Fig. 4. The solid curve shows the fitting function given in Eq. (8).

near 1.0 for all the angles. This oscillatory behavior, thus, is qualitatively similar to that observed using  $Z_T = 1$ , as shown in Fig. 3. The ratios were further fitted by the Cohen-Fano function given in Eq. (8). It is seen that the fitted function (shown by the blue solid line) has a good agreement with the experimental-to-theoretical ratios.

The choice of effective charge  $Z_T$  for calculating the atomic N cross sections plays a crucial role in determining the shape of the oscillations in the DDCS ratios, as seen in Figs. 3 and 4. Though, from Fig. 1, a better agreement is observed between the measured DDCS of N<sub>2</sub> with that of 2N using  $Z_T = Z_{bk}$  at higher energies, the ratios do not reveal proper oscillation. The oscillation, about a horizontal line, is finally revealed only after dividing by a fitted straight line. On the other hand, for the DDCS for 2N using  $Z_T = 1$ , although it overestimates the N<sub>2</sub> cross section (Fig. 1), it provides clearer oscillation about a horizontal line.

It should be mentioned here that the relative N<sub>2</sub>/N triple-differential cross section (TDCS) of Ref. [14] shows clear structure, although the agreement with the Cohen-Fano factor is a bit poor at such lower-impact energy (250 eV), compared to the high-energy electron beam used in this experiment. Also we should note that in Ref. [14], the experiments and calculations are done only for the  $3\sigma_g$  orbital, whereas our experimental results are presented for all molecular orbitals. We know from the case of ion impact that the interference effect can be shadowed [16,17,26] when the sum of all orbital contributions is included. The remarkable result obtained in our work is that the signature of interference patterns appears for the DDCS ratio considering the contributions of all molecular orbitals. This is possibly due to the fact that simultaneous multiple ionization of different orbitals is much less in the case of fast electron-impact ionization, compared to that for heavy-ion collisions in Refs. [16,17].

## 2. Frequency parameter

The variation of the angle-dependent frequency parameter  $c(\theta)$  [obtained from the fitting function in Eq. (8)] as a function of electron emission angles is displayed in Fig. 6. It is seen that for all of the forward angles, frequency remains

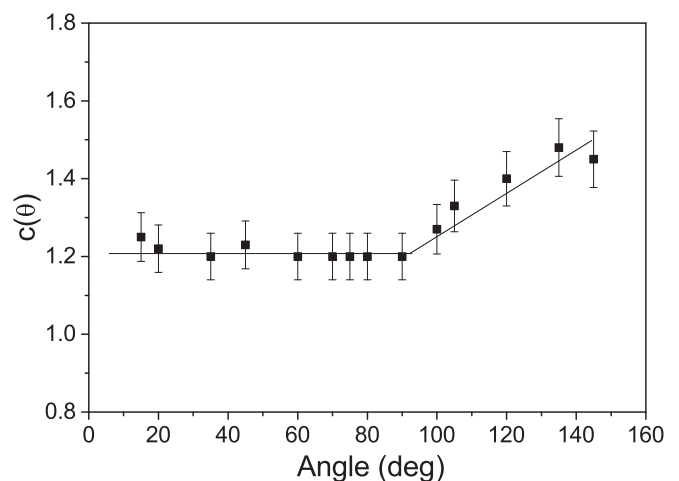


FIG. 6. Frequency parameter  $c(\theta)$  plotted as a function of electron emission angle. The solid line is to guide the eyes.

almost constant up to  $90^\circ$ . In the case of backward angles, the frequency parameter increases steadily with the increase in the observation angle. The frequency parameter changes from a value of 1.2 to 1.45 over the entire angular range, giving an enhancement of a factor of about 1.20(8). The shape of the angular dependence of  $c(\theta)$  is quite different than that for  $H_2$  [8].  $N_2$  is a multielectronic target, and therefore ionization is possible from different molecular orbitals and hence some difference can be expected in the observed oscillation parameters compared to that for the simplest molecule, i.e.,  $H_2$ .

### 3. Forward-backward angular asymmetry

In the previous section, we have obtained the interference oscillation from the ratio of the experimental DDCS for  $N_2$  to that of theoretical DDCS for atomic nitrogen. From Figs. 3 and 4, it is inferred that the pattern of interference oscillation depends on the choice of effective charge  $Z_T$  used for atomic N calculations. Another possible way to deduce the oscillation is from the asymmetry parameter according to the prescription given in [38]. In this method, the oscillation is directly determined from the ratios of the measured DDCS and hence does not depend on the absolute normalization procedure. In addition, since it involves the DDCS for the molecular target only, it is also free from atomic cross section and the choice of any effective charge. According to [39], non-Coulombic potential for a multielectronic atom or molecule contributes to the forward-backward asymmetry. In the case of a diatomic molecule, the Young-type interference can also influence the asymmetry parameter, as shown in Refs [7,38,40]. The asymmetry parameter  $\alpha(k)$  is defined as

$$\alpha(k) = \frac{\sigma(k, \theta) - \sigma(k, \pi - \theta)}{\sigma(k, \theta) + \sigma(k, \pi - \theta)}, \quad (9)$$

where  $k$  is momentum and  $\theta$  is chosen to be a small forward angle,  $35^\circ$ . As shown by Fainstein *et al.* [39], expanding  $\sigma(k, \theta)$  in terms of the Legendre polynomials and considering the first few terms of the series expansion,  $\alpha(k)$  represents the asymmetry parameter for  $\theta = 0$ . Since the variation of angular distribution around 0 and  $\pi$  is very small, we have used  $\theta = 35^\circ$  in the present case to calculate  $\alpha(k)$  approximately. The asymmetry parameter, obtained from the molecular DDCS for two complementary angles, is shown in Fig. 7 as a function of electron velocity. The quantity  $\alpha(k)$  shows a full sinusoidal oscillation with a minor increasing trend in the ejected electron velocity range of 0.6 to 3.5 a.u. From Fig. 6, we have seen that the frequency of oscillations is greater for backward angles compared to forward angles. This difference in frequency for two complementary angles give rise to the oscillatory structure in  $\alpha(k)$ . By replacing the DDCS in Eq. (9) with that in Eq. (7), which contains the Cohen-Fano term, one gets an expression for the asymmetry parameter  $\alpha(k)$  as follows [40]:

$$\alpha(k) = \frac{k\beta c(\theta)d(A-B) + \{A\beta \sin[kc(\theta)d] - B \sin[k\beta c(\theta)d]\}}{k\beta c(\theta)d(A+B) + \{A\beta \sin[kc(\theta)d] + B \sin[k\beta c(\theta)d]\}}, \quad (10)$$

where electron energy  $\epsilon_k = k^2/2$ ,  $A$  and  $B$  are the amplitudes of oscillation for the two complementary angles,  $d$  is the internuclear distance,  $c(\theta)$  is the frequency of low forward

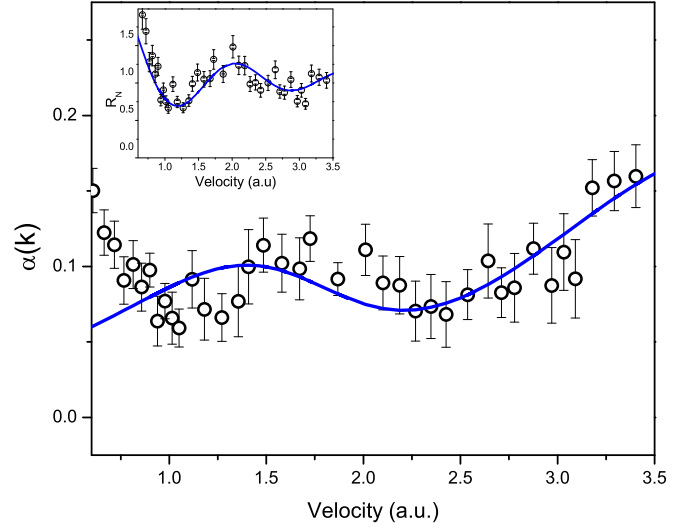


FIG. 7. Forward-backward asymmetry parameter obtained from measured DDCS of  $N_2$  for low forward angle ( $35^\circ$ ) and large backward angle ( $145^\circ$ ). The solid line corresponds to the model fitting given by Eq. (10). Inset: asymmetry parameter divided by first-order fitting function.

angle having  $\theta$  ( $= 35^\circ$  in this case), and  $\beta$  is the ratio of oscillation frequency for backward to forward angles, i.e.,  $c(\pi - \theta)/c(\theta)$ . The model fitting matches well with the experimental data above 1.4 a.u., as represented by the solid line in Fig. 7. A closer look at Fig. 7 shows that though the fitting matches well with the data, a periodic deviation is also observed. In order to study the deviations, we have divided the data points by the first-order fitting function (see the inset). The resulting data reveal an oscillatory structure which is further fitted by a model (solid line), similar to the Cohen-Fano-type formalism,

$$R_N = D + E \frac{\sin(nkd)}{nkd}, \quad (11)$$

where  $n$  is the frequency of oscillation, which is found to be 1.8, i.e., almost twice the frequency of the primary oscillation. This clearly indicates the presence of a higher-order contribution arising from a second-order scattering mechanism [24,25,41].

## V. CONCLUSION

We have measured the absolute DDCS of the secondary electron emission in ionization of the  $N_2$  molecule under the impact of fast electrons (7 keV) for emission angles between  $15^\circ$  and  $145^\circ$ . Experimental data have been compared with the theoretical calculations based on the B1 model, under the CNDO approximation with two different values of effective charges. The experimental-to-theoretical DDCS ratios (i.e.,  $N_2/2N$ ) were calculated using two different values of  $Z_T$ . The ratios show an oscillatory structure due to the Young-type interference, whose shape was found to be dependent on the choice of  $Z_T$ . Though in the case of  $Z_T = 1$  the DDCS ratios revealed clear oscillations, for  $Z_T = Z_{bk}$  the ratios had to be normalized by a linear function to deduce the oscillations clearly. The ratios have been fitted with the Cohen-Fano

model for either case. The derived values of the frequency parameter are seen to be constant for all forward angles and increase for backward angles. The forward-backward angular asymmetry displayed the oscillation very clearly and the fitting function based on the Cohen-Fano model matches well with the experimental ratio. However, periodic deviation from the first-order function indicates the presence of a second-order interference effect. It should be emphasized that since the asymmetry parameter is free from experimental normalization

procedure and does not require any theoretical atomic N cross section, it therefore provides a more convincing proof of the oscillation.

#### ACKNOWLEDGMENTS

The authors would like to thank D. Misra for the helpful discussions and also acknowledge the help of W. A. Fernandes and Nilesh Mhatre during the experiment.

- 
- [1] C. B. Opal, W. K. Peterson, and E. C. Beaty, *J. Chem. Phys.* **55**, 4100 (1971).
- [2] T. D. Mark, *J. Chem. Phys.* **63**, 3731 (1975).
- [3] H. D. Cohen and U. Fano, *Phys. Rev.* **150**, 30 (1966).
- [4] N. Stolterfoht, B. Sulik, V. Hoffmann, B. Skogvall, J. Y. Chesnel, J. Rangama, F. Fremont, D. Hennecart, A. Cassimi, X. Husson, A. L. Landers, J. A. Tanis, M. E. Galassi, and R. D. Rivarola, *Phys. Rev. Lett.* **87**, 023201 (2001).
- [5] N. Stolterfoht, B. Sulik, L. Gulyás, B. Skogvall, J. Y. Chesnel, F. Frémont, D. Hennecart, A. Cassimi, L. Adoui, S. Hossain, and J. A. Tanis, *Phys. Rev. A* **67**, 030702(R) (2003).
- [6] D. Misra, U. Kadhane, Y. P. Singh, L. C. Tribedi, P. D. Fainstein, and P. Richard, *Phys. Rev. Lett.* **92**, 153201 (2004).
- [7] S. Chatterjee, D. Misra, A. H. Kelkar, Lokesh C. Tribedi, C. R. Stia, O. A. Fojón, and R. D. Rivarola, *J. Phys. B: At. Mol. Opt. Phys.* **42**, 065201 (2009).
- [8] S. Chatterjee, D. Misra, P. D. Fainstein, and L. C. Tribedi, *Phys. Scr.* **T144**, 014040 (2011).
- [9] D. Akoury, K. Kreidi, T. Jahnke, Th. Weber, A. Staudte, M. Schoffler, N. Neumann, J. Titze, L. Ph. H. Schmidt, A. Czasch, O. Jagutzki, R. A. Costa Fraga, R. E. Grisenti, R. Díez Muino, N. A. Cherepkov, S. K. Semenov, P. Ranitovic, C. L. Cocke, T. Osipov, H. Adaniya, J. C. Thompson, M. H. Prior, A. Belkacem, A. L. Landers, H. Schmidt-Bocking, and R. Dorner, *Science* **318**, 949 (2007).
- [10] D. S. Milne-Brownlie, M. Foster, Junfang Gao, B. Lohmann, and D. H. Madison, *Phys. Rev. Lett.* **96**, 233201 (2006).
- [11] S. E. Canton, E. Plésiat, J. D. Bozek, B. S. Rude, P. Decleva, and F. Martin, *Proc. Natl. Acad. Sci. USA* **108**, 7302 (2011).
- [12] J. L. Baran, S. Das, F. Járai-Szábo, K. Póra, L. Nagy, and J. A. Tanis, *Phys. Rev. A* **78**, 012710 (2008).
- [13] M. Winkworth, P. D. Fainstein, M. E. Galassi, J. L. Baran, B. S. Dassanayake, S. Das, A. Kayani, and J. A. Tanis, *Nucl. Instrum. Methods Phys. Res., Sect. B* **267**, 373 (2009).
- [14] H. Chaluvadi, N. O. Zehra, M. Dogan, C. Ning, J. Colgan, and D. Madison, *J. Phys. B* **48**, 155203 (2015).
- [15] L. R. Hargreaves, C. Colyer, M. A. Stevenson, B. Lohmann, O. Al-Hagan, D. H. Madison, and C. G. Ning, *Phys. Rev. A* **80**, 062704 (2009).
- [16] S. Nandi, S. Biswas, C. A. Tachino, R. D. Rivarola, and L. C. Tribedi, *Eur. Phys. J. D* **69**, 192 (2015).
- [17] S. Nandi, A. N. Agnihotri, S. Kasthurirangan, A. Kumar, C. A. Tachino, R. D. Rivarola, F. Martín, and L. C. Tribedi, *Phys. Rev. A* **85**, 062705 (2012).
- [18] M. Ilchen, L. Glaser, F. Scholz, P. Walter, S. Deinert, A. Rothkirch, J. Seltmann, J. Viehhaus, P. Decleva, B. Langer, A. Knie, A. Ehresmann, O. M. Al-Dossary, M. Braune, G. Hartmann, L. C. Tribedi, A. Meissner, M. AlKhaldi, and U. Becker, *Phys. Rev. Lett.* **112**, 023001 (2014).
- [19] D. Rolles *et al.*, *Nature (London)* **437**, 711 (2005).
- [20] B. Zimmermann *et al.*, *Nat. Phys.* **4**, 649 (2008).
- [21] S. K. Semenov *et al.*, *J. Phys. B: At. Mol. Opt. Phys.* **39**, L261 (2006).
- [22] X. J. Liu *et al.*, *J. Phys. B: At. Mol. Opt. Phys.* **39**, 4801 (2006).
- [23] K. Ueda *et al.*, *Chem. Phys.* **329**, 329 (2006).
- [24] N. Stolterfoht, B. Sulik, B. Skogvall, J. Y. Chesnel, F. Frémont, D. Hennecart, A. Cassimi, L. Adoui, S. Hossain, and J. A. Tanis, *Phys. Rev. A* **69**, 012701 (2004).
- [25] D. Misra, A. H. Kelkar, S. Chatterjee, and L. C. Tribedi, *Phys. Rev. A* **80**, 062701 (2009).
- [26] C. A. Tachino, F. Martin, and R. D. Rivarola, *J. Phys. B* **45**, 025201 (2012).
- [27] A. Kumar, D. Misra, K. V. Thulasiram, L. C. Tribedi, and A. K. Pradhan, *Nucl. Instrum. Methods B* **248**, 247 (2006).
- [28] Deepankar Misra, K. V. Thulasiram, W. Fernandes, Aditya H. Kelkar, U. Kadhane, Ajay Kumar, Yeshpal Singh, L. Gulyas, and Lokesh C. Tribedi, *Nucl. Instrum. Methods Phys. Res., Sect. B* **267**, 157 (2009).
- [29] B. Senger, E. Wittendorp-Rechenmann, and R. V. Rechenmann, *Nucl. Instrum. Methods Phys. Res.* **194**, 437 (1982).
- [30] J. A. Pople, D. P. Santry, and G. A. Segal, *J. Chem. Phys.* **43**, S129 (1965).
- [31] C. W. Scherr, *J. Chem. Phys.* **23**, 569 (1955).
- [32] K. Siegbahn, C. Nordling, G. Johansson, J. Hedman, P. F. Hedén, K. Hamrin, U. Gelius, T. Bergmark, L. O. Werme, R. Manne, and Y. Baer, *ESCA Applied to Free Molecules* (North Holland, Amsterdam, 1969).
- [33] P. D. Fainstein, V. H. Ponce, and R. D. Rivarola, *J. Phys. B: At. Mol. Opt. Phys.* **21**, 287 (1988).
- [34] E. Clementi and C. Roetti, *At. Data Nucl. Data Tables* **14**, 177 (1974).
- [35] D. Belkić, R. Gayet, and A. Salin, *Phys. Rep.* **56**, 279 (1979).
- [36] M. F. Ciappina, O. A. Fojon, and R. D. Rivarola, *J. Phys. B* **47**, 042001 (2014).
- [37] L. Nagy, L. Kocbach, K. Pora, and J. Hansen, *J. Phys. B* **35**, L453 (2002).

- [38] D. Misra, A. Kelkar, U. Kadhane, A. Kumar, L. C. Tribedi, and P. D. Fainstein, *Phys. Rev. A* **74**, 060701(R) (2006).
- [39] P. D. Fainstein, L. Gulyás, F. Martin, and A. Salin, *Phys. Rev. A* **53**, 3243 (1996).
- [40] D. Misra, A. Kelkar, U. Kadhane, A. Kumar, Y. P. Singh, L. C. Tribedi, and P. D. Fainstein, *Phys. Rev. A* **75**, 052712 (2007).
- [41] A. Messiah, *Quantum Mechanics* (North-Holland, Amsterdam, 1970), Vol. II, pp. 848–852.